



Bitlis Eren University Journal of Science and Technology

Bitlis Eren Üniversitesi Bilim ve Teknoloji
Dergisi

Yıl/Year: 2021 • Cilt/Volume: 11 • Sayı/Issue: 2

ISSN: 2146-7706

Contact:

BEU Journal of Science and Technology, Bitlis Eren Üniversitesi 13000, Merkez, Bitlis/ TÜRKİYE
Tel: 0 (434) 222 0045

beujstd@beu.edu.tr <http://dergipark.gov.tr/beuscitech>



Bitlis Eren University Journal of Science and Technology

e-ISSN	:	2146-7706
Date of Issue	:	December 20 2021
Issue Period	:	December 2021
Volume	:	11
Issue	:	2
Founded	:	2011
Location	:	Bitlis
Language	:	English
Address	:	Bitlis Eren University Journal of Science and Technology Bitlis Eren Üniversitesi 13000, Merkez, Bitlis/ TÜRKİYE
e-mail	:	beujstd@beu.edu.tr
URL	:	http://dergipark.gov.tr/beuscitech

Bitlis Eren University Journal of Science and Technology

Yıl/Year: 2021 • Cilt/Volume: 11 • Sayı/Issue: 2

Editorial Board

On behalf of Bitlis Eren University Owner	Prof. Dr. Necmettin ELMASTAŞ <i>Bitlis Eren University</i>
Editor-in-Chief	Assoc. Prof. Dr. Kubilay TOYRAN <i>Bitlis Eren University</i>
Editorial Board	Prof. Dr. Mehmet Cihan AYDIN <i>Bitlis Eren University</i>
	Prof. Dr. Zeynep AYGÜN <i>Bitlis Eren University</i>
	Assoc. Prof. Dr. Murat KARAKAŞ <i>Bitlis Eren University</i>
	Assoc. Prof. Dr. Engin YILMAZ <i>Bitlis Eren University</i>
	Assoc. Prof. Dr. Musa ÇIBUK <i>Bitlis Eren University</i>
	Assist. Prof. Dr. Fahrettin ÖZBEY <i>Bitlis Eren University</i>
	Assist. Prof. Dr. Behçet KOCAMAN <i>Bitlis Eren University</i>
	Assist. Prof. Dr. Faruk ORAL <i>Bitlis Eren University</i>
	Assist. Prof. Dr. Tülay ÇEVİK SALDIRAN <i>Bitlis Eren University</i>
	Assist. Prof. Dr. Ramazan ERDOĞAN <i>Bitlis Eren University</i>

Bitlis Eren University Journal of Science and Technology

Yıl/Year: 2021 • Cilt/Volume: 11 • Sayı/Issue: 2

Bitlis Eren University Journal of Science and Technology (Bitlis Eren Univ J Sci & Technol) is an international, refereed open access electronic journal. Research results, reviews and short communications in the fields of Biology (Medicinal, Molecular and Genetics, Veterinary and Agriculture), Physics, Chemistry, Mathematics and Statistics, and also Engineering Sciences are accepted for review and publication. Papers will be published in English. Scientific quality and scientific significance are the primary criteria for publication. Articles with a suitable balance of practice and theory are preferred. Manuscripts previously published in other journals and as book sections will not be accepted.




























Bitlis Eren University Journal of Science and Technology indexed in:

- EBSCO

Bitlis Eren University Journal of Science and Technology

Yıl/Year: 2021 • Cilt/Volume: 11 • Sayı/Issue: 2

Articles

İrfan EMRE  , Turker TUNCER  , Sengul DOGAN  , Murat KÜRŞAT  , Osman GEDİK  , Yaşar KIRAN 	22-28
An Accurate HOG based Exemplar Pyramid Method for Image Classification of <i>Astragalus L.</i> Taxa	
Ercan IŞIK  , Eyyüp DEMIRKIRAN 	29-35
The effect of different earthquake ground motion level on performance of reinforced-concrete structures	
Biröl BAŞER  , Nazli AKAY  , Murat KÜRŞAT 	36-45
Using of light and scanning electron microscopy for pollen morphology of some <i>Epilobium</i> (Onagraceae) taxa and Its taxonomic importance	
İbrahim DEMİR  , Murat ÜNAL 	46-50
Habitat Classification of Cilo Glaciers and Their Surroundings	
Ali Emre ULU  , M. Cihan AYDIN  , Fevzi ÖNEN 	51-59
Experimental and numerical analysis of weir structures in open channel flows	
Ayşe METİN KARAKAŞ  , Aslıhan DEMİR  , Sinan ÇALIK 	60-75
Dynamic Conditional Dependence for Turkey Earthquake Data: CD Vine Copula Approach	
Murat KARAKAŞ 	76-81
Some inclusion results for the new Tribonacci-Lucas matrix	
Ezman KARABULUT 	82-86
The Possible External Factor Effecting On NO₂ Molecule During Lightning Flash Under Corona Discharge	
Fatih Ahmet CELİK 	87-90
Study on crystallization process of SiO₂ based SiO₂-Li₂O nano-wire glass ceramic: A molecular dynamics simulation based on SCC-DFTB calculations	
Hakan ÇOBAN  , Özcan Ali KALKAN 	91-96
Trace element geochemistry of Bitlis ignimbrites generated by Quaternary Nemrut Volcano: inferences for A2-type magma generation in Eastern Anatolia post-collisional extensional setting	
Ercan IŞIK  , Ali Emre ULU  , M. Cihan AYDIN 	97-103
A case study on the updates of Turkish rapid visual screening methods for reinforced-concrete buildings	

Available online at www.dergipark.gov.tr/beuscitech

Journal of Science and Technology

E-ISSN 2146-7706



An Accurate HOG based Exemplar Pyramid Method for Image Classification of *Astragalus* L. Taxa

İrfan EMRE^{a*}, Turker TUNCER^b, Sengul DOGAN^b, Murat KÜRŞAT^c, Osman GEDİK^d, Yaşar KIRAN^e

^a Firat University, Faculty of Education, Department of Basic Education, TR-23119, Elazig, Turkey

^b Firat University, Faculty of Technology, Department of Digital Forensics Engineering, TR-23119, Elazig, Turkey

^c Bitlis Eren University, Faculty of Science and Arts, Department of Biology, TR-13000, Bitlis, Turkey

^d Kahramanmaraş Sutçu Imam University, Faculty of Agriculture, Department of Field Crops, TR-46000, Kahramanmaraş, Turkey

^e Faculty of Science and Arts, Department of Biology, Firat University TR-23119, Elazig, Turkey

ARTICLE INFO

Article history:

Received 05 June 2021

Received in revised form 01 December 2021

Accepted 01 December 2021

Keywords:

Chromosome

Image processing

Astragalus

HOG

Plant classification

ABSTRACT

As known from the literature, machine learning (ML) is one of the popular researches have been used variable areas. In this work, a novel exemplar pyramid method is presented to accurately classify *Astragalus* L. taxa by using their chromosome images. To implement ML to biological images, the proposed exemplar pyramid method is used. Histogram of Oriented Gradients (HOG) is utilized as feature generator. The proposed exemplar pyramid method consists of preprocessing, feature generation and concatenation, feature selection and classification phase. 10 classifiers are chosen to train and test the extracted features. According to results, the proposed exemplar pyramid generates discriminative features. because five of the used 10 classifiers achieved 100.0% classification rate.

© 2021. Turkish Journal Park Academic. All rights reserved.

1. Introduction

The classification of plants not only contribute to the botany but also supports the ecology, conservation, genetics and phytochemical studies (Wang et al., 2017). Traditional plant taxonomy studies use morphological, phytochemical, molecular and anatomical characters but these studies require experts in botany and sometimes these features aren't not enough to solve the systematical problems (Liu and Kan, 2016).

The studies showed that new approaches such as machine learnings are used in many areas such as financial analysis, transportation, health care, clinical diagnosis, image identification and also plant identification studies (Singh and Singh, 2021). The combined use of image processing and machine learning have greatly supplied to the solutions to describe of plant species using images from leaves, fruits or flowers (Guillermo et al., 2016; Naresh and Nagendraswamy, 2016; Yiğit et al., 2019). Machines perceive the objects and evaluate the results with little or human input in the machine

* Corresponding author. Tel.: +0 424 237 0000; fax: +0 424 236 50 64

E-mail address: iemre@firat.edu.tr

ORCID : 0000-0003-0591-3397 (İ. Emre), 0000-0002-5126-6445 (T. Tuncer), 0000-0001-9677-5684 (S. Dogan), 0000-0002-0861-4213 (M. Kürşat), 0000-0002-4816-3154 (O. Gedik), 0000-0002-3225-2080 (Y. Kiran)

learning is an artificial intelligence approach (Singh and Singh, 2021). The image pattern identification was used to classify an image or a desired object or region into one of categories (Uchida, 2013). Image processing includes a series of transforms to increase the quality of the image and the image characteristics (Siraj et al., 2010). Histogram of Oriented Gradient (HOG) is one of the reliable feature extraction methods for image or pattern detection (Fernandes et al., 2016). It splits the input images into small square cells and later counts the histogram of gradient directions based on the basic differences (Ebrahimzadeh and Jampour, 2014).

The goal of this study is to compare of nine *Astragalus* L. (*Astragalus camptoceras* Bunge, *Astragalus cretaceus* Boiss., *Astragalus campylorhynchus* Fisch. & C.A.Mey.A., *Astragalus suberosus* Banks & Sol., *Astragalus leporinus* Boiss. var. *hirsutus* (Post) D.F.Chamb, *Astragalus densifolius* Lam. subsp. *densifolius*, *Astragalus lamarckii* Boiss., *Astragalus anthylloides* Lam., *Astragalus odoratus* Lam.) taxa by using chromosome figures based on HOG feature extraction method. *Astragalus* L. is the biggest genus in the Fabaceae, has over the 3000 species around the world and it is represented by 478 taxa, of which 224 are endemic in Turkey (Çeçen et al., 2016; Albayrak and Kaya, 2019). The basic chromosome number of *Astragalus* L. species varied from $x:7,8,11-15$ (Sheidai et al., 2009). Also, Gedik et al. (2019) found that somatic chromosome numbers of nine *Astragalus* taxa in this study are $2n:2x:16, 32$ and $2n:4x:32$ chromosomes. They indicated that *Astragalus* taxa have metacentric and sub-metacentric chromosomes and one of them (*A. densifolius* Lam. subsp. *densifolius*) has sat-chromosome (Gedik et al., 2019). Although the chromosome morphology studies were largely used in classification studies, calculations and the determination of other characters in these studies are done manually using traditional methods that are open to error. Therefore this study aims to prevent such errors by using machine learning.

2. Dataset

Plant materials were collected from natural habitats and samples were stored in Bitlis Eren University Herbarium (BEUH). Karyological analysis of nine *Astragalus* L. taxa was conducted based on the method proposed by Elci (1982). Microphotographs of 387 cells in the metaphase stage of mitosis belong to each species were taken using Olympus BX51 light microscope after staining process completed. The chromosome images of nine *Astragalus* species were utilized as input for the proposed method. Attributes of the used dataset were given as follows. The used dataset consists of nine classes. There are 19-57 images in the 1st-9th class (1st class is *Astragalus camptoceras* Bunge; 2nd class is *Astragalus cretaceus* Boiss., 3rd class is *Astragalus campylorhynchus* Fisch. & C.A.Mey.A., 4th class is *Astragalus suberosus* Banks & Sol., 5th class is *Astragalus leporinus* Boiss. var. *hirsutus* (Post) D.F.Chamb, 6th class is *Astragalus densifolius* Lam. subsp. *densifolius*, 7th class is *Astragalus lamarckii* Boiss., 8th class is *Astragalus anthylloides* Lam., 9th class is *Astragalus odoratus* Lam.). These images were RGB and were JPG. Size of these images were 3072 x 2304.

3. A Histogram of Oriented Gradients based Exemplar Pyramid Method

The main purpose of this study is to automatically classify *Astragalus* species by proposing a new ML method. To achieve this goal, a new hand-crafted feature generation and concatenation method is presented. The presented method is named as HOG based exemplar pyramid method. The proposed HOG based exemplar pyramid method is inspired by deep learning methods. Deep learning methods can extract low level, medium level and high level features but they have long execution times because need millions parameters set. Therefore, we presented a hand-crafted feature extraction method to obtain low level, medium level and high level features. Schematical demonstration of the proposed HOG based exemplar pyramid method was shown in Fig. 1.

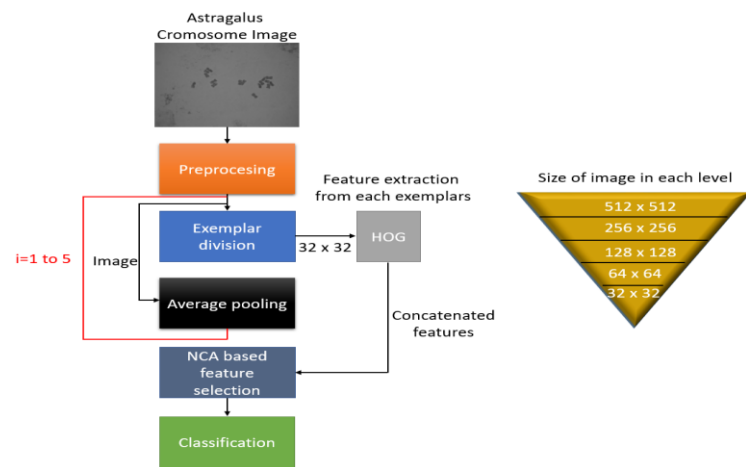


Figure 1. Schematical explanation of the proposed HOG based exemplar pyramid image classification method

Pseudo code of the proposed exemplar pyramid method was also shown in Algorithm 1 for better understanding. Algorithm 1 summarized the proposed HOG based exemplar pyramid image classification method.

Algorithm 1. Pseudo code of the proposed HOG based exemplar pyramid method.

<p>Input: Microscopic <i>Astragalus</i> image (Im) with size of 3072 x 2304 x 3. Output: Predicted values (PV) with length of 387.</p> <pre> 0: Load microscopic <i>Astragalus</i> image. 1: Apply RGB2Gray conversion to Im. 2: Resize gray level Im to 512 x 512. 3: for $i=1$ to 5 do // Create levels 4: $counter = 1$; 5: $[m, n] = size(Im)$; 6: for $k=1$ to m step by 32 do // Divide 32 x 32 sized exemplars into Im. 7: for $l=1$ to n step by 32 do 8: $Exm = Im(k:k+31:l:l+31)$; 9: $feature((counter - 1) * 324 + 1:counter * 324) = HOG(Exm)$; 10: $counter = counter + 1$; 11: end for l 12: end for k 13: $Im = averagePool(Im)$; // Apply average pooling to Im. 14: end for i 15: Select 128 most discriminative features. 16: Classify selected 128 features.</pre>

Phases of the proposed HOG based exemplar pyramid image classification method were explained in sub-sections for better understanding.

3.1. Preprocessing

Size of the used *Astragalus* Chromosome images is 3072 x 2304 x 3 and these microscopic images were color (RGB images). In the used preprocessing phase, RGB2Gray conversion and image resizing were used and steps of this phase are given as below.

Step 1: Apply RGB2Gray transformation to Raw *Astragalus* image. Mathematical notation of the RGB2Gray transformation was given in Eq. 1.

$$gray = Im(:, :, 1) * 0.299 + Im(:, :, 1) * 0.587 + Im(:, :, 1) * 0.114 \quad (1)$$

where *gray* was grayscale image with size of 3072 x 2304.

Step 2: Resize grayscale image to 512 x 512 sized image.

$$gray = imresize(gray, 512 \times 512) \quad (2)$$

where *imresize* defines resizing function.

3.2. Exemplar division

The proposed *Astragalus* chromosome image classification method was an exemplar classification method. To extract features in detail, exemplar feature extraction with levels were used. Therefore, the second phase of the proposed *Astragalus* chromosome image classification method were exemplar division. The generated 512 x 512 sized gray level image was divided into exemplars with size of 32 x 32.

Step 3: Divide 32 x 32 sized exemplars to image.

$$Exm^k = gray(i : i + 31, j : j + 31) \quad (3)$$

$$i = \{1, 33, \dots, row\} \quad (4)$$

$$j = \{1, 33, \dots, col\} \quad (5)$$

$$k = \{1, 2, \dots, \frac{row * col}{32^2}\} \quad (6)$$

Where Exm^k k^{th} exemplar, *i* and *j* describe indices of the image, *row* and *col* are number of rows and columns of the preprocessed Graylevel image.

3.3. Feature Extraction with Histogram of Oriented Gradients

HOG is one of the mostly known image descriptors and has been widely used for computer vision studies. The use of the HOG algorithm, which can also be called characteristic of the orientation (θ) and magnitude values of the pixels in the image in recent years, has received a lot of attention in many areas. It is an effective local image descriptor and calculates oriented gradients. The mathematical representation of the HOG method is as Eqs. 7-10.

$$G_x = M_x \odot Exm \quad (7)$$

$$G_y = M_y \odot Exm \quad (8)$$

$$G = \sqrt{G_x^2 + G_y^2} \quad (9)$$

$$\alpha = \arctan\left(\frac{G_x}{G_y}\right) \quad (10)$$

where M_x, M_y represent convolution matrixes. To calculate gradients of and exemplar, convolution process is used and \odot represents convolution operator. G_x and G_y gradients of the used exemplar by using M_x and M_y . G is oriented gradients and α angel of the gradients. By using histograms G and α , HOG features are obtained.

In this study, we used HOG for automated classification of the microscopic images of the *Astragalus* chromosomes.

Step 4: Generate features using HOG and each exemplars.

$$feat^k = HOG(Exm^k) \quad (11)$$

where $feat^k$ is k^{th} feature of k^{th} exemplar with size of 324.

Step 5: Concatenate features of each exemplar to obtain level features.

$$feat^{level} = feat^1 | feat^2 \dots | feat^k \quad (12)$$

where $feat^{level}$ features of level, $|$ is concatenation operator. We created five levelled pyramid by using average pooling.

3.4. Average Pooling

Average pooling has been widely used in the deep networks to create layers and reduce dimensionality of the features or images. It is basic and effective method. To create pyramid, average pooling is used.

Step 6: Reduce dimension of the image using average pooling with 2 x 2 sized non-overlapping blocks.

$$gray_{r,c}^{level+1} = \frac{gray_{i,j}^{level} + gray_{i,j+1}^{level} + gray_{i+1,j}^{level} + gray_{i+1,j+1}^{level}}{4} \quad (13)$$

where *r* and *c* indices of the pooled image.

Then, pooled image is divided into exemplars and features extraction process (HOG) is implemented. Steps 3-6 are repeated five times and each level features are concatenated to obtain final feature with size of 110,484.

3.5. Feature selection with NCA

The obtained final feature vector was very large. Therefore, a feature selector should be used. NCA was selected as feature selector in this work. NCA computes weights of each features and these weights represents strength of the used features. It was used for classification and regression because uses gradient optimization methods (stochastic gradients descent, adam) to calculate weights. Distances from features were calculated by Manhattan distance. In this view, NCA similar to 1NN. Steps of the NCA based feature selection phase were given as below.

Step 7: Normalize final features in range of from 0 to 1. To calculate correct weights, normalization should be used

because NCA is a distance based feature selector.

$$feature = \frac{feature - feature_{min}}{feature_{max} - feature_{min}} \quad (14)$$

Step 8: Generate weights using NCA.

$$weights = NCA(feature) \quad (15)$$

Step 9: Sort weights from large to small and calculate indexes of the ordered weights.

$$[sorted, indexes] = sort(weights) \quad (16)$$

Step 10: Select 128 most discriminative feature using indexes.

$$feat_i^S = feature_{indexes_i}, i = \{1, 2, \dots, 128\} \quad (17)$$

where $feat^S$ defines selected 128 most discriminative features according to NCA.

3.6. Classification

Classification was final phase of the proposed HOG based exemplar pyramid method. 128 most discriminative features were forwarded to conventional classifiers. To use classifiers, MATLAB Classification Learner (MCL) Toolbox was chosen. There were 23 classifiers in the MCL and these classifiers can be grouped as Trees, Discriminants, Support Vector Machines, KNNs and Ensemble Classifiers. We selected Fine Tree (FT), Linear Discriminant (LD), Quadratic SVM (QSVM), Cubic SVM (CSVM), Medium Gaussian SVM (MGSVM), Fine KNN (FKNN), Weighted KNN (WKNN), Ensemble Subspace Discriminant (ESD), Ensemble Subspace KNN (ESKNN) and Ensemble Bagged Tree (EBT). 10 of the 23 classifiers of the MCL were used in the classification phase to obtain comprehensively results and default settings of these classifiers were used. Tests were validated using 10-fold cross-validation.

4. Results and Discussions

Various studies have shown that deep learning techniques achieve good results in plant classification. (Grinblat et al., 2016; Sun et al., 2017). For example, Grinblat et al. (2016) demonstrated the successful results of deep learning in the plant identification by using leaf vein images. Also, Sun et al. (2017) used deep learning models to design plant classification in the natural habitats and they found that the achievement ratio of model was determined 91.78% (Sun et al., 2017). Similarly, Kayhan and Ergün (2020) classified the medicinal and aromatic plants by using several machine learning techniques and their results showed that plants were diagnosed in the correct classifications.

In this study, numerical results of the used 10 classifiers were presented. These 10 classifiers were used for validation to illustrate success of the proposed HOG based exemplar pyramid feature extraction method. The mostly used performance parameter for the classification was accuracy

(ACC). ACC has very simple mathematical. It is calculated by dividing the number of correctly predicted observations by the number of observation. Formula of ACC was given as Eq. 18.

$$ACC = \frac{NTPO}{NO} \quad (18)$$

ACC: Classification accuracy

NTPO: Number of true predicted observations.

NO: Number of observation.

We used 10 classifiers in five groups and these groups are tree, discriminant, SVM, KNN and ensemble. Tests were performed by using 10-fold CV. It means of the proposed method was a robust method. Calculated ACC are listed in Table 1.

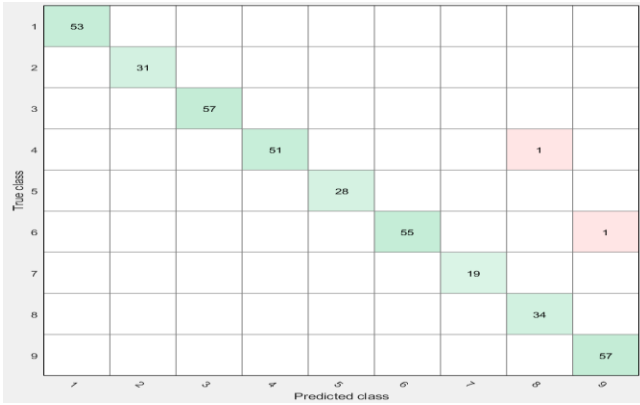
Table 1. Calculated ACC rates using tree, discriminant, SVM, KNN and ensemble classifiers.

Group	Name	ACC	Training Time (sec)
Tree	Fine Tree	74.16%	1.43
	Linear Discriminant	99.48%	0.64
KNN	Fine KNN	100.0%	4.88
	Weighted KNN	99.48%	5.61
SVM	Quadratic SVM	100.0%	4.55
	Cubic SVM	100.0%	4.43
	Medium Gaussian SVM	100.0%	7.43
Ensemble	Ensemble Subspace Discriminant	98.70%	9.88
	Ensemble Subspace KNN	100.0%	9.79
	Ensemble Bagged Tree	97.42%	11.05

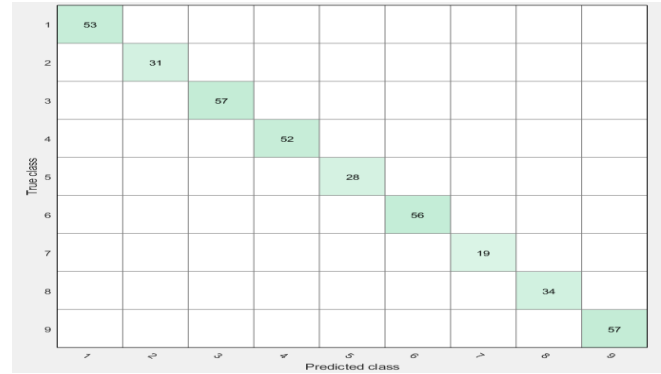
As seen from Table 1, FKNN, QSVM, CSVM, MGSVM and ESKNN classifiers achieved 100.0% ACC. Table 1 clearly demonstrates that the used 5 of 10 classifiers achieve the best ACC. The worst classifiers was FT according to ACC. Ensemble classifiers has high training time because their training times are higher than 9 second. The fastest classifier was LD and it trained the selected feature set in 0.64 second and it achieved 99.48% success rate. Confusion matrixes of the used classifiers were shown as below (Fig 2a-j).

	1	2	3	4	5	6	7	8	9
1	40	1		7	2	1		1	1
2		29		1	1				
3	4		47				1	1	4
4	5	2	1	33	2	2	1	1	5
5	3		2	4	13	1	2	2	1
6	2		4	4	1	44	1		
7	1			2	1		13	1	1
8	1		4	2	2	4		21	
9	2	1	1	3	2		1		47

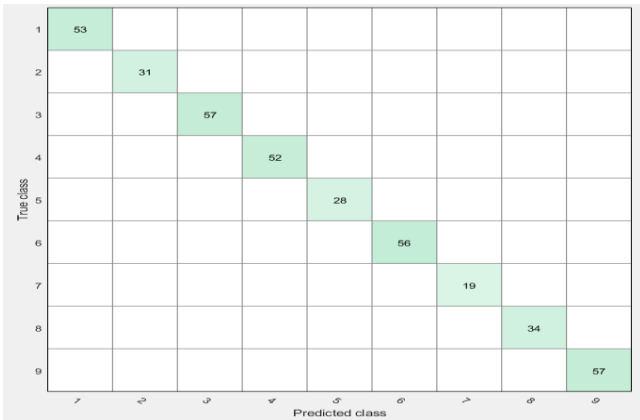
(a) Confusion matrix of FT.



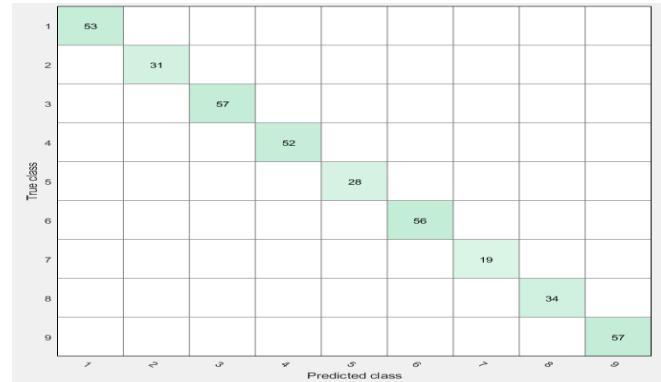
(b) Confusion matrix of LD.



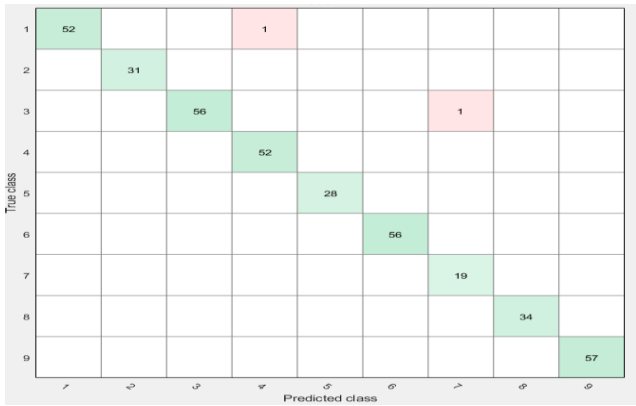
(e) Confusion matrix of QSVM.



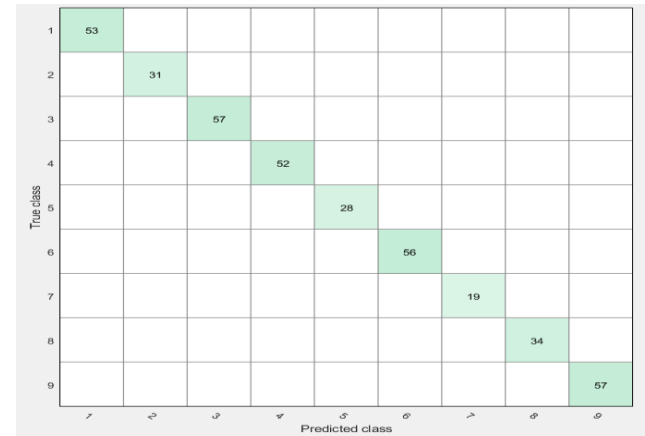
(c) Confusion matrix of FKNN.



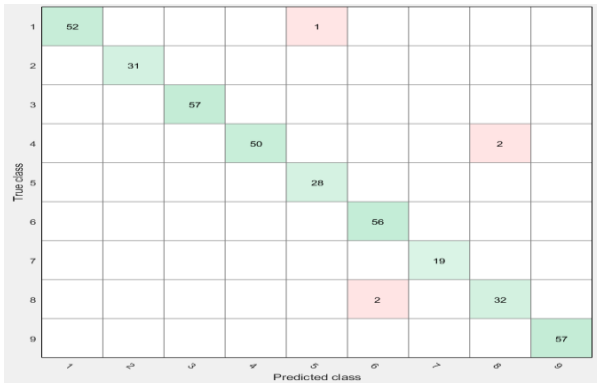
(f) Confusion matrix of CSVM.



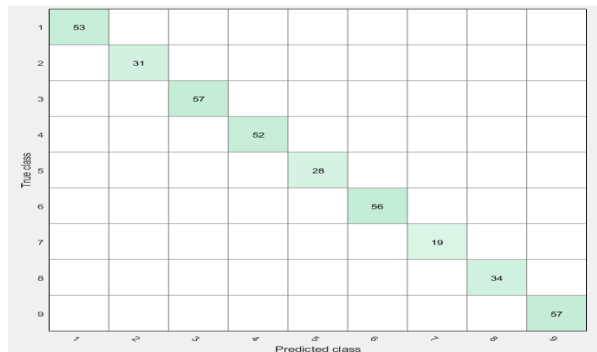
(d) Confusion matrix of WKNN.



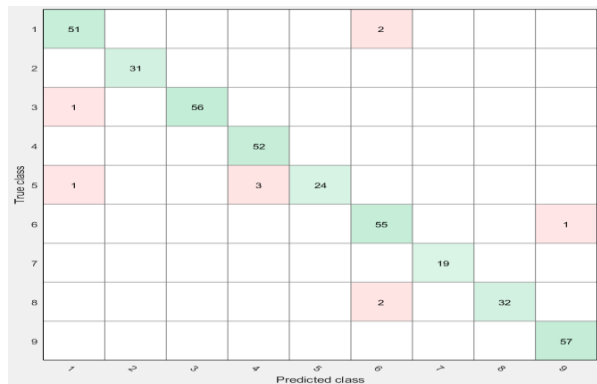
(g) Confusion matrix of MGSVM.



(h) Confusion matrix of ESD.



(i) Confusion matrix of ESKNN.



(j) Confusion matrix of EBT.

Figure 2a-j. Confusion matrixes of the used classifiers

It was indicated that the chromosome numbers of *Astragalus* were varied from $x=7,8,11-15$ and it was suggested that the basic chromosome numbers can be used as taxonomical tool to distinguish the *Astragalus* taxa (Sheidai et al., 2009; Gedik et al., 2019). A karyological study done by Gedik et al. (2019) demonstrated that *A. campylorhynchus*, *A. suberosus*, *A. densifolius* subsp. *densifolius* (has sat-chromosomes), *A. cretaceus*, *A. leporinus* var. *hirsutus*, *A. anthylloides*, *A. odoratus* have $2n=16$ while *A. lamarckii* has $2n=32$ and *A. camptoceras*, $2n = 2x = 16$ and $2n = 4x = 32$ tetraploid chromosomes. Additionally, it was shown that *A. cretaceus* and *A. densifolius* subsp. *densifolius* were located same section according to the

Flora of Turkey (Davis, 1988), And also, Emre et al. (2011) demonstrated that *A. camptoceras*, *A. suberosus*, *A. densifolius* and *A. cretaceus* have similar total and some individual saturated and unsaturated fatty acid compositions. However, it was showed that the used all of classifiers except for FT classified successfully separated and classified *Astragalus* taxa based on chromosome images (Table 1; Figure 2a-j).

4. Conclusions

In this study, a novel HOG based exemplar pyramid feature extraction method is presented. The main goal of the proposed HOG based exemplar pyramid iterative feature extraction is to generate distinctive features of the *Astragalus* species by using chromosome images. HOG is chosen as feature extractor and it generates features from each exemplar. By using pyramid method, features are extracted from exemplar of image and whole image. NCA reduced dimension of the extracted and concatenated features from 110,484 to 128. To illustrate success of the HOG based exemplar pyramid feature extraction method, 10 classifiers were chosen and five of them achieved 100.0% classification accuracy. Training times of the used classifiers were also listed in Table 1 to comprehensively comparison. Merits of the automated *Astragalus* chromosome image classification method;

- An *Astragalus* chromosome Image dataset is collected. This dataset acquires images of the 9 specifies.
- 100.0% classification accuracy was achieved. Therefore, it was suggested that the HOG can be contribute to taxonomical studies in addition to traditional taxonomical approaches including morphological and biochemical parameters.
- A cognitive biological image classification method is presented because there is no need set millions parameters.
- The proposed method has a high performance because 100.0% CA was obtained.
- Novel automated specifies classification application can be developed by using the proposed method.



References

- Albayrak, S. and Kaya, O., 2019. Antioxidant, Antimicrobial and Cytotoxic Activities of Endemic *Astragalus argaeus* Boiss. From Turkey. Hacettepe J. Biol. & Chem., 47 (1), 87-97.
- Çeçen, Ö., Aytaç, Z., and Mısırdalı, H., 2016. *Astragalus unalii* (Fabaceae), A New Species from Turkey. Turkish Journal of Botany, 40, 81-86.
- Ebrahimzadeh, R., and Jampour, M., 2014. Efficient Handwritten Digit Recognition Based On Histogram of Oriented Gradients and SVM. International Journal of Computer Applications (0975 - 8887), 104(9), 10-13.
- Elci, S., 1982. Observations and Reserach Methods in Cytogenetics. Fırat University Press, Elazig.
- Emre, İ., Şahin, A., Türkoğlu, İ., Yılmaz, Ö., Bahşi, M., and Kurşat, M., 2011. Compositions of Seed Fatty Acids in Some *Astragalus* L. Taxa from Turkey, Acta Botanica Gallica, 158(4), 487-491.
- Fernandes, F., Weigel, L., Jung, C., Navaux, P., Carro, L., and Rech, P., 2016. Evaluation of Histogram of Oriented Gradients Soft Errors Criticality for Automotive Applications. ACM Transactions on Architecture and Code Optimization, 13 (4), 38:2-38:25.

- Gedik, O., Kurşat, M., and Kiran, Y., 2019. Karyological Studies On Nine *Astragalus* L. taxa in Turkey. *KSÜ Tarım ve Doğa Dergisi*, 22(1), 35-44.
- Grinblat, G., Uzal, L.C., Larese, M.G., and Granitto, P.M. 2016. Deep Learning for Plant Identification Using Vein Morphological Patterns. *Computers and Electronics in Agriculture Journal*, 127,418-424.
- Kayhan, G. and Ergün, E. 2020. Medicinal and Aromatic Plants Identification Using Machine Learning Methods. *Balkan Journal of Electrical & Computer Engineering*, 8 (1), 81-87.
- Liu, N. and Kan, J.M., 2016. Improved Deep Belief Networks and Multifeature Fusion for Leaf Identification. *Neurocomputing*, 216, 460–467.
- Naresh, Y.G. and Nagendraswamy, H.S., 2016. Classification of Medicinal Plants: An Approach Using Modified Lbp with Symbolic Representation. *Neurocomputing*, 173,1789–1797.
- Sheidai, M., Shahin, Z., and Jalal, I., 2009. New Chromosome Number Reports in Tragacanthic *Astragalus* Species. *Caryologia*, 62(1), 30-36.
- Sing, M.M. and Singh, T.R. 2021. A Survey On Different Methods for Medicinal Plants Identification and Classification System. *Revista Geintec*, 11(4), 3191-3202.
- Siraj, F., Salahuddin, M.A., and Yusof, S.A.M., 2010. Digital Image Classification for Malaysian Blooming Flower. *Second International Conference on Computational Intelligence, Modelling and Simulation*, 33-38.
- Sun, Y., Liu, Y., Wang, G., Zhang, H., 2017. Deep Learning for Plant Identification in Natural Environment. *Computational Intelligence and Neuroscience*, 1-6.
- Uchida, S., 2013. Image Processing and Recognition for Biological Images. *Develop. Growth Differ.*, 55, 523–549.
- Wäldchen, J. and Mäder, P. 2018. Machine Learning for Image Based Species Identification. *Methods in Ecology and Evolution*, 9, 2216-2225.
- Wang, Z., Li, H., Zhu, Y., and Xu, T.F., 2017. Review of Plant Identification Based On Image Processing. *Arch Computat Methods Eng.*, 24, 637–654.
- Yigit, E., Sabanci, K., Toktas, A., and Kayabasi, A., 2019. A Study On Visual Features of Leaves in Plant Identification Using Artificial Intelligence Techniques. *Computers and Electronics in Agriculture*, 156, 369–377.



The effect of different earthquake ground motion level on performance of reinforced-concrete structures

Ercan IŞIK^{a,*} , Eyyüp DEMIRKIRAN^b 

^a Bitlis Eren University, Department of Civil Engineering, TR-13000, Bitlis Turkey

^b Bitlis Eren University, Department of Civil Engineering, TR-13000, Bitlis Turkey

ARTICLE INFO

Article history:

Received 15 June 2021

Received in revised form 10 October 2021

Accepted 14 October 2021

Keywords:

Earthquake

Ground motion level

TBEC-2018

Site-specific

ABSTRACT

Four different earthquake ground motion levels with different probabilities of exceedance were expressed with the current seismic design code. In this study, earthquake-structural parameters were obtained by taking into account four different ground motion levels for four different provinces with different earthquake hazards. Structural analyses were carried out using different earthquake ground motion levels obtained for each province. In the structural analysis, a sample reinforced-concrete structure with the same structural characteristics was selected. The results were obtained by using both ground motion levels and design spectra for four provinces. With this study, both the earthquake hazard and the ground motion level change were examined separately. It was determined that the two variables significantly changed the target displacement values expected from the structure.

© 2020. Turkish Journal Park Academic. All rights reserved.

1. Introduction

Renewal and improvement is inevitable in earthquake resistant building design rules over time. In addition, since the building and construction technologies have developed, the rules related to these should also be added to the seismic design codes. In this context, this process continued in Turkey with the studies carried out over time. Earthquake resistant building design rules, which started in the 1940s, were renewed on different dates and used within the scope of structural design, analysis and evaluation. The seismic design code, which has been used since 2007, was finalized in 2018 with the necessary updates and additions. One of the important additions was made at earthquake ground motion levels. In the previous code, only earthquake ground motion level, which had a recurrence period of 475 years and was expressed as a standard design earthquake, was used. However, with the current code, four different earthquake ground motion levels with different recurrence periods and exceedance probabilities have been specified. The earthquake parameter and design spectra differ for each ground motion level.

The usage of site-specific design spectra is also one of the important updates with current code. Seismicity parameters and design spectra are obtained specifically for any location and show differences with this update. The design spectra can be obtained by using the local soil conditions and seismicity parameters of any location together (Işık et al., 2020; Karaşın et al., 2020). The differentiation of the design spectra significantly effects the expected target displacements from the buildings. Damage estimation and realistic performance of buildings depend on the correct determination of design spectra (Kutanis et al., 2018; Işık et al., 2016).

There are many studies examining the changes between the last two regulations. In these studies, earthquake force calculation methods, base shear forces, displacements, period, target displacements, spectrum curves and section damage values were examined and compared (Işık et al., 2021; Aksoylu et al., 2020; Aksoylu and Arslan, 2021; Keskin and Bozdoğan, 2018; Koçer et al., 2018; Bozer, 2020; Ulutaş, 2019; Adar et al., 2021; Seyrek, 2020; Büyüksaraç et al., 2021; Başaran, 2018; Nemutlu and Sarı, 2018; Işık et al., 2021a; Yalın and Ulutaş, 2021; Peker ve Işık, 2021; Akyıldız et al., 2021). In the study conducted by Başaran and Hiçyılmaz (2020), the effects of

* Corresponding author. Tel.: +0 434 222 0030; fax: +0 434 222 9145

E-mail address: eisik@beu.edu.tr

ORCID : 0000-0001-8057-065X (E.Işık), 0000-0002-3268-9733 (E.Demirkıran)

different earthquake ground motion levels on reinforced-concrete frames were examined. The results obtained by considering different local ground conditions and four different ground motion levels for Afyon province were compared.

Within the scope of this study, four different provinces located in different earthquake zones were selected and earthquake-structure parameters were obtained for four different earthquake ground motion levels for each province. Design spectra were obtained by considering different ground motion levels for each province. Structural analyses were carried out using these obtained design spectra. Base shear forces, elastic and effective stiffness values and target displacement values expected from the structure were obtained for four different ground motion levels, separately. Two different variables were selected in this study such four different provinces located in different earthquake zones and four different ground motion levels. In this study, the interaction of these two variables was tried to be examined.

2. Comparison of Earthquake Parameters

While selecting different provinces within the scope of this study, four different provinces located in different earthquake zones were selected in the previous earthquake zone map. As Erzincan 1st degree earthquake zone; Adana is a 2nd degree earthquake zone; Gümüşhane was chosen as the 3rd degree earthquake zone and Ankara as the 4th degree earthquake zone. The representation of these selected provinces on the current earthquake hazard map is given in Figure 1.

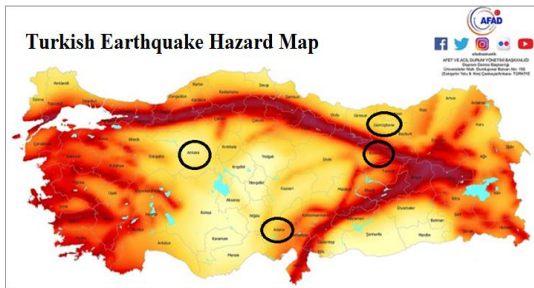


Figure 1. Turkish Earthquake Hazard Map and the studied locations

In TSDC-2007, while only the standard design earthquake ground motion with a recurrence period of 475 years and a probability of exceedance of 10% in 50 years was taken into account, three more ground motion levels with a probabilities of exceedance in 50 years were added in the current code. Four different earthquake ground motion levels in the current code are given in Table 1.

Table 1. Earthquake ground motion levels (TEBC-2018)

Earthquake Level	Recurrence Period	Probability of Exceedance	Description
DD-1	2475	2%	Largest earthquake
DD-2	475	10%	Standard earthquake
DD-3	72	50%	Frequent earthquake
DD-4	43	68%	Service earthquake

Earthquake parameters for any geographic location can be obtained very easily and practically with the help of Turkey Earthquake Hazard Maps Interactive Web Application. The application gives earthquake parameters and design spectra, taking into account the earthquake ground motion level and local soil classes, in accordance with the current code. In this study, the ZC local soil type in TBEC-2018 was taken into account in order to reveal the changes in the structural analysis results. The peak ground acceleration (PGA), the peak ground velocity (PGV), map spectral acceleration coefficients (S_s and S_1), local ground effect coefficients (F_s and F_1) for four different provinces were obtained for different ground motion levels. The design spectral acceleration coefficients (S_{DS} and S_{D1}) were obtained separately. Horizontal and vertical elastic design spectra were obtained with the help of the application. The comparison of PGA and PGV values for different earthquake ground motion levels is shown in Table 2.

Table 2. The comparison of PGA and PGV for selected provinces

Province	PGA (g)				PGV(cm/s)			
	Probability of exceedance in 50 years				Probability of exceedance in 50 years			
	2%	10%	50%	68%	2%	10%	50%	68%
Erzincan	1.09	0.60	0.22	0.15	74.61	39.34	12.4	8.38
Adana	0.45	0.23	0.08	0.06	24.16	11.33	4.56	3.29
Gümüşhane	0.35	0.18	0.07	0.05	21.95	11.89	5.26	3.71
Ankara	0.30	0.15	0.06	0.04	17.93	10.17	4.33	3.16

The comparison of the short period map spectral acceleration coefficient (S_s) and the map spectral acceleration coefficient (S_1) for the 1.0 second period for different probabilities of exceedance in 50 years are shown in Table 3.

Table 3. Comparison of map spectral acceleration coefficients

Province	S_s				S_1			
	Probability of exceedance in 50 years				Probability of exceedance in 50 years			
	2%	10%	50%	68%	2%	10%	50%	68%
Erzincan	2.71	1.44	0.50	0.33	0.84	0.41	0.13	0.09
Adana	1.07	0.53	0.19	0.13	0.26	0.13	0.05	0.04
Gümüşhane	0.85	0.43	0.16	0.11	0.26	0.13	0.06	0.04
Ankara	0.70	0.35	0.13	0.09	0.21	0.12	0.05	0.04

The comparison of spectral acceleration coefficients was made only for DD-2 ground motion level. The reason for this is that in the previous earthquake code, only the ground motion level with a recurrence period of 475 years and a probability of exceedance 10% in 50 years was used. The comparison of the spectral acceleration coefficients according to the last two seismic design codes is shown in Table 4. No comparisons were

made in the vertical direction since there were no vertical values in the previous code.

Table 4. Comparison of spectral acceleration coefficients

PROVINCE	Spectral Acceleration Coefficient				Corner Periods			
	All soil types		ZC		ZC		ZC	
	TSDC-2007		TBEC-2018		TSDC-2007		TBEC-2018	
	S _{DS}	0.40S _{DS}	S _{DS}	0.40S _{DS}	T _A	T _B	T _A	T _B
Erzincan	1	0.40	1.726	0.690	0.15	0.60	0.072	0.360
Adana	0.75	0.30	0.682	0.273	0.15	0.60	0.058	0.288
Gümüşhane	0.50	0.20	0.554	0.223	0.15	0.60	0.081	0.404
Ankara	0.25	0.10	0.448	0.179	0.15	0.60	0.080	0.401

With the updated code, local ground effect coefficients (F_S and F₁) were used for the first time. The short period map spectral acceleration coefficient for the period of 0.2 s (S_S) and map spectral acceleration coefficient for the period of 1.0 s (S₁) was also obtained for all locations. Horizontal elastic design acceleration spectrum corner period (T_A and T_B) and vertical elastic design acceleration spectrum corner period (T_{AD} and T_{BD}) were obtained from the application. The results obtained for the same ground motion levels for four different provinces with different seismicity characteristics and considered within the scope of the study were also compared. The comparison of the earthquake parameters obtained for DD-1, which is called the largest earthquake, is shown in Table 5.

Table 5. The comparison of earthquake parameters for DD-1

Province	F _S	F ₁	S _{DS}	S _{D1}	T _A	T _B	T _{AD}	T _{BD}
Erzincan	1.200	1.400	3.256	1.169	0.072	0.359	0.024	0.120
Adana	1.200	1.500	1.283	0.387	0.060	0.302	0.020	0.101
Gümüşhane	1.200	1.500	1.015	0.393	0.077	0.387	0.026	0.129
Ankara	1.221	1.500	0.851	0.318	0.075	0.374	0.025	0.125

The comparison of the earthquake parameters obtained for DD-2, which is called the standard design earthquake, is shown in Table 6.

Table 6. The comparison of earthquake parameters for DD-2

Province	F _S	F ₁	S _{DS}	S _{D1}	T _A	T _B	T _{AD}	T _{BD}
Erzincan	1.200	1.500	1.726	0.621	0.072	0.360	0.024	0.120
Adana	1.288	1.500	0.682	0.197	0.058	0.288	0.019	0.096
Gümüşhane	1.300	1.500	0.554	0.224	0.081	0.404	0.027	0.135
Ankara	1.300	1.500	0.448	0.180	0.081	0.404	0.027	0.135

The comparison of the earthquake parameters obtained for DD-3, which is called the frequent earthquake, is shown in Table 7. DD-4, which is called the service earthquake, is shown in Table 8.

Table 7. The comparison of earthquake parameters for DD-3

Province	F _S	F ₁	S _{DS}	S _{D1}	T _A	T _B	T _{AD}	T _{BD}
Erzincan	1.300	1.500	0.650	0.199	0.061	0.307	0.020	0.102
Adana	1.300	1.500	0.246	0.076	0.062	0.311	0.021	0.104
Gümüşhane	1.300	1.500	0.204	0.091	0.090	0.448	0.030	0.149
Ankara	1.300	1.500	0.169	0.076	0.091	0.453	0.030	0.151

Table 8. The comparison of earthquake parameters for DD-4

Province	F _S	F ₁	S _{DS}	S _{D1}	T _A	T _B	T _{AD}	T _{BD}
Erzincan	1.300	1.500	0.434	0.129	0.059	0.297	0.020	0.099
Adana	1.300	1.500	0.168	0.054	0.064	0.322	0.021	0.107
Gümüşhane	1.300	1.500	0.140	0.065	0.092	0.459	0.031	0.153
Ankara	1.300	1.500	0.122	0.056	0.091	0.454	0.030	0.151

Comparison of horizontal and vertical elastic design spectra obtained for different earthquake ground motion levels for the provinces considered in the study was also made. Comparison of the design spectra obtained for different ground motion levels for the province of Erzincan is shown in Figure 2.

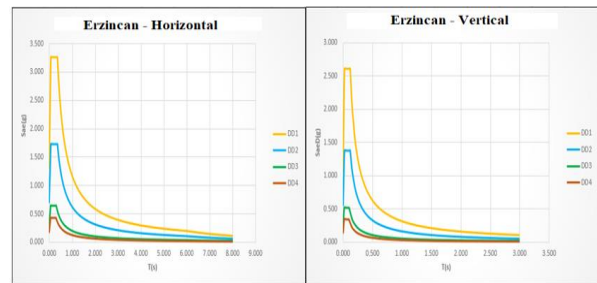


Figure 2. Comparison of the design spectra obtained for different ground motion levels for Erzincan province

The comparison of the horizontal and vertical elastic design spectra obtained for the DD-2 ground motion level, which is the standard design earthquake, for four different provinces is shown in Figure 3.

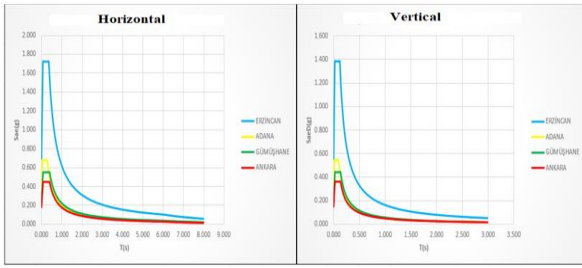


Figure 3. Comparison of the design spectra obtained for different ground motion levels for all provinces

The earthquake parameters obtained for different earthquake ground motion levels have taken different values for provinces with different seismicity conditions for same local soil type. In addition, earthquake parameters changed as the probability of exceedance in 50 years changed for each province. Among the provinces considered within the scope of the study, the map PGA, PGV and map spectral acceleration coefficients (S_s and S_1) had the highest values in Erzincan. The lowest values were obtained for Ankara. The local soil coefficients F_s and F_1 values were equal to each other except for very slight differences, since the local soil type did not change. The variation of the local soil coefficients (F_s and F_1) directly affects the S_{DS} and S_{D1} parameters. The short period design spectral acceleration coefficient (S_{DS}) has the highest value in Erzincan and the lowest value in Ankara.

3. Comparison of Structural Analyses Parameters

Pushover analysis is the one of the commonly used approaches to determine the seismic capacities of buildings in the design and evaluation of structures (Estêvão and Oliveira, 2015; Ademović et al., 2013; Karakaš et al., 2018; Bilgin and Frangu, 2017). This type of analysis was also used in this study. Typical pushover curve and all displacements calculated for structural analysis are shown in Figure 4.

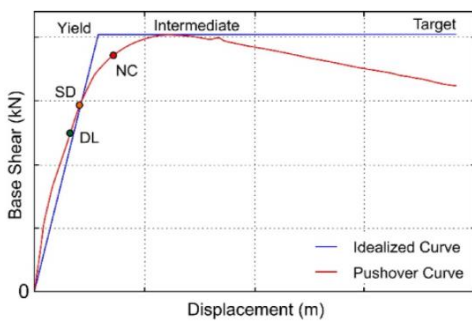


Figure 4. Typical pushover and idealized curves and calculated displacements

In performance-based earthquake engineering, it is important to determine target displacements for damage estimation when certain performance limits of structural elements are reached. In the structural analysis, limit states given in Eurocode-8 (Chapter 3) (Eurocode, 2005; Pinto and Franchin, 2011) for worldwide used damage estimation were taken into account. Accordingly, the proposed limit states are shown in Table 9.

Table 9. Limit states in Eurocode 8 (Part3)

Limit State	Description
Damage Limitation (DL)	Only lightly damaged, damage to non-structural components economically repairable
Significant Damage (SD)	Significantly damaged, some residual strength and stiffness, non-structural components damaged, uneconomic to repair
Near Collapse (NC)	Heavily damaged, very low residual strength and stiffness, large permanent drift but still standing

A 6-storey reinforced-concrete building was chosen as an example. Since the structure was chosen as symmetrical, structural analyses were carried out only in the X direction with Seismostruct software (Seismosoft, 2018). There is no irregularity in the selected reference building. In the RC sample building model, C25-S420 was chosen as the material. $\phi 10/10$ is chosen as transverse reinforcement for both columns and beams. The longitudinal reinforcement for the columns is $4\phi 20$ at the corners and $8\phi 16$ for the other longitudinal reinforcements. For the beams, $4\phi 14$ was chosen in the lower and upper regions and $2\phi 12$ was chosen as the body reinforcement. The blueprint of the considered reinforced-concrete structure is given in Figure 5.

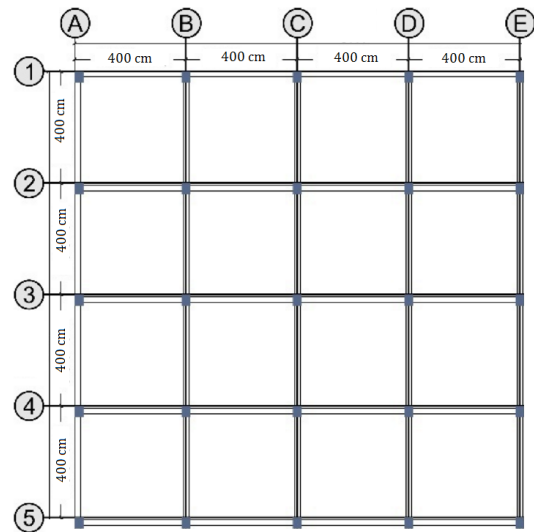


Figure 5. The blueprint of sample RC building

The 3D finite element model of the sample RC building is given in Figure 6.

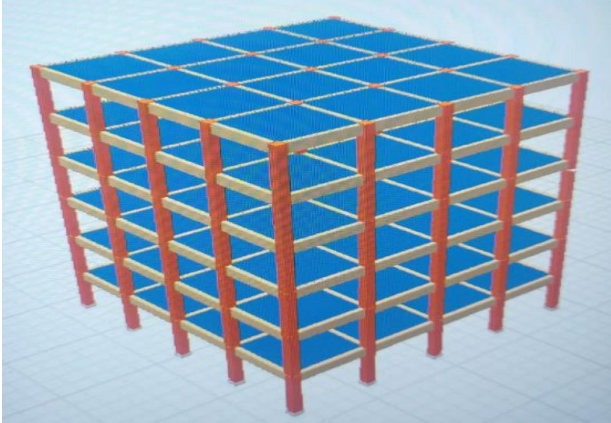


Figure 6. The 3D model of the sample building

The sample RC building was analysed in all provinces without changing its structural properties. The natural vibration period for the sample RC building was obtained as 0.351 s for all provinces and all ground motion levels.

Comparison of structural results obtained for DD-1 ground motion level was shown in Table 10; comparisons for DD-2 ground motion level was in Table 11; the comparison of the results for the DD-3 ground motion level was shown in Table 12 and the comparison of the results obtained when the DD-4 ground motion level was shown in Table 13. The elastic stiffness value (K_{elas}) and effective stiffness (K_{eff}) values for each structural model were obtained directly using the stiffness reduction coefficients predicted in the algorithm.

Table 10. Comparison of results for DD-1 ground motion level

Province	Base Shear (kN)	K_{elas}	K_{eff}	DL	SD	NC
Erzincan	6434.74	174945.59	82880.23	0.137	0.179	0.318
Adana	6434.74	174945.59	82880.23	0.053	0.068	0.124
Gümüşhane	6434.74	174945.59	82880.23	0.042	0.054	0.095
Ankara	6434.74	174945.59	82880.23	0.035	0.045	0.078

Table 11. Comparison of results for DD-2 ground motion level

Province	Base Shear (kN)	K_{elas}	K_{eff}	DL	SD	NC
Erzincan	6434.74	174945.59	82880.23	0.071	0.093	0.169
Adana	6434.74	174945.59	82880.23	0.027	0.035	0.061
Gümüşhane	6434.74	174945.59	82880.23	0.022	0.028	0.048
Ankara	6434.74	174945.59	82880.23	0.018	0.023	0.039

Table 12. Comparison of results for DD-3 ground motion level

Province	Base Shear (kN)	K_{elas}	K_{eff}	DL	SD	NC
Erzincan	6434.74	174945.59	82880.23	0.026	0.033	0.057
Adana	6434.74	174945.59	82880.23	0.010	0.0128	0.022
Gümüşhane	6434.74	174945.59	82880.23	0.008	0.011	0.018
Ankara	6434.74	174945.59	82880.23	0.007	0.009	0.015

Table 13. Comparison of results for DD-4 ground motion level

Province	Base Shear (kN)	K_{elas}	K_{eff}	DL	SD	NC
Erzincan	6434.74	174945.59	82880.23	0.018	0.0230	0.039
Adana	6434.74	174945.59	82880.23	0.0068	0.0087	0.015
Gümüşhane	6434.74	174945.59	82880.23	0.006	0.0073	0.013
Ankara	6434.74	174945.59	82880.23	0.005	0.006	0.011

There was no change in the natural vibration period for the sample RC building with the same structural properties, since the structural properties did not change. This situation remained valid for the base shear force, elastic and effective stiffness values of the structure and no change was obtained. The target displacement values expected from the structure at different earthquake ground motion levels for each province have changed significantly. As the probability of exceedance for the province decreases, that is, in case of larger earthquakes, the displacement demands have taken on higher values. These values decreased in smaller earthquakes that were more frequent. When the values obtained for different provinces are compared, in case the PGA values increase, the displacement values to be used in the performance evaluation of the buildings also increased significantly. DD-2 earthquake ground motion with a recurrence period of 475 years and a probability of exceedance of 10% in 50 years, which is the standard design earthquake level, is taken into account as an example for the comparisons between the maximum ground acceleration (PGA) obtained and the target displacements. The comparison of PGA values and target displacement values obtained for this ground motion level is shown in Table 14.

Table 14. Comparison of PGA and target displacement values

Province	PGA (g)	DL	SD	NC
Erzincan	0.598	0.071	0.093	0.169
Adana	0.232	0.027	0.035	0.061
Gümüşhane	0.182	0.022	0.028	0.048
Ankara	0.149	0.018	0.023	0.039

4. Conclusions

Earthquake ground motion levels are expressed with different probabilities of exceedance with the current seismic design code. The number of one ground motion level in the previous code was increased to four. Within the scope of this study, four different ground motion levels specified in the current seismic design code were chosen as the first variable. In addition, with the current code, earthquake parameter and site-specific design spectra for studied geographical location are obtained. Four different geographical locations were chosen as the second variable. Erzincan for the 1st degree earthquake zone; Adana for the 2nd degree earthquake zone; Gümüşhane for the 3rd degree earthquake zone and Ankara for the 4th degree earthquake zone was taken into consideration. Firstly, earthquake parameters were obtained for both ground motion levels and provinces. Structural analyses were carried out for a sample RC building using the obtained design spectra.

Since the structural properties did not change, there was no change in the base shear forces, elastic and effective stiffness values obtained. However, as the design spectrum values changed, the target displacement values used for damage estimation in structures changed significantly. This has once again revealed that the performance levels and damage estimates for the structures will be more realistic. In this context, it shows that the usage of site-specific design spectra with the current code is an important gain.

Percentages of change between TSDC-2007 and TBEC-2018 in the design spectral acceleration coefficient (S_{DS}) for ZC local soil for the short period; 72.6% in Erzincan, 9.07% in Adana, 10.8% in Gümüşhane and 79.2% in Ankara. Design spectral acceleration coefficient (S_{D1}) for 1.0 second period, percentages of change between TSDC-2007 and TBEC-2018 for ZC local ground; Erzincan province has 72.5%, Adana province 9.0%, Gümüşhane province 11.5% and Ankara province 79.0%. The percentages of change for the design spectral acceleration coefficient for the short period of the values obtained from DD-1, which is called the largest earthquake, to DD-4, which is the service earthquake ground motion level; There is a decrease of 86.67% in the province of Erzincan, 86.91% in the province of Adana, 86.21% in the province of Gümüşhane and 85.66% in the province of Ankara.

For the peak ground acceleration (PGA) value, as the probability of exceedance in 50 years increases by 2%, 10%, 50%, 68%; there is a decrease of 86.49% in Erzincan, 87.33% in Adana, 86.44% in Gümüşhane and 85.81% in Ankara. For the peak ground velocity (PGV) value, as the probability of exceedance in 50 years increases by 2%, 10%, 50%, 68%; there is a decrease of 88.76% in Erzincan, 86.40% in Adana, 83.09% in Gümüşhane and 82.36% in Ankara.

If the same local soil condition is taken into account, the short period map acceleration coefficient (S_s) increases as the probability of exceedance in 50 years increases according to 2%, 10%, 50%, 68% at different earthquake ground motion levels; there is a decrease of 87.67% in Erzincan, 87.93% in Adana, 87.23% in Gümüşhane and 86.51% in Ankara. The map spectral acceleration coefficient (S_1) for the 1.0 second period increases as the probability of exceedance in 50 years

increases according to 2%, 10%, 50%, 68% at different earthquake ground motion levels; there is a decrease of 89.70% in Erzincan, 86.05% in Adana, 83.59% in Gümüşhane and 82.55% in Ankara.

Percentage of change in target displacement values from DD-1 to DD-4 for different earthquake ground motion levels for each province; Erzincan province DL 86.86%, SD 87.15%, NC 87.84%; Adana province DL 87.17%, SD 87.21%, NC 87.90%; Gümüşhane province DL 85.71%, SD 86.48%, NC 86.73% and Ankara province DL 85.71%, SD 86.67%, NC 85.90%.

Acknowledgements

This study was produced from master thesis of second author

References

- Adar, K., Büyüksarac, A., Işık, E., and Ulu, A.E., 2021. Comparison of 2007 and 2018 Seismic Codes in the Scope of Structural Analysis. *European Journal of Science and Technology*, 25, 306-317.
- Ademovic, N., Hrasnica, M., and Oliveira, D.V., 2013. Pushover Analysis and Failure Pattern of a Typical Masonry Residential Building in Bosnia and Herzegovina. *Engineering Structures*, 50, 13-29.
- Aksoyly, C., Mobark, A., Arslan, M.H., and Erkan, İ.H., 2020. A Comparative Study on ASCE 7-16, TBEC-2018 and TEC-2007 for Reinforced Concrete Buildings. *Revista de la Construcción*, 19(2), 282-305.
- Aksoyly, C., and Arslan, M.H., 2021. 2007 ve 2019 Deprem Yönetmeliklerinde Betonarme Binalar İçin Yer Alan Farklı Deprem Kuvveti Hesaplama Yöntemlerinin Karşılaştırılması Olarak İrdelenmesi. *International Journal of Engineering Research and Development*, 13(2), 359-374.
- Aksoyly, C. and M.H. Arslan. 2019. Çerçeve Türü Betonarme Binaların Periyod Hesaplarının Farklı Ampirik Bağlıtlara Göre İrdelenmesi. *Bitlis Eren Üniversitesi Fen Bilimleri Dergisi* 8(2), 569-581.
- Akyıldız, M.H., Ulu, A.E., Adar, K. 2021. TBDY-2018'deki Yerel Zemin Koşullarının Deprem Kesit Tesirlerine Etkisi. *Dicle Üniversitesi Mühendislik Fakültesi Mühendislik Dergisi*, 12(4), 679-687.
- Available online: <https://tdth.afad.gov.tr> (accessed on 2 May 2021).
- Başaran, V., 2018. Türkiye Bina Deprem Yönetmeliğine (TBDY2019) göre Afyonkarahisar için Deprem Yüklerinin Değerlendirilmesi. *Afyon Kocatepe Üniversitesi Fen ve Mühendislik Bilimleri Dergisi* 18(3), 1028-1035.
- Başaran, V., and Hiçyılmaz, M., 2020. Betonarme Çerçevelerde Farklı Deprem Yer Hareketi Düzeyi Etkilerinin İncelenmesi. *Journal of Innovations in Civil Engineering and Technology*, 2(1), 27-41.
- Bilgin, H., and Frangu, I., 2017. Predicting the Seismic Performance of Typical R/C Healthcare Facilities: Emphasis on Hospitals. *International Journal of Advanced Structural Engineering*, 9(3), 277-292.
- Bozer, A., 2020. Tasarım Spektral İvme Katsayılarının DBYBHY 2007 ve TBDY 2018 Yönetmeliklerine Göre Karşılaştırılması. *Dicle Üniversitesi Mühendislik Fakültesi Mühendislik Dergisi*, 11(1), 393-404.
- Buyuksarac, A., Isik, E., and Harirchian, E., 2021. A Case Study for Determination of Seismic Risk Priorities in Van (Eastern Turkey). *Earthquakes and Structures*, 20(4), 445-455.

- EN 1998-3 (2005). Eurocode-8: Design of Structures for Earthquake Resistance-Part 3: Assessment and Retrofitting of Buildings; European Committee for Standardization: Bruxelles, Belgium, 2005.
- Estêvão, J. M., and Oliveira, C.S. 2015. A new analysis method for structural failure evaluation. *Engineering Failure Analysis*, 56, 573-584
- Işık, E., Harirchian, E., Bilgin, H., Jadhav, K., 2021. The Effect of Material Strength and Discontinuity in RC Structures According to Different Site-Specific Design Spectra. *Research on Engineering Structures and Materials*, accepted paper.
- Işık, E., Ekinci, Y.L., Sayil, N., Buyuksarac, A., and Aydın, M.C., 2021. Time-dependent Model for Earthquake Occurrence and Effects of Design Spectra on Structural Performance: A Case Study from the North Anatolian Fault Zone, Turkey. *Turkish Journal of Earth Sciences*, 30(2), 215-234.
- Işık, E., Büyüksaraç, A., Ekinci, Y.L., Aydın, M. C., and Harirchian, E., 2020. The Effect of Site-Specific Design Spectrum on Earthquake-Building Parameters: A Case Study from the Marmara Region (NW Turkey). *Applied Sciences*, 10(20), 7247.
- Işık, E., Kutanis, M., and Bal, İ E., 2016. Displacement of the Buildings According to Site-Specific Earthquake Spectra. *Periodica Polytechnica Civil Engineering*, 60(1), 37-43.
- Karakaş, N., Kalman Šipoš, T., and Hadzima-Nyarko, M., 2018. Application of Different Seismic Analyses to RC Structures. *Electronic Journal of the Faculty of Civil Engineering Osijek-e-GFOS*, 9(17), 39-51.
- Karasin, İ.B., Işık, E., Demirci, A., and Aydın, M.C., 2020. Coğrafi Konuma Özel Tasarım Spektrumlarının Betonarme Yapı Performansına Etkisi. *Dicle Üniversitesi Mühendislik Fakültesi Mühendislik Dergisi*, 11(3), 1319-1330.
- Keskin, E., and Bozdoğan, K.B., 2018. 2007 ve 2018 Deprem Yönetmeliklerinin Kırklareli İli Özelinde Değerlendirilmesi. *Kırklareli Üniversitesi Mühendislik ve Fen Bilimleri Dergisi*, 4(1), 74-90.
- Koçer, M., Nakipoğlu, A., Öztürk, B., Al-hagri, M.G., and Arslan, M.H., 2018. Deprem Kuvvetine Esas Spektral İvme Değerlerinin TBDY 2018 ve TDY 2007'ye göre Karşılaştırılması. *Selçuk-Teknik Dergisi*, 17(2), 43-58.
- Kutanis, M., Ulutaş, H., and Işık, E., 2018. PSHA of Van Province for Performance Assessment Using Spectrally Matched Strong Ground Motion Records. *Journal of Earth System Science*, 127(7), 1-14.
- Nemutlu, Ö.F. and Sarı, A., 2018. Comparison of Turkish Earthquake Code in 2007 with Turkish Earthquake Code in 2018. *International Engineering and Natural Sciences Conference (IENSC 2018)*, Diyarbakır.
- Peker, F. U., Işık, E. 2021. TBDY-2018'deki Yerel Zemin Koşullarının Çelik Yapı Deprem Davranışına Etkisi Üzerine Bir Çalışma. *Bitlis Eren Üniversitesi Fen Bilimleri Dergisi*, 10(3), 1125-1139.
- Pinto, P.E.; Franchin, P., 2011. Eurocode 8-Part 3: Assessment and retrofitting of buildings. In *Proceedings of the Eurocode 8 Background and Applications, Dissemination of Information for Training*, Lisbon, Portugal.
- Seismosoft. SeismoStruct 2018-A Computer Program for Static and Dynamic Nonlinear Analysis of Framed Structures. 2018. Available online: <http://www.seismosoft.com>
- Seyrek, E., 2020. Yeni Türkiye Sismik Tehlike Haritasının Ege Bölgesi için Değerlendirilmesi. *Niğde Ömer Halisdemir Üniversitesi Mühendislik Bilimleri Dergisi*, 9(1), 414-423.
- TBEC-2018. Turkish Building Earthquake Code; T.C. Resmi Gazete: Ankara, Turkey, 2018.
- TSDC-2007. Turkish Seismic Design Code; T.C. Resmi Gazete: Ankara, Turkey, 2007.
- Ulutaş, H., 2019. DBYBHY (2007) ve TBDY (2018) Deprem Yönetmeliklerinin Kesit Hasar Sınırları Açısından Kıyaslanması. *Avrupa Bilim ve Teknoloji Dergisi*, (17), 351-359.
- Yalin, M., and Ulutaş, H., 2021. Mevcut Okul Türü bir Binanın Deprem Performansının 2007 ve 2018 Deprem Yönetmeliklerine göre Değerlendirilmesi. *Niğde Ömer Halisdemir Üniversitesi Mühendislik Bilimleri Dergisi*, 1-1.

Available online at www.dergipark.gov.tr/beuscitech

Journal of Science and Technology

E-ISSN 2146-7706



Using of light and scanning electron microscopy for pollen morphology of some *Epilobium* (Onagraceae) taxa and Its taxonomic importance

Birol BAŞER^{a,*} , Nazli AKAY^b , Murat KÜRŞAT^a 

^a Bitlis Eren University, Department of Biology, 13000, Bitlis, Turkey

^b Ministry of Family and Social Policies, Disability-Free Living, Care, Rehabilitation and Family Counseling Center, Ahlat, Bitlis, Turkey

ARTICLE INFO

Article history:

Received 29 September 2021

Received in revised form 21 October 2021

Accepted 04 November 2021

Keywords:

Epilobium,
LM,
Onagraceae,
Pollen morphology,
SEM

ABSTRACT

In this study, pollen morphologies of eleven species of the *Epilobium* L. genus belonging to Onagraceae family were investigated under light and scanning electron microscopy. Solutions to taxonomic problems of these species were sought with palynological information. The characteristics of the genus *Epilobium* L. studied as a result of palynological studies are as follows: It has been determined that their pollen grains have tetrad, angulaperturate, 3-zonoporate (rarely 2,4 porate), suboblate and oblate-spheroidal pollen shapes, and have baculate, baculate-rugulate, and rugulate ornamentation.

© 2021. Turkish Journal Park Academic. All rights reserved.

1. Introduction

The Onagraceae family having very rich and widespread genera and species are represented by nearly 20 genera and 656 species in the world (Raven, 1962a; Heywood et al., 2007). The genus *Epilobium* L. (Onagraceae) contains about 200 species that grow in the subarctic, temperate, and subantarctic regions in the world (Walter et al. 2007). *Epilobium* are mostly herbs. However, few of them are annual or perennial subshrubs. In total, 22 *Epilobium* species have been reported in Turkey (Okur 2019). *Epilobium* is a very difficult genus due to its very similar appearance and high probability of hybridization among almost all taxa (Makbul 2008).

Palinomorphy of Onagraceae has been examined by many authors (Erdtman, 1952; Mitroiu, 1963; Ting, 1966; Brown, 1967; Skvarla, et al., 1978-2008; Keri & Zetter, 1992; Praglowski et al., 1994; Rowley & Claugher, 1996; and Rowley & Skvarla, 2006). Mosquin (1966) examined two subspecies of *E. angustifolium* according to their morphology; *E. angustifolium*

L. subsp. *circumvagum* Mosquin taxon is tetraploid (n=36) and *E. angustifolium* L. subsp. *angustifolium* is diploid (n=18) and hexaploid (n=54). Tetraploid taxa with three and four pores, and diploid taxa having pollens with three pores are found together. Brown, (1967) stated that in the Epilobieae tribe, which also includes the *Epilobium* pollen grains are seen as either monads or tetrahedral tetrads. The pollen of tetraploid taxa is larger than the pollen of other taxa whereas, pollen grains with four pores are denser in hexaploid taxa. Punt et al., (2003) comprehensively studied pollen morphology of the Onagraceae from Northwest Europe. Skvarla et al., (2008) examined pollen morphology of *Epilobium luteum* of Onagraceae belonging to tribe Onagreae. Makbul et al., (2008) studied the anatomical and pollen morphological characters of the genus *Epilobium* from Northwest Anatolia and reported that anatomical features are more important than palynological features for explaining the variation among these taxa. Skvarla et al., (2008) observed that the pollen grains of the genus *Epilobium* has both monad and tetrahedral tetrad structure.

* Corresponding author. Tel.: +0 434 222 00 20

E-mail address: bbaser@beu.edu.tr

ORCID : 0000-0002-9305-8759 (B. Başer), 0000-0002-7367-9697 (N. Akay), 0000-0002-0861-4213 (M. Kürşat)

Punt et al., (2003) and Makbul et al., (2008) determined that the pollen shape of the *Epilobium* taxon was suboblate or oblate and the pollen shape contributed significantly to the differentiation of the *Epilobium* taxon. Erdtman, 1960; Punt et al., 2003 revealed that there is a fine connection between the tetrad and monad pollen spreads by breaking this connection with the acetolysis method. Rahimi et al., (2018) determined that radial symmetrical, tetrahedral tetrad, trizonoporate, rugulate, granulate, verrucate, and striate ornamentations were observed in pollens and that these family members did not differ significantly in terms of characteristics such as pollen size, shape, and pore structure. Perveen and Qaiser (2013) determined that the pollen distribution of *Epilobium* is generally tetrahedral tetrad and rarely monad.

The aim of the study is to perform pollen morphology analyses of 11 different taxa belonging to *Epilobium* by using light and scanning electron microscopy methods and to clarify the usefulness of these features in terms of taxonomic implications.

2. Materials and Methods

Plant specimens was obtained from the specimens of Gazi University herbarium (GAZI) and Bitlis Eren University Herbarium. The list of voucher specimens is deposited in GAZI and Bitlis Eren University Herberia.

Specimens investigated.

***E. hirsutum* L.:** B8-Bitlis: Bitlis Ağačköprü Village and stream sides, 26.07.2013, 38° 20' 11.95" K, 42° 00' 10.88" D, 1350-1450m, M. Karataş 1304, Det.: M. Kurşat. ***E. parviflorum* Schreb.:** B8-Bitlis: Bitlis, Kambos Mountain north slope, 18.07.2014, 38° 19' 23.26" K, 41° 59' 42.29" D, 1800-1950m, M. Karataş 2318, Det.: M. Kurşat. ***E. minutiflorum* Hausskn.:** B8-Bitlis: Bitlis, East of Mount Kambos, 18.06.2014, 38° 19' 29.58" K, 42° 00' 33.33" D, 1400-1600 m, M. Karataş 2131, Det.: M. Kurşat. ***E. montanum* L.:** A4-Çankırı: Çankırı- Artacalar, Dumanlı Mountain, 1350 m, 05.07.1991 A. Duran 1236 (GAZI) ***E. confusum* Hausskn.:** B8-Bitlis: Bitlis, East of Mount Kambos, 18.06.2014, 38° 19' 29.58" K, 42° 00' 33.33" D, 1400-1600 m, M. Karataş 2088, Det.: M. Kurşat. ***E. ponticum* Hausskn.:** B8-Bitlis: Bitlis, Mount Kambos south, 15.03.2014, 38° 17' 52.83" K, 41° 59' 15.31" D, 1240- 1650m, M. Karataş 1553, Det.: M. Kurşat. ***E. gemmascens* C.A.Mey.:** B8-Bitlis: Bitlis, Kambos Mountain north slope 08.07.2013, 38° 19' 23.26" K, 41° 59' 42.29" D, 1800-1950m, M. Karataş 1188, Det.: M. Kurşat. ***E. anagallidifolium* Lam.:** B8-Bitlis: Bitlis, Kambos Mountain north slope 03.07.2013, 38° 19' 23.26" K, 41° 59' 42.29" D, 1800-1950m, M. Karataş 1060, Det.: M. Kurşat. ***E. palustre* L.:** A8 Rize: Rize İkizdere, Başköy, 24.07.1984 A. Güner 6052 (GAZI). ***E. anatolicum* Hausskn. subsp. anatolicum.:** C6 Maraş: Maraş-Berit mountain, Karagöl, Yataz slope 2600 m, 25.07.1992 Z. Aytac, 5531 (GAZI). ***E. anatolicum* subsp. prionophyllum (Hausskn.) P.H.Raven:** A8 Rize: Rize İkizdere, Başköy, 18.06.1986, A.Güner 6969 (GAZI).

For light microscopy (LM) analysis, The pollen grains were prepared for light (LM) and scanning microscopy (SEM) by the standard methods described by Wodehouse (1935). For light microscopy, the pollen grains were mounted in Safranin glycerin jelly and observations were made with a Olympus BX-31 microscope under (E40, 0.65) and oil immersion (E100, 1.25), using 10x eye piece. Measurements were performed on at least 30 pollen grains per specimen for each morphological character (Polar axis (P), equatorial diameter (E), Plg (Porus length), Plt (porus width), mesopodium, apopodium, annulus length, annulus diameter, costae, exine and intine with LM using an oil immersion 100U objective lens.

For SEM studies, pollen grains were dried, mounted on stubs, coated with gold by sputter coater, and the SEM examination was carried using a ZEISS Supra 55 Scanning Electron Microscope at the SEM Laboratory of the Central Research Laboratory (MERLAB), Yuzuncu Yil University, Van. In general, the terminology used is in accordance with Punt et al. (2007) and Hesse et al. (2009).

3. Results

The palynological properties of the examined *Epilobium* taxa are summarized in Table 1. Representative pollen grains are illustrated in Figures 1–3.

3.1. Size, symmetry, and shape

The pollen grains of the investigated species are dispersed as tetrad. They can be described as bilateral symmetrical and subisopolar based on SEM and LM observations. The shape of the pollen grains in equatorial view are suboblate, and oblate-spheroidal, whilst their shape in polar view is triangular-obtus. The pollen grains of the genus are oblate-spheroidal, suboblate (*E. anatolicum* subsp. *anatolicum*, *E. palustre*, and *E. confusum*). The polar axis varies from 57.52-87.33 µm and the equatorial diameters from 65.42-95.23 µm. Amb diameter 62.50-92.74 µm. Mesopodium (M) 36.78-62.08 µm. Apopodium (Ap) 37.15-60.07 µm. Their dimensions are smaller in *E. palustre* and larger in *E. hirsutum* (Table 1; Figures 1-3).

3.2. Apertures

In the investigated taxa, there are eleven taxa with trizonoporate (rarely 2,4 porate), apertures at corners (angulaaperturate) (Table 1). The porus is long (10.81-22.03 µm) and broad (11.97-22.66 µm); The shape of porus is circular. The apertural membrane is generally psilate and rarely granulate. Annulus thickness (An-th) 4.25-6.35 µm. Annulus height (An-h) 14.29-23.58 µm (Table 1; Figures 1-3).

3.3. Exine, intine and Ornamentations

The exine ranges from 1.78 to 2.68 µm. Ectexine is thicker than endexine without costae and the intine is 0.39-0.69 µm thick. The exine shows tumescence at the aperture. Costae thickness

(C) 2.45-3.35 μm . Exine sculpturing, showed three distinct types of surface structures: Baculate (the common type), baculate-rugulate (*E. anatolicum* subsp. *prionophyllum*), and rugulate (*E. montanum*) (Table 1; Figures 1-3).

Table 1. Summary of pollen morphological data for the *Epilobium* species examined.

Taxa	P	E	P/E	Plg	Plt	Ex	In
<i>E. hirsutum</i>	87.33±11.09	95.23±10.54	Oblate-spheroidal	22.03±2.99	22.66±2.67	2.68±0.36	0.66±0.18
<i>E. parviflorum</i>	72.03±5.95	79.83±6.43	Oblate-spheroidal	18.10±2.96	17.57±2.85	2.47±0.40	0.45±0.17
<i>E. montanum</i>	82.52±3.09	94.30±3.13	Oblate-spheroidal	19.42±1.76	19.58±1.95	1.78±0.18	0.56±0.11
<i>E. anatolicum</i> subsp. <i>anatolicum</i>	59.87±3.41	67.45±2.46	Suboblate	16.01±1.55	15.97±1.20	2.29±0.57	0.63±0.17
<i>E. anatolicum</i> subsp. <i>prionophyllum</i>	73.73±4.23	80.80±3.76	Oblate-spheroidal	20.51±1.94	22.23±2.64	1.84±0.32	0.50±0.14
<i>E. palustre</i>	57.52±3.48	65.42±4.83	Suboblate	10.81±1.33	11.97±1.25	2.14±0.43	0.57±0.12
<i>E. minutiflorum</i>	63.17±7.85	68.00±7.98	Oblate-spheroidal	14.01±3.07	14.40±2.50	2.34±0.25	0.39±0.13
<i>E. confusum</i>	68.17±4.50	76.67±4.31	Suboblate	16.30±1.99	17.40±2.03	2.10±0.22	0.41±0.18
<i>E. ponticum</i>	71.23±4.69	76.03±4.84	Oblate-spheroidal	19.66±1.72	20.33±1.49	2.35±0.19	0.69±0.16
<i>E. gemmascens</i>	79.86±7.84	87.96±7.50	Oblate-spheroidal	14.87±2.36	16.77±2.35	2.21±0.24	0.51±0.15
<i>E. anagallidifolium</i>	67.20±2.34	74.50±2.69	Oblate-spheroidal	14.60±1.10	14.43±1.25	2.30±0.33	0.54±0.09

Taxa	An-th	An. h.	Amb	M	Ap	C	Orn.
<i>E. hirsutum</i>	4.61±0.90	21.49±2.01	90.09±6.54	61.86±3.73	59.40±1.42	2.49±0.48	Baculate
<i>E. parviflorum</i>	4.98±0.71	18.93±1.34	83.92±5.83	46.41±2.38	48.10±0.92	3.25±0.26	Baculate
<i>E. montanum</i>	6.13±0.52	20.39±2.01	92.74±4.12	62.08±3.24	60.07±1.27	3.35±0.46	Rugulate
<i>E. anatolicum</i> subsp. <i>anatolicum</i>	5.54±0.72	16.56±1.26	65.75±2.75	36.78±2.09	37.15±0.90	3.11±0.52	Baculate
<i>E. anatolicum</i> subsp. <i>prionophyllum</i>	6.35±1.01	18.29±1.73	84.50±5.57	46.52±1.98	48.42±2.43	2.87±0.45	Baculate-rugulate
<i>E. palustre</i>	5.84±0.70	14.29±1.20	62.50±5.30	37.14±0.78	39.02±0.94	2.65±0.46	Baculate
<i>E. minutiflorum</i>	5.27±1.39	15.48±2.48	70.36±5.30	43.07±1.18	44.82±2.34	2.79±0.58	Baculate
<i>E. confusum</i>	4.98±0.82	17.69±1.13	78.19±3.77	40.24±0.62	41.43±3.08	2.55±0.20	Baculate
<i>E. ponticum</i>	4.25±1.04	20.28±0.98	77.42±4.17	50.72±1.08	48.43±2.66	2.45±0.31	Baculate
<i>E. gemmascens</i>	6.01±0.74	23.58±1.01	89.24±3.29	55.08±2.03	56.73±1.99	2.72±0.54	Baculate-rugulate
<i>E. anagallidifolium</i>	4.50±0.62	20.25±1.40	72.02±2.94	50.72±1.08	53.01±1.08	2.75±0.63	Baculate

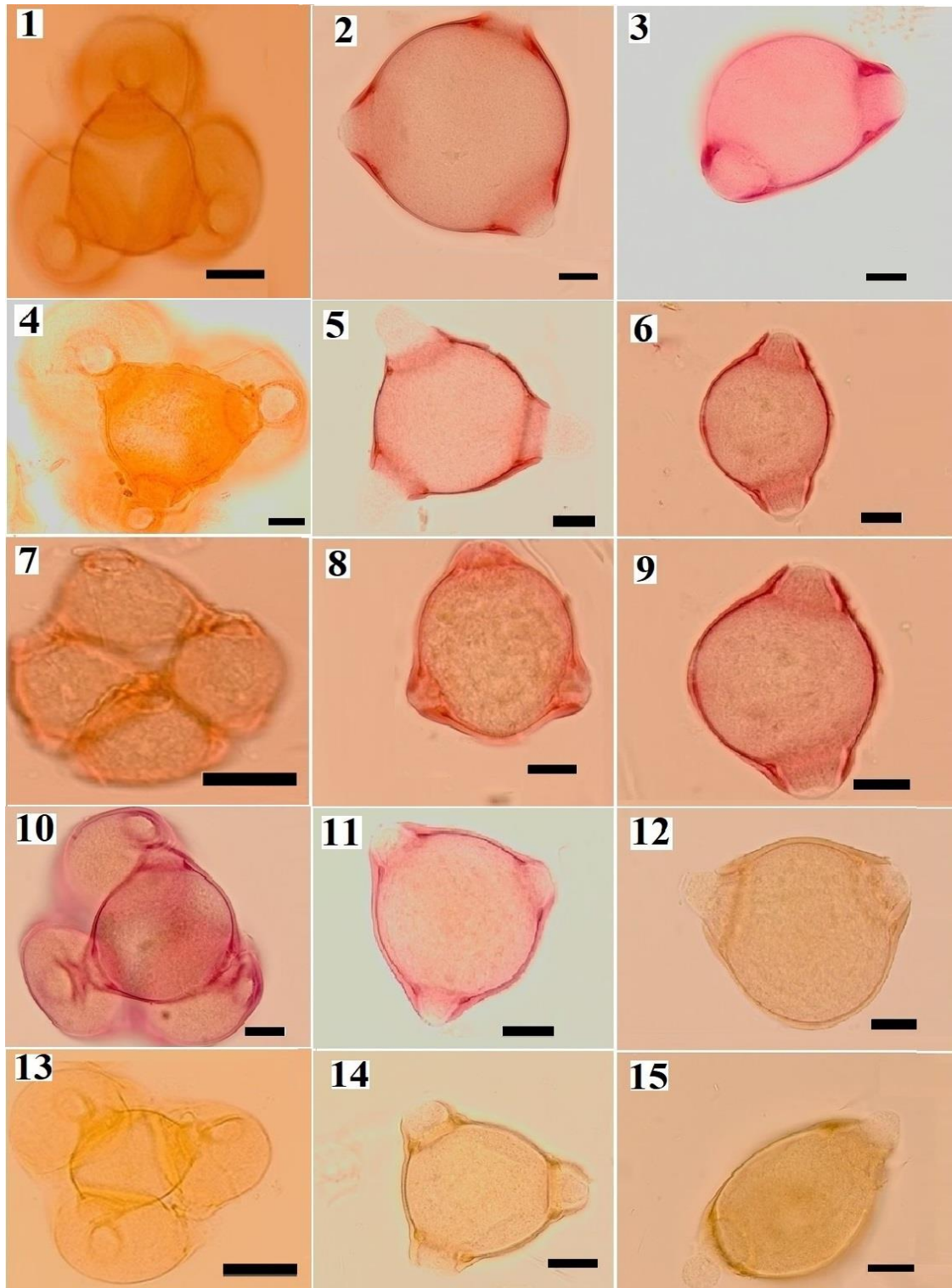


Figure 1. Pollen grains LM photos of studied taxa: tetrad, polar and equatorial view respectively; **(1-3)** *Epilobium hirsutum*, **(4-6)** *E. parviflorum*, **(7-9)** *E. montanum*, **(10-12)** *E. anaticum* subsp. *anaticum*, **(13-15)** *E. anaticum* subsp. *prionophyllum* (Scale bar 20 μm) and **(1,7,13)** Scale bar 50 μm).

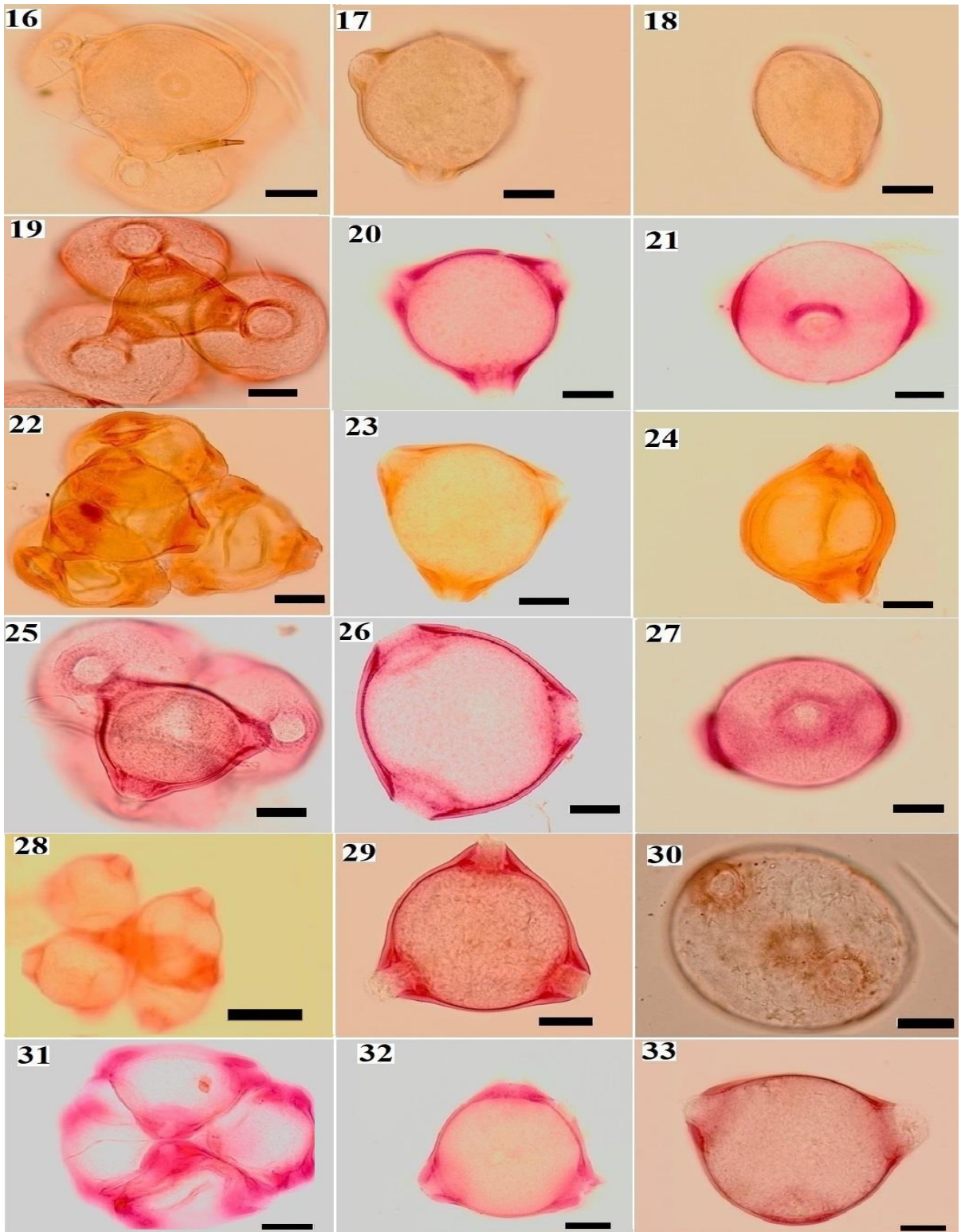


Figure 1. (Continued) (19-21) *E. minutiflorum*, (22-24) *E. confusum*, (25-27) *E. ponticum*, (28-30) *E. gemmascens*, (31-33) *E. anagallidifolium* (Scale bar 20 µm) and (28; Scale bar 50 µm).

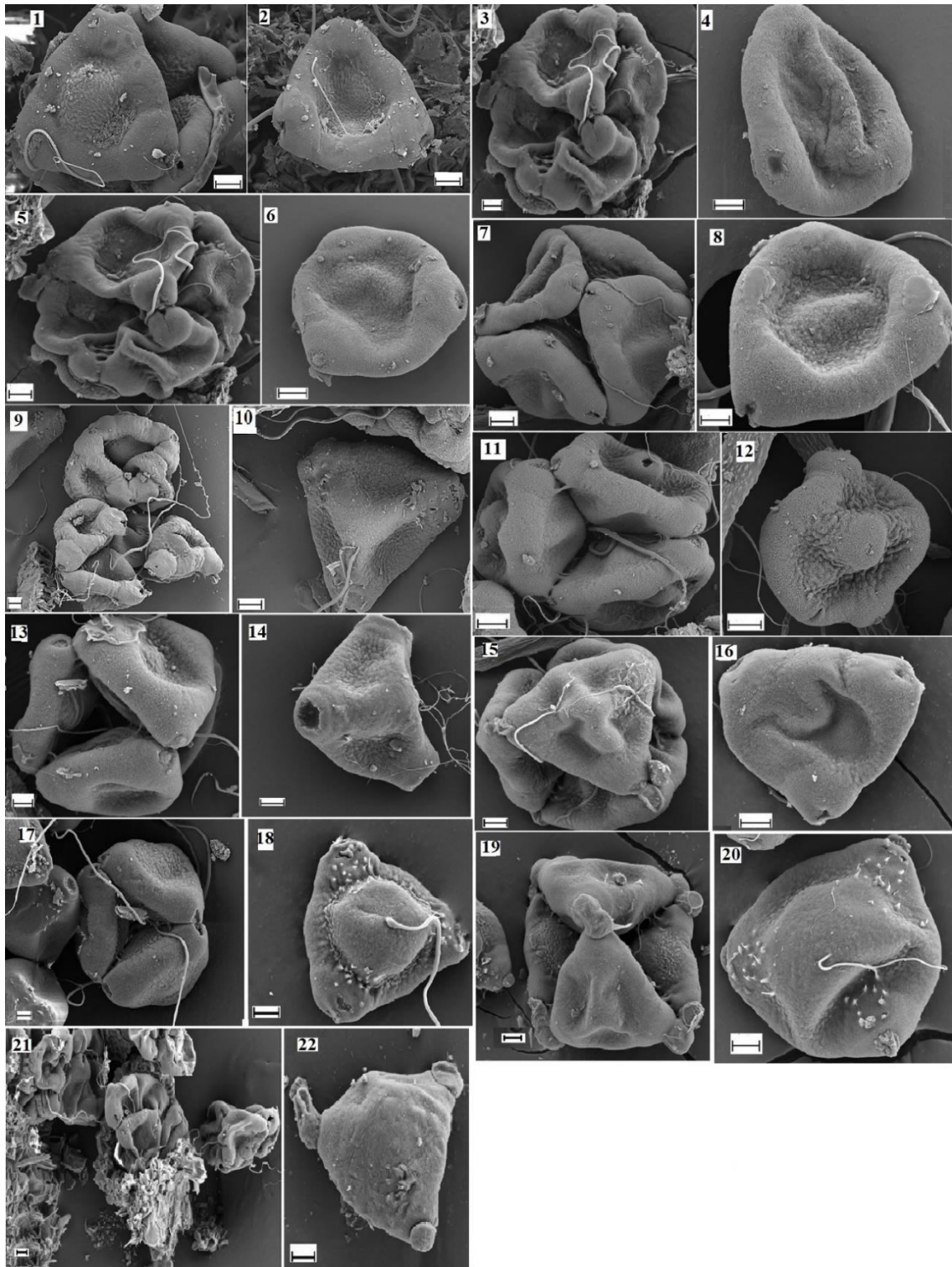


Figure 2. Pollen grains SEM photos of studied taxa: tetrad and general view respectively; (1-2) *Epilobium hirsutum*, (3-4) *E. parviflorum*, (5-6) *E. montanum*, (7-8) *E. anaticum* subsp. *anaticum*, (9-10) *E. anaticum* subsp. *prionophyllum*, (11-12) *E. palustre*, (13-14) *E. minutiflorum*, (15-16) *E. confusum*, (17-18) *E. ponticum*, (19-20) *E. gemmascens*, (21-22) *E. anagallidifolium* (Scale bar 5 μm).

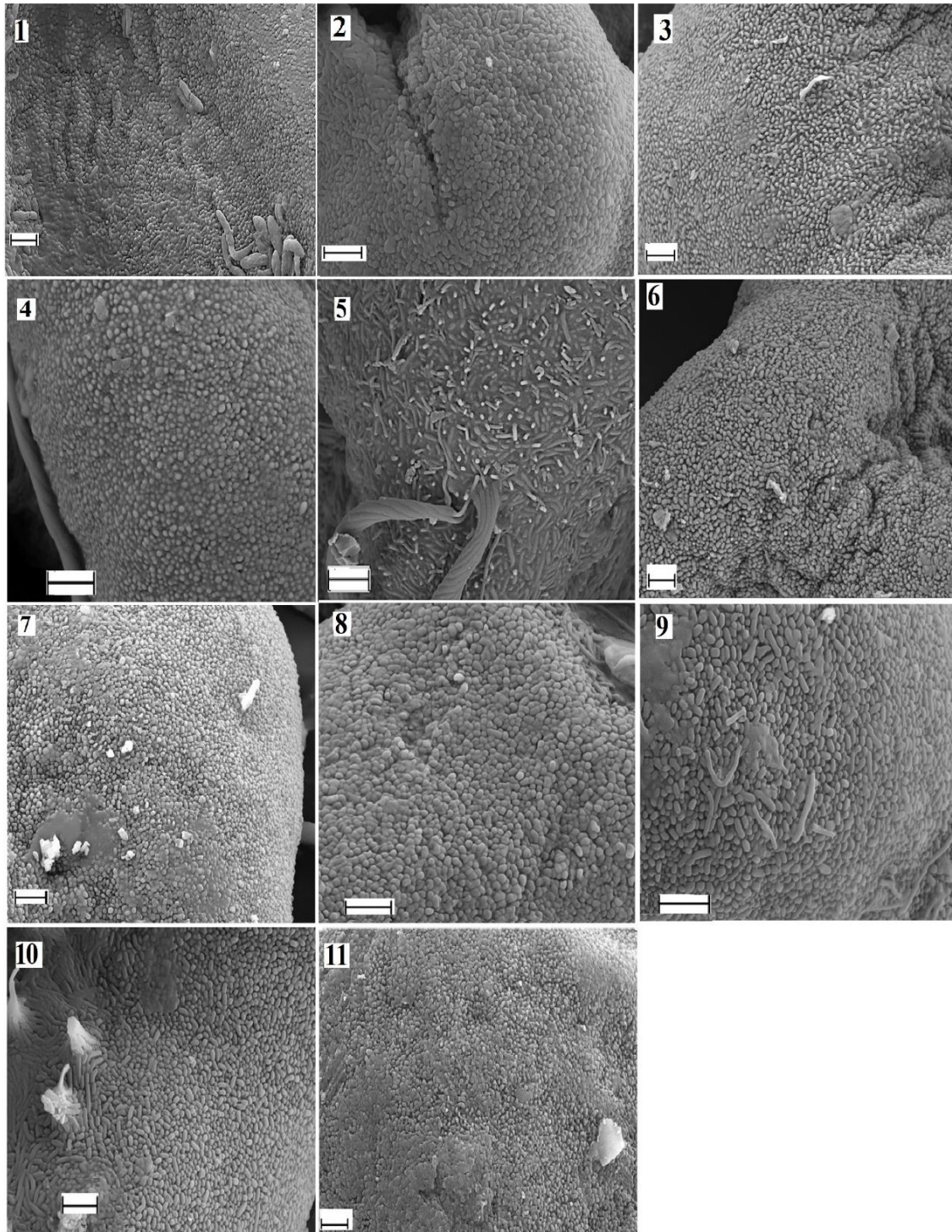


Figure 3. Pollen grains SEM photos of studied taxa: ornamentation; (1) *Epilobium hirsutum*, (2) *E. parviflorum*, (3) *E. montanum*, (4) *E. anaticum* subsp. *anaticum*, (5) *E. anaticum* subsp. *prionophyllum*, (6) *E. palustre*, (7) *E. minutiflorum*, (8) *E. confusum*, (9) *E. ponticum*, (10) *E. gemmascens*, (11) *E. anagallidifolium* (Scale bar 2 μm).

4. Discussion

Pollen grains characteristics of *Epilobium* 11 taxa are summarised in Table 1 and are shown in Figs. 1-3. Pollen grains are tetrad, apertures (angulaperturate) at corners and pollen grains are triangular-obtus, 3-zonoporate (*E. anatolicum* subsp. *anatolicum* 4 % 2-porate, *E. anatolicum* subsp. *prionophyllum* taxa, 3 % 2-porate and 6 % 4-porate and *E. palustre* 6 % 4-porate). *E. montanum*, *E. anatolicum* subsp. *anatolicum*, *E. palustre*, *E. confusum* taxa have suboblate and other taxa have oblate-spheroidal pollen grains shape. *E. palustre* (57.52 μm and 65.42 μm) with the smallest polar axis and equatorial axis has the largest polar axis *E. hirsutum* (87.33 μm and 95.23 μm). The taxon with the smallest pore length and pore width is *E. palustre* (10.81 μm and 11.97 μm). The largest polar axis is *E. hirsutum* (22.03 μm and 22.66 μm). The smallest exine thickness is in *E. montanum* (1.78 μm) and the largest one is in *E. hirsutum* (2.68 μm). The smallest intin thickness is observed in the taxon *E. minutiflorum* (0.39 μm), while the largest thickness is observed in the taxon *E. ponticum* (0.69 μm). *E. ponticum* (4.25 μm) has the smallest annulus thickness, and *E. anatolicum* subsp. *prionophyllum* (6.35 μm) has the greatest thickness. *E. palustre* (14.29 μm) has the shortest annulus height and *E. anatolicum* subsp. *prionophyllum* (23.58 μm) has the largest taxon. The smallest ambi diameter is in *E. palustre* (62.50 μm), and the largest in *E. montanum* (92.74 μm). The shortest mesopodium is in *E. anatolicum* subsp. stated that pollen grains color can also be used for species differentiation from the genus *Clarkia* Pursh in Onagraceae. Skvarla et al. (2008) reported that pollens with tetrahedral tetrad characteristics in Onagraceae are connected to each other by bridges and that the structures called viscin threads formed in tetrahedral pollens. This is also characteristic for *Epilobium* taxa which are the structures that connect the pollen. It was also noted that the palynomorphological characters have taxonomic importance and the importance of more detailed studies in order to obtain more effective results was emphasized in the study.

Punt et al. (2003) determined 7 different pollen types according to micromorphological features such as pollen grain size, aperture type and exine thickness in the Northwest European *Epilobium*. In this genus, three different types of pollen: *Epilobium angustifolium*-type, *E. latifolium*-type and *E. tetragonum*-type were included. The structure of pollen is radial symmetrical, monad and tetrad. Tectum characteristic is pitted-angular, fine granular, rod-like, oblate, suboblate and spheroidal pollen. Their shapes revealed that they have granulate and striate-rugulate ornamentation.

Makbul et al. (2008) revealed that *Epilobium palustre*, *E. algidum* Bieb., *E. ponticum*, *E. confusum*, *E. hirsutum*, *E. montanum* pollen grains are radially symmetrical, isopolar, 3-zonoporate and generally shed in monads, rarely tetrads. Pollen grains shape are suboblate, *E. montanum* (spheroidal). taxa of *Epilobium* are usually tetrahedral tetrads and rarely monads. In the examination carried out on a certain number of

anatolicum (37.15 μm), and the largest one is in *E. montanum* (62.08 μm). Apopodium is seen in the shortest taxon *E. anatolicum* subsp. *anatolicum* (37.15 μm), and the largest in *E. montanum* (60.07 μm). The taxon with the smallest costal thickness is *E. ponticum* (2.45 μm), and the largest one is *E. montanum* (3.35 μm). It was determined that the taxon *E. montanum* has rugulate, *E. anatolicum* subsp. *prionophyllum* and *E. gemmascens* baculate-rugulate, while the other taxa have baculate ornamentation.

Some studies on the palynomorphological features of *Epilobium* genera have been carried out (Chen and Wang, 2001; Punt et al., 2003; Skvarla et al., 2008; Perveen and Qaiser, 2013). The most comprehensive palynological studies on *Epilobium* taxa in our country were made by Makbul et al. (2008); Okur (2019). Makbul et al. (2008) revealed the morphological features of the pollen of *Epilobium* 6 taxon and stated that all species of our country should be studied in order to make more contribution. (Patel et al., 1984; Perveen and Qaiser, 2013; Okur, 2019) determined that the pollen distribution of *Epilobium* is generally tetrahedral tetrad and rarely monad.

Lewis and Lewis (1955) reported that in addition to morphological features such as umb diameter, pore size, exine and ectexin thickness of pollen, the color of fresh pollen is effective in the differentiation of taxa, and Small et al., 1971

The outline is triangular in meridional optical section. Polar axis is 78–67 μm and equatorial axis is 87–94 μm . The aperture membrane is generally psilate and rarely granulate. The exine is tectate. Ornamentation is baculate, *E. ponticum* and *E. confusum* (striate). They stated that palynological characters such as pollen shape and surface ornamentation were effective in distinguishing *Epilobium* taxa.

Perveen and Qaiser (2013) found that the tectum structure of pollen grains belonging to the Onagraceae is an important characteristic. Rugulate-perforate ornamentation was observed in two *Oenothera* species (*O. affinis* Combess. and *O. glazioviana* Michel), which are known for their taxonomic affinity to the genus *Epilobium*, while *Epilobium leiophyllum* Haussn. It has been determined that it has a granulate ornamental structure, as well as *E. angustifolium*, *E. cylindricum* D. Don., *E. hirsutum*, *E. latifolium* L., *E. parviflorum* and *E. palustre* species with scabrate ornamentation.

Erdtman 1960; Punt et al. 2003 revealed that there is a fine connection between the tetrad and monad pollen grains spreads by breaking this connection in the acetolysis process. Skvarla et al. (2008) observed that the pollen of the genus *Epilobium* has both monad and tetrahedral tetrad structures. They revealed that the monad structure, the tetrahedral tetrad structure, was formed as a result of the breakdown of the bridges between pollens and each other during the preparation process. Makbul et al. (2008) observed that the pollens of the 6 taxa, it was determined that the pollen grains in the monad structure supported the stated idea.

As a result of their examination on the pollens of the genus *Epilobium*, Okur et al. (2019), stated that the pollen is monad or tetrahedral or, bilateral, with subisopolar symmetry, 3-porate (trizonoporate). Surface ornamentation is baculate, striate and baculate-rugulate. They determined that the pollen grains in the *Epilobium* section spread in tetrahedral form from the anther and monad in the *Chamaenerion* section. They determined that the pollen shape of the taxa belonging to *Epilobium*, exine ornamentation, and pollen grains leaving the anther, ie spreading (pollen out of the anther monate or tetrahedral) are important in the differentiation of pollen. Okur (2019) determined that *Epilobium* and *Chamaenerion* taxa have baculate, baculate-rugulate, rugulate, baculate-plate ornaments and pollen grains size is between 40.70-53.96 µm. They determined that it may be due to the fact that they have carried out palynomorphological studies on the taxon.

Our results and the data of Okur 2019 were found to be compliant regarding the fact that the taxa are tetrahedral tetrads and ornamentations with trizonoporate (*E. anatolicum* subsp. *anatolicum* 4% 2-porate, *E. anatolicum* subsp. *prionophyllum* taxa, 3% 2-porate and 6% 4-porate and *E. palustre* 6% 4-porate) pollens were observed. On the other hand, using different methods may have caused differences in the polar and equatorial axis, pore length and width, exine and intin thickness, annulus thickness, Amb diameter, mesopodium and apopodium thicknesses.

Epilobium is considered to be a taxonomically difficult genus due to the fact that it contains a large number of taxa with morphological similarities and the high percentage of hybridization within the genus (Krajsek et al., 2006). For this reason, it is emphasized that making a distinction only on morphological characters is not a solution in the differentiation of taxa belonging to the genus and there is a need for various studies that will contribute to this distinction.

In our opinion, revealing the morphological features of the pollen of 11 taxa belonging to *Epilobium* will contribute primarily to plant systematics and other fields of palynology.

Acknowledgements

We wish to thank Curators of Herbaria GAZI and Bitlis Eren University Herbaria, who allowed us to study their *Epilobium* specimens, to Dr. Yüksel AKINAY and Dr. Ihsan Nuri AKKUŞ (Science Application and Research Center, University of Yuzuncu Yil, Van) who is helper to take of electron photographs of pollen grains surface.

References

- Brown, D.D., 1967. Chapter 2. The Genes for Ribosomal RNA and their Transcription During Amphibian Development, *Current Topics in Developmental Biology*, 2: 47-73.
- Chen, S.H., Wang, Y.F., 2001. Pollen Flora of Yuenyang Lake Nature Preserve, Taiwan (II), *Taiwania*, 46 (2): 167-191.
- Erdtman, G., 1952. Pollen Morphology and Plant Taxonomy, *Almqvist and Wiksells*, 133-134.
- Erdtman, G., 1960. The acetolysis method. A revised description. *Svensk Botanisk Tidskrift*, 54: 561-564.
- Graham, A., Barker, G. & Da Silva, M.F., 1980. Unique pollen types in the Caesalpinioideae (Leguminosae). *Grana*, 19: 79-84.
- Hesse, M., Halbritter, H., Zetter, R., Weber, M., Buchner, R., Frosch Radivo, A., & Ulrich, S., 2009. Pollen terminology an illustrated handbook. -Spri. Verlag. Vienna.
- Heywood, V.H., Brummitt, R.K., Culham, A. and Seberg, O., 2007. *Flowering Plant Families of the World*. Royal Botanic Gardens, Kew. 1- 424.
- Keri, C. & Zetter, R., 1992. Notes on the exine ultrastructure of Onagraceae and Rhododendroideae (Ericaceae). -Grana, 31: 119-123.
- Krajsek, S.S., Dermastia, M. and Jogan, N., 2006. Determination key for Central European *Epilobium* species based on trichome morphology. *Botanica Helvetica*, 116: 169-178.
- Lewis, H. and Lewis, M.E., 1955. The genus *Clarkia*. *University of California Publications in Botany*, 20: 241-392.
- Makbul, S., Türkmen, Z., Coskuncelebi, K. & Beyazoglu, O., 2008. Anatomical and pollen characters in the genus *Epilobium* L. (Onagraceae) from Northeast Anatolia. *Acta. Biol. Cracov. Bot.* 50: 51-62.
- Mitroiu, N., 1963. Certetari palinologice asupra microsporilor din familia Onagraceae. *Acta Botanica Horti Bucuresti*. 1: 435-457.
- Mosquin, T., 1966. A new taxonomy for *Epilobium angustifolium* L. *Brittonia* 18: 167-188.
- Okur, S., 2019. Türkiye *Epilobium* L. (Onagraceae) Taksonlarının Biyosistematik Yönden İncelenmesi. *Recep Tayyip Erdoğan Üniversitesi, Fen Bilimleri Enstitüsü. Doktora Tezi*. 1-262.
- Punt, W., Rovers, J. and Hoen, P.P., 2003. The Northwest European Pollen Flora, Onagraceae, 67. *Review of Palaeobotany and Palynology*, 123: 107-161.
- Pragłowski, J., Nowicke, J.W., Skvarla, J.J., Hoch, P.C., Raven, P.H. & Takahashi, M., 1994. Onagraceae Juss.: Circaeae DC., Hauyae Raimann, Epilobieae Spach. *World Pollen and Spore Flora* 19: 1-38.
- Patel, V.C., Skvarla, J.J. and Raven, P.H., 1984. Pollen characters in relation to the delimitation of Myrtales. *Annals of the Missouri Botanical Garden*, 71: 858-96.
- Perveen, A. and Qaiser, M., 2013. Pollen Flora of Pakistan-LXXI. Onagraceae. *Pakistan Journal of Botany*, 45(1): 241-245.
- Punt, W., Hoen, P.P., Blackmore, S., Nilsson, S. and Le Thomas, A., 2007. Glossary of pollen and spore terminology. *Review of Palaeobotany and Palynology*, 143, 1-81.
- Rahimi, S., Mehrabian, A.R., Sheidai, M. and Sadr, M.M., 2018. Pollen morphology of Onagraceae in Iran. *Iranian Journal of Botany*, 24 (1): 16-27.
- Raven, P.H., 1962a. The genus *Epilobium* in Turkey. *Notes from the Royal Botanic Garden Edinburgh*, 24: 183-203.

- Rowley, J. & Claugher, D., 1996. Structure of the exine of *Epilobium angustifolium* (Onagraceae). Grana. 35: 79-86.
- Rowley, J.R., & Skvarla, J.J., 2006. Pollen development in *Epilobium* (Onagraceae): Late microspore stages (a review). -Rev. Palaeobot. Palynol. 140: 91–112.
- Skvarla, J.J., Chissoe, W.F. and Sharp, M., 1978. An ultrastructural study of viscin threads in Onagraceae pollen. Pollen et Spores, 20: 5–143.
- Skvarla, J.J., Rowley, J.R., Hoch, P.C. and Chissoe, W.F., 2008. Unique tetrads of *Epilobium luteum* (Onagraceae: Onagraceae) pollen from Alaska. Brittonia, 60: 398-404.
- Small, E., Bassett I.J., Crompton, C.W. and Lewis, H., 1971. Pollen phylogeny in *Clarkia* Taxon, 20: 739-746.
- Ting, W.S., 1966. Pollen morphology of Onagraceae. Pollen et Spores, 8: 9-36.
- Wagner, W.L., Hoch, P.C., Raven, P.H., 2007. Revised Classification of the Onagraceae. Syst. Bot. Monogr., 83: 1-239.
- Walter, B., Ulf, S., Michael, R., 2007. Interspecific hybridization between alien and native plant species in Germany and its consequences for native biodiversity. Biol. Conserv. 137: 248-253.
- Wodehouse, R.P., 1935. Pollen Grains: Their Structure, Identification and Significance in Science and Medicine. Hafner Publish, Company, New York & London, pp. 106-109.



Habitat Classification of Cilo Glaciers and Their Surroundings

İbrahim DEMİR^{a,*} , Murat ÜNAL^b 

^a Bitlis Eren University, Faculty of Arts and Sciences, Department of Biology, 1300, Bitlis, Turkey

^b Van Yüzüncü Yıl University, Faculty of Education, Department of Biology Education, Zeve Campus, Tuşba-Van, Turkey

ARTICLE INFO

Article history:

Received 12 October 2021

Received in revised form 01 November 2021

Accepted 08 November 2021

Keywords:

EUNIS

Cilo Glaciers

Hakkari

Habitat mapping

ABSTRACT

This study was carried out for the habitat classification of the Cilo glaciers and their environments, which have significant biological diversity within the borders of Hakkari National Park and are under serious threat especially due to global climate change in Turkey. The study material consists of the data obtained as a result of field studies conducted in 2018-2019. As a result of the studies, 11 habitat types were determined on the area according to habitat types of The European Nature Information System (EUNIS) and observations about these habitats were given. In addition, 4 types of vegetation are determined according to the plant density with satellite images of the area. This research reveals the importance of habitat type determination studies for important nature areas.

© 2020. Turkish Journal Park Academic. All rights reserved.

1. Introduction

The human population is expected to reach 9 billion by 2050. In this case, it is predicted that 10-20% of natural areas will be replaced by agriculture and urban infrastructure, further reducing the habitat of wildlife. (Martinuzzi et al., 2015). Anthropogenic pressures affect the structure of local ecological communities and may lead to local extinction of species. This could lead to reduced ecosystem functionality (Tilman et al., 2001; Cardinale et al., 2006) and global extinction (Vié et al., 2009). increased human population and consumption will likely result in further habitat loss (Newbold et al., 2014; Krausmann et al., 2013). On the other hand, the pressure of global climate change on sensitive habitats is a major threat to sensitive species living in these areas (Kromp-Kolb and Formayer, 2005; Dow and Downing, 2006). Natural areas are particularly vulnerable to climate change due to their limited adaptive capacity, and some of these systems may suffer significant and irreversible damage. (Omann et al., 2009).

Due to increasing environmental problems, the loss of Biodiversity is expected to continue to increase in the coming years. The most effective way to prevent or reduce the loss of

biodiversity is to preserve the habitat. Therefore, identifying and identifying habitats with unique characteristics is extremely important (Geven 2016; Schamberger and Krohn 1982; Schroeder, 1986; Çakmak and Aytaç, 2020; Süel et al., 2018).

Conservation of natural areas requires comprehensive classification systems of natural habitat types. They are essential for creating protected area networks, conducting natural area surveys, setting monitoring targets, management planning, environmental impact assessments and ecological restoration (Chytrý et al., 2020; McDermid, Chytrý et al., 2015). Conservation programs can tackle the main cause of extinction by reducing the loss of natural habitats and the species they host (Eken et al., 2014; Bruner et al., 2001).

Despite the fact that the number of EUNIS studies in Turkey has increased in recent years, it is small when compared to Europe. Priority might be given to locations with potentially significant biological and habitat diversity, such as national parks, nature reserves, and special environmental protection zones, in the following process of identifying the areas to be investigated on habitat categorization. Because these areas differ from their immediate surroundings in terms of ecology, climate, and

* Corresponding author. Tel.: +0 434 222 0020; fax: +0 434 222 9143

E-mail address: idemir@beu.edu.tr

ORCID : 0000-0003-1533-556X (İ. Demir), 0000-0002-6224-8269 (M. Ünal)

topography. In this situation, it will affect the floristic composition and hence the habitat type, allowing new habitat types to be identified in these regions (Çakmak, 2017; Çakmak and Aytac, 2021).

The Cilo Mountains and Sat Glacier Lakes, located inside the boundaries of Hakkari province in Turkey's Eastern Anatolian region, are one of the sites with priority protection. The area, which was recently declared a National Park, is also among the Important Natural Areas that host many species with its unique endemics. This area is the habitat of *Cephalaria hakkarica*, *Cirsium hakkariacum* and many other locally endemic plant and other species (Eken et al., 2006). However, human and climate change pressures on the area have taken their toll in recent years. Determining the habitat types of this area, which is very important in terms of biodiversity, is extremely important for the management and sustainability of the area. The EUNIS habitat classification (European Union Nature Information System), developed by the European Environment Agency, has been used in nature conservation as a tool to identify habitat units during monitoring and assessments. (Černecký et al., 2020; Moss, 2008).

Habitat maps for sensitive areas can help achieve national biodiversity conservation goals and assess conservation status (Bilasi et al., 2000).

The aim of this research is to determine habitat types according to EUNIS habitat classification for the protection of endangered species with increasing anthropogenic pressures and global climate change threat in recent years. Thus, to ensure the formation of data for the protection of the rich biodiversity in this area and to form the basis for management plans.

2. Material and Methods

2.1. Study area

The area is 87.6% covered with mountainous areas and there are many mountains and peaks above 3000 m altitude. Uludoruk (Reşko) Hill (4135 m) on the Cilo Mountains is also the second highest point in Turkey after Mount Ağrı. Cilo Glacier Mountain is located in the eastern part of the Southeast Taurus Mountain (Fig. 1). It's also known as the most glaciated region of Turkey (Yavaşlı and Ölgün, 2008).

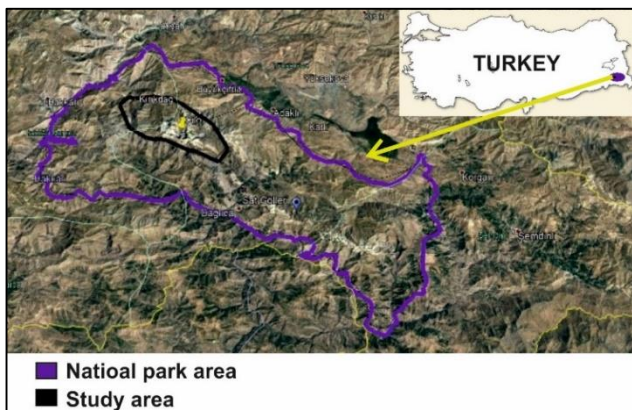


Figure 1. Location map of the study area

2.2. Field work

Flora studies were carried out in the research area in 2018-2019. The samples obtained as a result of these studies were recorded and identified. In addition, habitat types in the area and plant species on these habitats were determined.

2.3. Maps Usage

2.3.1 Vegetation map

First of all, the Normalized Difference Vegetation Index (NDVI) method, which is frequently preferred in mapping the distribution areas of plants, was used to create the vegetation map of the study area (Rouse et al., 1974). SENTINEL 2A satellite images with a spatial resolution of 10 m were used to create the vegetation map. Images were obtained by downloading cloudless images (25.06.2020) from "https://codata.eumetsat.int/#/home". In the study, Band 8 (NIR) and Band 4 (Red) were used in the images consisting of 13 bands. Vegetation maps were created using the SNAP program with the formula given below.

$$NDVI = \frac{Band\ 8 - Band\ 4}{Band\ 8 + Band\ 4}$$

In the vegetation map obtained; areas devoid of vegetation, covered with weak vegetation, medium and dense vegetation were determined (Fig. 2).

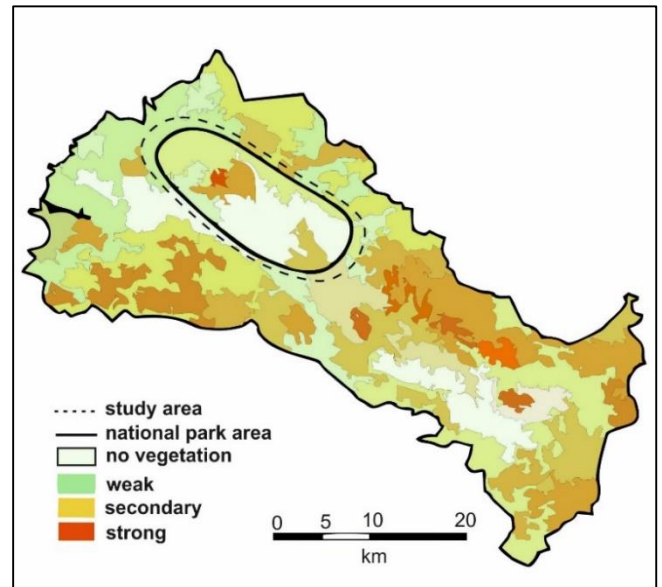


Figure 2. Vegetation map of Study area

2.3.2. Habitat types map

According to the EUNIS Habitat types (https://eunis.eea.europa.eu/habitats-code-browser.jsp?expand=#level_G), the findings obtained as a result of the field studies were mapped. First of all, the polygon map of the area was drawn and habitats were placed on these polygons. These habitats were created according to the following codes of EUNIS and each colored with a different color (Fig. 5)

- C: Inland surface waters
 D: Mires, bogs and fens
 E: Grasslands and lands dominated by forbs, mosses or lichens
 H: Inland unvegetated or sparsely vegetated habitats

3. Results and discussion

11 habitat types have been identified in the area according to the coding of EUNIS. These; C (C1.7, C2.2), D (D4.2), E (E1.2E), H (H2.2; H3.61; H3.62; H4.1; H4.23; H5.22; H5.36), These habitats consist of steppe, high mountain meadow formations, areas that are weak in terms of vegetation and completely devoid of vegetation. Habitat maps are used as a basis for management plans and to define preservation objectives at the regional and national levels by ecologists, environmentalists, administrators, and nature conservationists (Mergen and Karacaoğlu 2015; Moss, 2008). The habitats identified on the area are as follows.

C1.7: Permanent lake ice

Covers a small area east of the Cennet Cehennem valley. There are no plants in this habitat type (Fig3).



Figure 3. Cilo glacial lake

Permanent or almost permanent lake ice formations that produce continuous ice sheets that cover the whole surface all year or recede to a section of the lake during the summer, and are accompanied or replaced by floating ice blocks, rafts, and hummocks. On a local, seasonal, or permanent basis, they can extend to the lake's whole depth. They can be found at high latitudes and high altitudes (https://eunis.eea.europa.eu/habitats-code-browser.jsp?expand=#level_G).

C2.2: Permanent non-tidal, fast, turbulent watercourses

They are the streams starting from the glacial lake and continuing along the Cennet Cehennem valley. It is called Dêz Stream by the local people and it was named that way in the Flora of Turkey (Davis, 1965-1985). The source of these streams is Cilo

glaciers and snow patches. The flow rate and amount of the creeks fed by small rivers increase as you go down. The power plant established near Kırıkdağ village was built on this stream.

D4.2: Basic mountain flushes and streamsides, with a rich arctic-montane flora

These are areas where the ground water is high and the temperature is low, around the Cilo glacial lake and along the Dez stream. The dominant species in this area vary according to the vegetation period. But *Poa pratensis* L., *Ranunculus poluninii* P.H.Davis, *Primula auriculata* Lam., Tabl., *Colchicum kurdicum* (Bornm.) Stef., *Puschkinia scilloides* Adams are the most prominent species on the area. Apart from this, the habitat is the habitat of locally endemic plants such as *Myosotis platyphylla* Boiss, *Primula davisii* W.W.Sm.

E1.2E: Irano-Anatolian steppes

This habitat type covers most of the area. Cennet Cehennem Valley, which is especially rich in vegetation and biodiversity, is one of the important areas of this habitat type. Although the dominant species vary, the dominant species in this area are the Tragagantic steppes formed by the spiny *Astragalus* sp. species (Figure 4). Apart from this, it is represented by other hemicryptophyte and gametophyte form species in the area. Along with the spiny Camephyte *Astragalus* species, genus such as *Thymus*, *Verbascum*, *Eryngium*, *Helichyrsom*, *Cousinia*, *Ferula*, *Centaurea*, *Allium*, *Dianthus*, *Artemisia*, *Achillea*, *Salvia* are abundant. While the most dominant genus in the *Gramine* group are *Poa*, *Elymus*, *Bromus* species in the area, the most intense species is *Psathyrostachys fragilis*. Some of the important endemics in this habitat type in the area are *Astragalus latistipulatus* D.F. Chamb., *Astragalus sachanewii* Sirj., *Astragalus yueksekovae* V. Matthews, *Gypsophila adenophylla* Barkoudah, *Gypsophila baytopiorum* Kit Tan, *Gypsophila hakkarica* Kit Tan, *Cousinia satdagensis* Hub.-Mor., *Cousinia hakkarica* Hub.-Mor. and *Crocus kotschyanus* K.Koch



Figure 4. A view from the steppes in the area

H2.2: Cold limestone screes

This habitat type is the formations formed by the fragmentation

of the rocky slopes, especially around Kırıkdağ village and the eastern parts of the Cennet Cehennem Valley, over time. Soil accumulation is low in this habitat. Factors such as so little soil, water scarcity, rock mobility that flows downstream hindering vegetative growth, only host special species that can adapt to the environment. For these reasons, the vegetation is very weak. In these areas, there are species such as *Melica ciliate* L., *Capparis spinosa* L.

H3.61 - Bare weathered rock and outcrop habitats

Consists of bare rocky areas with less plant species than H3.62. Although very few plants are seen in these areas, it is the habitat of local endemics such as *Rosularia davisii* Muirhead, *Scrophularia pumilio* Lall

H3.62: Sparsely vegetated weathered rock and outcrop habitats

It consists of steep cliffs forming mountain peaks from Kırıkdağ Village towards the Cennet Cehennem valley. The highest point of the area is Reşko Hill (4135 m). This habitat type is one of the important habitats in terms of biodiversity, although the vegetation is weak. These rocks constitute the habitat of important locally endemic species such as *Silene araratica* subsp. *davisii* (Chowdhuri) Ghaz, *Silene cartilaginea* Hub.-Mor., *Silene lucida* Chowdhuri, *Rosularia davisii* Muirhead, *Draba thylacocarpa* (Nábelek) Hedge and *Theodorovia karakuschensis* (Grossh.) Kolak.

H4.1: Snow packs

The surroundings and northern slopes of the Cilo glacial lake are in this habitat type. This area is devoid of vegetation. There are some *bulbous species* (*Puschkinia scilloides* Adams, *Colchicum kurdicum* (Bornm.) Stef. etc) only at the bottom of the melting snowpacks.

H4.23: Glaciers

Although glaciers are devoid of vegetation, they play an important role in the biodiversity of the area. According to Yavaşlı and Ölgün (2008) there are 5 glacier areas on the area. These are: Erinç (Suppa Durak) Glacier, x Valley glaciers (Mia Hvara or Avaspi) and Uludoruk (Gelyaşın or İzbırak) glaciers. (Figure 2).

H5.22: Sparsely vegetated glacial moraines

It is one of the habitat types that occupy the least space in the area. Vegetation is very sparse

H5.36: Shallow rocky soils with very sparse or no vegetation

This habitat type is located in the lower part of the Cilo glaciers and margins of the Dez Stream. Soil is very low, so there is either a complete deficiency of vegetation or very sparse vegetation.

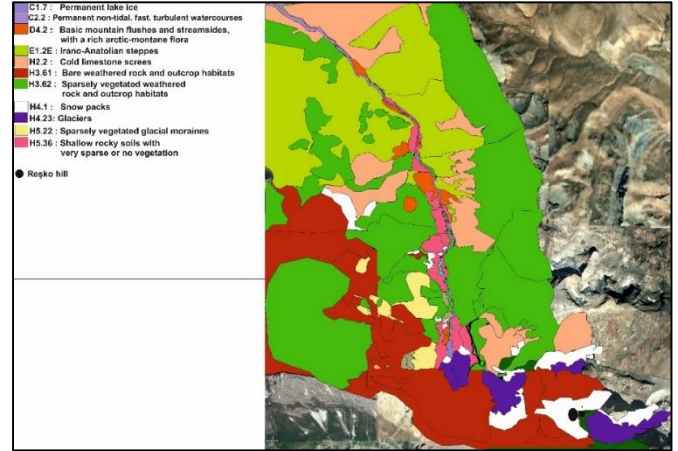


Figure 5. The EUNIS habitat map of the study area.

Acknowledgement

Some of the data presented in this study were obtained within the scope of Hakkari Province Biodiversity Inventory and Monitoring Project of Republic of Turkey Ministry of Agriculture and Forestry General Directorate of Nature Conservation and National Parks. In addition, satellite images of the vegetation map of the region were prepared by Dr. Mustafa Akkuş (Van Yüzüncü Yıl University). We would like to take this opportunity to thank the aforementioned institution and person.

References

- Abdulhasan, N. 2009. Habitat mapping project of the proposed Iraqi Marshlands National Park area. *BioRisk*, 3, 55.
- Blasi, C., Carranza, M.L., Frondoni, R., and Rosati, L. 2000. Ecosystem classification and mapping: A proposal for Italian Landscapes. *Applied Vegetation Science*, 3, 233-242. doi:10.2307/1479002
- Bruner, AG., Gullison, RE., Rice, RE., and da Fonseca, GAB. 2001. Effectiveness of parks in protecting tropical biodiversity. *Science* 291, 125-128.
- Çakmak, M. H., and Aytaç, Z. 2021. EUNIS Habitat Sınıflandırmasının Türkiye Durum Değerlendirmesi. *Bilge International Journal of Science and Technology Research*, 5(2), 111-117.
- Çakmak, M.H. 2017. Avrupa Doğa Bilgi Sistemi (EUNIS) Habitat Sınıflandırması ve Soğuksu Milli Parkı Pilot Alanında Uygulanması (Uzmanlık Tezi). T. C. Orman ve Su İşleri Bakanlığı, Ankara, Türkiye
- Çakmak, M.H., and Aytaç, Z. 2020. Determination and mapping of EUNIS habitat types of Mamak District (Ankara), Turkey. *Acta Biologica Turcica*, 33(4), 227-236.
- Cardinale, BJ., Srivastava, DS., Duffy, JE., Wright, JP., Downing, AL., Sankaran, M., and Jouseau, C. 2006 Effects of biodiversity on the functioning of trophic groups and ecosystems. *Nature* 443, 989-992. (doi:10. 1038/nature05202)
- Černecký, J., Gajdoš, P., ŠpuleroVá, J., Halada, L., Mederly, P., Ulrych, L., ... and Rybanič, R. 2020. Ecosystems in Slovakia. *Journal of Maps*, 16(2), 28-35.
- Chytrý, M., Tichý, L., Hennekens, S. M., KnolloVá, I., Janssen, J. A., Rodwell, J. S., ... and Schaminée, J.H. 2020. EUNIS Habitat Classification: Expert

- system, characteristic species combinations and distribution maps of European habitats. *Applied Vegetation Science*, 23(4), 648-675.
- Davis, P.H. (Eds) 1965-1985. *Flora of Turkey and the East Aegean Islands*, Vol 1-9. Edinburgh University, Edinburgh
- Eken, G., Bennun, L., Brooks, T. M., Darwall, W., Fishpool, L. D., Foster, M., ... and Tordoff, A. 2004. Key biodiversity areas as site conservation targets. *BioScience*, 54(12), 1110-1118.
- Eken, G., Bozdoğan, M., İsfendiyaroğlu, S., Kılıç, D. T., and Lise, Y. 2006. Türkiye'nin Önemli Doğa Alanları. *Doğa Derneği*, Ankara, 2, 348-351
- European environment agency. (September, 2021.). EUNIS habitat type hierarchical view. https://eunis.eea.europa.eu/habitats-code-browser.jsp?expand=#level_G
- Geven, F., Ozdeniz, E., Kurt, L., Bolukbasi, A., Ozbey, B. G., Ozcan, A. U., and Turan, U. 2016. Habitat Classification and Evaluation of the Köyceğiz-Dalyan Special Protected Area (Muğla/Turkey). *Rendiconti Lincei*, 27(3), 509-519.
- Krausmann, F., Erb, K-H., Gingrich, S., Haberl H, Bondeau A, Gaube V, Lauk C, Plutzer C, and Searchinger. TD. 2013 Global human appropriation of net primary production doubled in the 20th century. *Proc. Natl Acad. Sci. USA* 110, 10 324-10 329. (doi:10.1073/pnas.1211349110)
- Kromp-Kolb, and H., Formayer, H. 2005. *Schwarzbuch Klimawandel. Wie viel Zeit bleibt unsnoch?*. Ecowin Verlag der Top Akademie GmbH,
- Martinuzzi, S., Withey, J. C., Pidgeon, A. M., Plantinga, A. J., McKerrow, A. J., Williams, S. G., ... and Radeloff, V. C. 2015. Future land-use scenarios and the loss of wildlife habitats in the southeastern United States. *Ecological Applications*, 25(1), 160-171.
- McDermid, G. J., Franklin, S. E., and LeDrew, E.F. 2005. Remote sensing for large-area habitat mapping. *Progress in Physical Geography*, 29(4), 449-474.
- Mergen, O., and Karacaoğlu, C. 2015. Tuz Lake Special Environment Protection Area, Central Anatolia, Turkey: The EUNIS Habitat Classification and Habitat Change Detection between 1987 and 2007. *Ekoloji Dergisi*, 24, 95.
- Moss, D. 2008. EUNIS Habitat Classification – a Guide for Users. European Topic Centre on Biological Diversity, Paris.
- Moss, D. 2008. EUNIS habitat classification. European topic centre on biological diversity. 27 pp. Retrieved from <http://citeseerx.ist.psu.edu/viewdoc/download?doi=10.1.1.231.4607&rep=rep1&type=pdf>
- Newbold, T., Hudson, L. N., Phillips, H. R., Hill, S. L., Contu, S., Lysenko, I., ... and Purvis, A. 2014. A global model of the response of tropical and sub-tropical forest biodiversity to anthropogenic pressures. *Proceedings of the Royal Society B: Biological Sciences*, 281(1792), 20141371.
- Omann, I., Stocker, A., and Jäger, J. 2009. Climate change as a threat to biodiversity: An application of the DPSIR approach. *Ecological Economics*, 69(1), 24-31.
- Rouse, J.W., Haas, R.H., Schell, J.A., and Deering, D.W. 1974. Monitoring vegetation systems in the Great Plains with ERTS. NASA special publication, 351(1974), 309.
- Salzburg, Dow, K., and Downing, T.E., 2006. *The Atlas of Climate Change. Earthscan*
- Schamberger, M, and Krohn, WB. 1982. Status of the habitat evaluation procedures. *Trans N Amer. Wildl. Nat Resour Gmf* 47,154-164
- Schroeder, RL. 1986. Habitat suitability index models: wildlife species richness in shelter belts. *US Fish and Wildlife Service Biological Report* 82,10-128
- Süel, H., Şentürk Ö., Mert A., Özdemir S., and Yalçınkaya B. 2018. Habitat Suitability Modeling and Mapping. V. International Multidisciplinary Congress of Eurasia Proceedings July 24-26, 2018, Barcelona, Spain, 536-549.
- Tilman, D., Reich, PB., Knops, J., Wedin, D., Mielke, T., and Lehman, C. 2001. Diversity and productivity in along-term grassland experiment. *Science* 294, 843-845. (doi:10.1126/science.1060391)
- Vie´, J-C., Hilton-Taylor, C, and Stuart SN. 2009 *Wildlife in a changing world: an analysis of the 2008. Red List of Threatened Species*. Gland, Switzerland: IUCN.
- Yavaşlı, D.D., and Ölgen, M.K. 2008. Assessing the variation of recent glaciers in Buzul (Cilo) mountain with remote sensing and meteorological data. In *International Conference on Geographic Information Systems (ICGIS)* (pp. 2-5).

Available online at www.dergipark.gov.tr/beuscitech

Journal of Science and Technology

E-ISSN 2146-7706



Experimental and numerical analysis of weir structures in open channel flows

Ali Emre ULU ^{a,*} , M. Cihan AYDIN ^a , Fevzi ÖNEN ^b 

^a Bitlis Eren University, Department of Civil Engineering, TR-13000, Bitlis Turkey

^b Dicle University, Department of Civil Engineering, TR-21000, Diyarbakır Turkey

ARTICLE INFO

Article history:

Received 15 October 2021

Received in revised form 11 November 2021

Accepted 16 November 2021

Keywords:

Computational fluid dynamics (CFD)

Experimental model

Discharge coefficient

Inclined-bed

Rectangular labyrinth

ABSTRACT

Weirs are important water structures used to hold water in dams and canals and to safely transfer water from upstream to downstream. Due to these features, these structures, which have been used for years, have many different designs. In this study, a rectangular labyrinth weir and an inclined-bed rectangular weir were studied experimentally and numerically. The weir geometries used in the experiment were produced in a 3D printer and transferred to the numerical simulation with the same dimensions. The discharge and discharge coefficients corresponding to five different upstream heights obtained from the experiment and numerical simulation were obtained and the data were compared. Comparison of numerical and experimental results showed a good agreement. Where the difference between the tests is maximum was calculated at $H_o/P = 0.1$ m where the water load is the lowest.

© 2021. Turkish Journal Park Academic. All rights reserved.

1. Introduction

Weirs are hydraulically important structures that are built in different types and shapes, used to drain excess water that passes through a canal or in the dam reservoir. While determining the weir types in open channels, issues such as the maximum flow and velocity of the flow expected to pass through the channel should be considered. In structures with limited cross-section such as open channels, designs that increase the spillway capacity come to the fore. One of the most common and effective methods used to increase the amount of water taken from the channels is to increase the water contact surface of the weirs. Different types of designs determined to increase the performance of the weirs are determined in the light of the data obtained from experimental, theoretical and numerical studies. It has been shown by the studies in the literature that the performance of the labyrinth style weirs is much higher than the weirs designed in the classical style (straight) and are widely used in practice. Some studies in the literature can be given as follows.

Aydin and Ulu (2017) numerically examined the effects of antivortex to reduce flow turbulence over labyrinth side weirs. Anderson and Tullis (2012) compared the efficiency of Piano Key weirs (PKW) with rectangular labyrinth weirs in a laboratory setting. The results showed that the performance of Piano Key type weirs is more efficient than rectangular labyrinth weir. Sadeghian et al. (2019) investigated the advantages of inclined-bed application for triangular labyrinth side weirs. In the study, more than 160 experimental laboratory tests were performed and different hydraulic and geometry variables were used. Le et al. (2021) compared the discharge capacity of piano key and rectangular labyrinth weirs using a three-dimensional numerical model validated by available experimental data. Balzner et al. (2017) investigated piano key and labyrinth weirs on different geometries under free and submerged flow conditions and compared the findings. Aydin et al. (2019a), worked on the determination of water surface profiles in high-head spillways using computational fluid dynamics method. Khanh (2017), describes the initial procedure for laboratory research on

* Corresponding author. Tel.: +90 434 222 0000-3618

E-mail address: aeulu@beu.edu.tr

ORCID: 0000-0001-7499-3891 (A.E. Ulu), 0000-0002-5477-1033 (M.C. Aydin), 0000-0002-2368-1035 (F. Önen)

Piano Keyweirs (PKW) in 2004. Also, the study gives some information about existing and projected dams with PKW. Aydın et al. (2019b) conducted a detailed analysis study on trapezoidal labyrinth weirs using computational fluid dynamics (CFD) method. Kabiri-Samani (2013) carried out experimental and analytical tests on rectangular labyrinth weir. The results showed that this type of weir can be five times more productive than a conventional weir. Aydın and İşik (2015) examined hydraulic structures using a CFD software in their study and stated the advantages and disadvantages of using such programs in hydraulic structures. In addition to these, Schleiss (2011), Azimi and Hakim (2019), Anderson and Tullis (2013), Crookston and Tullis, (2012) and Ghanbari and Heidarnejad (2020) have comprehensive studies in literature.

Labyrinth weirs are currently used as a water intake structure in open channels and surface flowing spillways. These weirs, which have different types of designs and sizes, have high weir capacity at low nappe loads. They increase the capacity of reservoirs and channels and minimize nappe loads. In this study, a rectangular labyrinth weir and an inclined-bed rectangular weir type that inspired from piano-key weirs were studied using experimental and computational fluid dynamics (CFD) methods. Inclined-bed rectangular weirs have not been studied as widely in the literature as other weir types. For this content, the study contributed to the literature in this context. The three-dimensional models prepared in the CAD environment were printed on a three-dimensional printer and used in the experiments and transferred to the numerical analysis program in accordance with the 1/1 scale and the analyses were carried out. The data obtained from the experiments were analysed in the numerical analysis program and comparisons were made. As a method in the study, an open channel laboratory set and a developed CFD numerical analysis program were used.

2. Material and method

Two methods were used in the study. The first is laboratory work and the other is FLOW-3D, a computational fluid dynamics software. The length of the open channel setup used in the experiments is 4.0 m and the width is 0.40 m. The experiments were carried out without slope. The pump with a power of 2200 W produces a flow of 1300 l/min. The amount of water entering the channel was measured with a flowmeter. Discharge over sharp crested rectangular labyrinth weirs can be expressed as:

$$Q = \frac{2}{3} * C_d * L * \sqrt{2g} * H_0^{3/2} \quad (1)$$

Here, Q is flow discharge over weir; C_d is discharge coefficient, L is total length of the crest; g is the gravitational acceleration and H_0 is total upstream head.

Another method used in the study is the FLOW-3D software program, which is a CFD program. Like other CFD software,

FLOW-3D is known for numerically solving a number of basic fluid equations to determine fluid motion. The basic equations of fluid motion are modelled using finite elements or volumes with the help of programs such as FLOW-3D. CFD method solves the theoretical and semi-empirical dynamical equations of compressible and incompressible fluids by using various numerical methods and computational tools. Momentum and continuity equations used in the FLOW-3D given as follows:

Momentum equation:

$$\begin{aligned} \frac{\partial u}{\partial t} + \frac{1}{V_F} \left[uA_x \frac{\partial u}{\partial x} + vA_y \frac{\partial u}{\partial y} + wA_z \frac{\partial u}{\partial z} \right] &= -\frac{1}{\rho} \frac{\partial p}{\partial x} + G_x + f_x \\ \frac{\partial v}{\partial t} + \frac{1}{V_F} \left[uA_x \frac{\partial v}{\partial x} + vA_y \frac{\partial v}{\partial y} + wA_z \frac{\partial v}{\partial z} \right] &= -\frac{1}{\rho} \frac{\partial p}{\partial y} + G_y + f_y \\ \frac{\partial w}{\partial t} + \frac{1}{V_F} \left[uA_x \frac{\partial w}{\partial x} + vA_y \frac{\partial w}{\partial y} + wA_z \frac{\partial w}{\partial z} \right] &= -\frac{1}{\rho} \frac{\partial p}{\partial z} + G_z + f_z \end{aligned} \quad (2)$$

Continuity equation:

$$\frac{\partial}{\partial x}(uA_x) + \frac{\partial}{\partial y}(vA_y) + \frac{\partial}{\partial z}(wA_z) = 0 \quad (3)$$

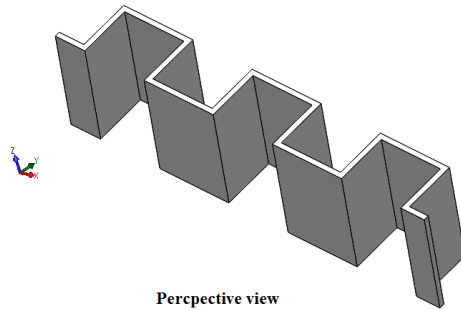
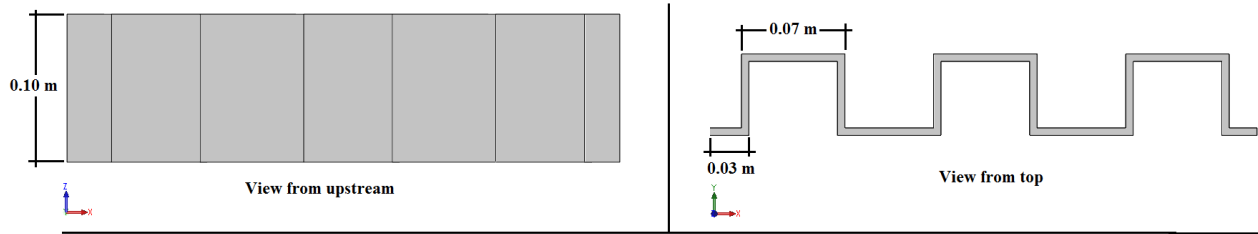
here, t is time, ρ is the fluid density, V_f is the volume fraction, (u, v, w) are velocity components, (A_x, A_y, A_z) are fractional areas open to flow in Cartesian coordinates. (G_x, G_y, G_z) are mass accelerations, (f_x, f_y, f_z) are viscous accelerations (Flow Science, 2019).

2.1. Rectangular labyrinth weir model

The prepared rectangular labyrinth weir with sharp edges is 0.10 m in height (P), 0.40 m in length, and 0.69 m in weir (crest) length (Fig. 1). The drawings prepared in the CAD environment were produced in two parts on a 3D printer due to the capacity of the printer, and then the parts were glued together. It has been determined that 10% fullness rate for the produced parts will have the desired strength and rigidity. The production process of this piece took twenty-five hours.

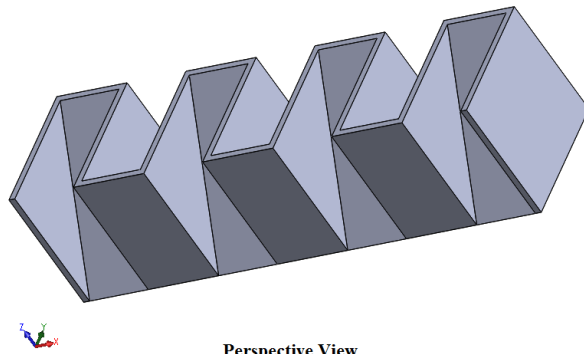
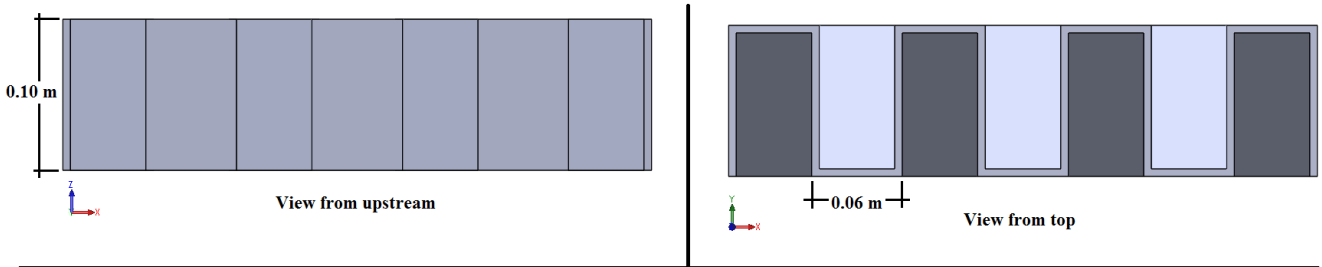
2.2. Inclined-bed rectangular weir model

The prepared inclined-bed rectangular weir is 0.10 m high (P), 0.40 m long and 0.99 m in weir (crest) length. Similar to the rectangular model, the drawings prepared in the CAD environment were produced in two parts in the printer due to the printer's capacity, and then the parts were glued together (Fig. 2). It has been determined that 10% fullness rate for the produced parts will have the desired strength and rigidity as well. The production process of this piece took fifty hours. Figure 3 shows some images from the experimental setup.



Perspective view

Figure 1. Rectangular labyrinth weir.

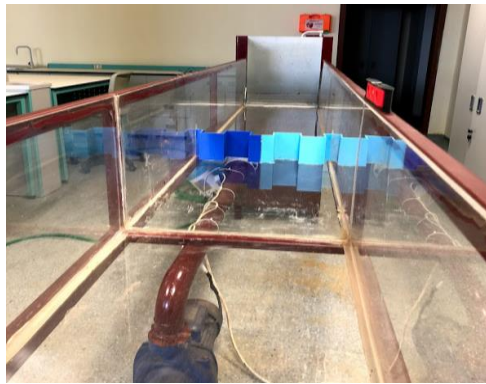


Perspective View

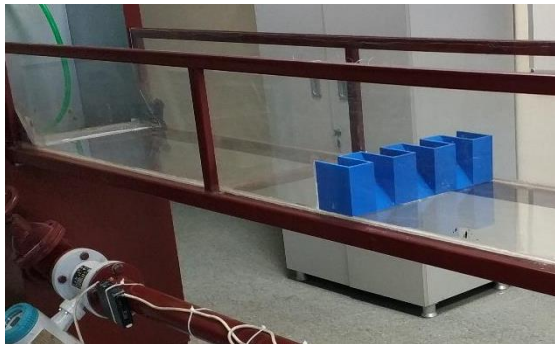
Figure 2. Inclined-bed rectangular weir.



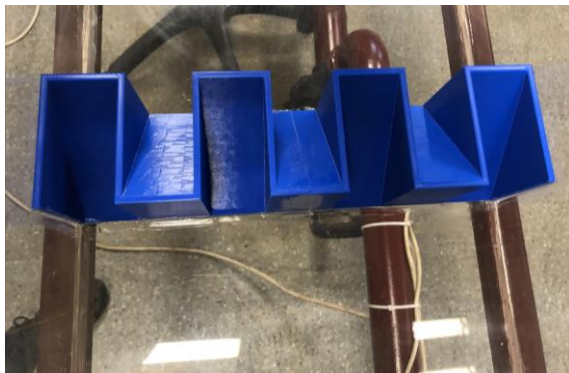
a)



b)



c)



d)

Figure 3. a-b) Views from upstream and downstream of rectangular labyrinth weir, c-d) Views from inclined-bed weir.

2.3. Numerical Model

The numerical model geometry was prepared in three dimensions according to its original dimensions as used in the experiment. In numerical model solutions, the quality of the solution network is very important in terms of receiving the data correctly and properly. On the other hand, the frequency of the mesh to be used for the model can significantly increase the processing time. An excessively high-resolution mesh structure may unnecessarily extend the solution time and cause an increase in numerical errors. In addition, the insufficient resolution of the solution mesh will cause the geometry to be not fully and accurately perceived by the CFD program. Therefore, it is useful to determine an optimum mesh size for the best numerical mesh structure (Figure 4-5). In the study, RNG (Renormalized Group) turbulent model is used. This model, which is similar to the k-epsilon turbulence model, is widely used in open channels.

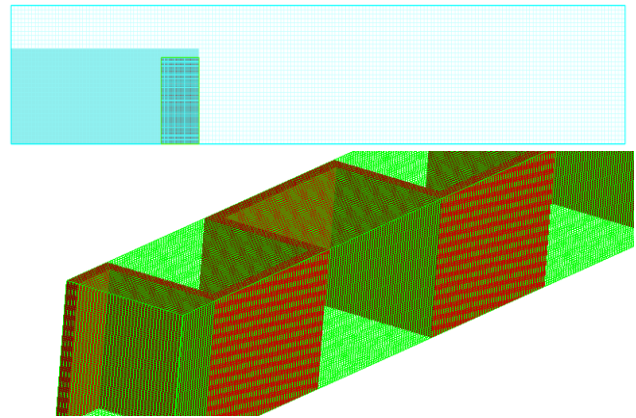


Figure 4. Rectangular labyrinth weir mesh structure.

FLOW-3D CFD software allows to create structured mesh. In the numerical model of the rectangular labyrinth situation, two different sizes of mesh blocks are used. The first net block is a 0.005 m net block that includes the weir. The second net block is 0.0015 m in size to cover the entire weir structure. The total number of mesh structure used is calculated as 1,225,424.

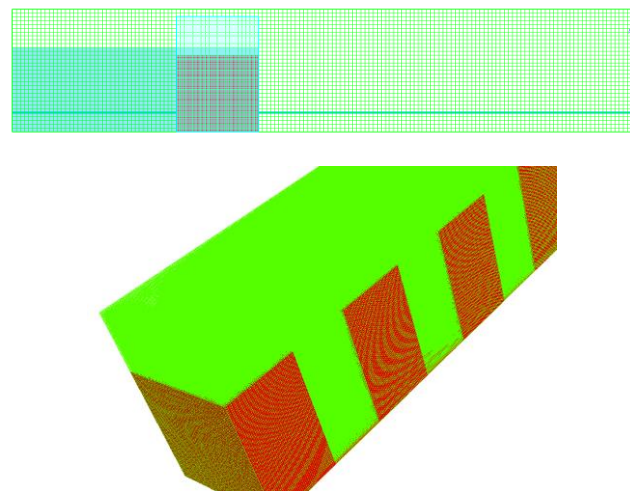


Figure 5. Inclined-bed rectangular weir mesh structure.

Similarly, in the numerical model of the inclined-bed situation, two different sizes of mesh blocks are used. The first mesh block is a 0.005 m mesh block that includes the weir. The second net block is 0.0015 m in size, including the entire weir structure and 0.05 m above the weir. The total number of mesh structure used in this model is given as 2,416,490.

2.4. Model Boundary Conditions

As in the channel design where the weir is located, the water inlet (*specified pressure*) is given from the channel entrance point (Figure 6). Since the upstream side of the weir is open to the atmosphere, it was evaluated as the *Specified Pressure*. The lower part of the sluice was defined as a *Wall*, and the remaining areas were left as *Symmetry*.

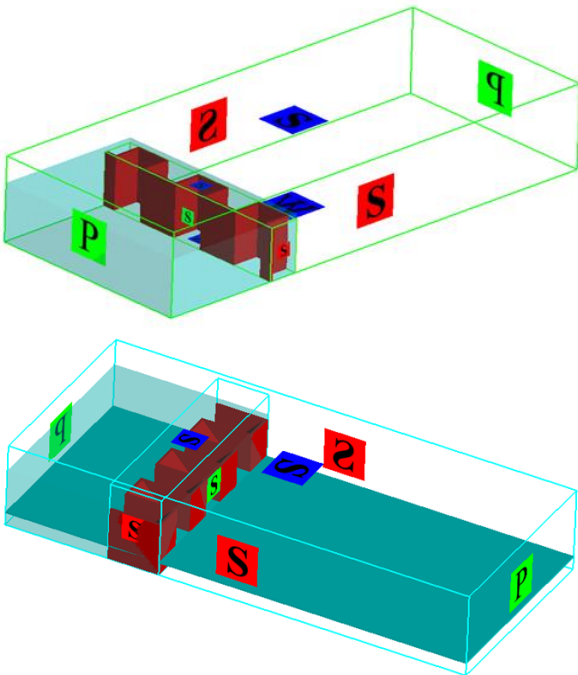


Figure 6. Model boundary conditions. (P: Specified Pressure; S: Symmetry; W: Wall)

In order to see the precision of the applied mesh resolution on the numerical model geometry, the images in the shapes were obtained by using the 'FAVOR' feature in FLOW-3D (Figure 7-8).

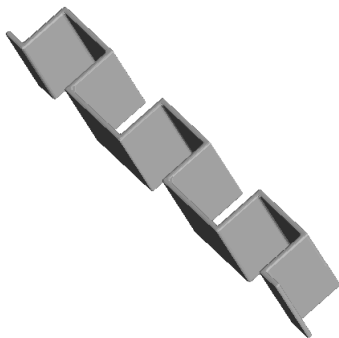


Figure 7. Designed rectangular labyrinth model 'FAVOR' image.

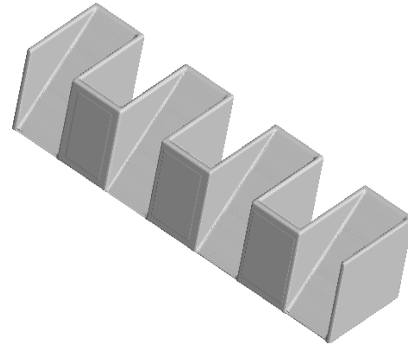


Figure 8. Designed inclined-bed rectangular model 'FAVOR' image.

3. Results

The weir types produced were tested in the laboratory using an open channel test set. Calculations in the experiments were made by measuring the discharges corresponding to five different upstream water levels of $H = 0.11$ m, $H = 0.12$ m, $H = 0.13$ m, $H = 0.14$ m and $H = 0.15$ m. In both cases, the difference in discharge in the test and CFD analyses was maximum at low nappe loads. The reason for this was thought to be due to insufficient mesh resolution compared to nappe load, and it was predicted that the results would be the same when the mesh quality was increased. Since the spillway capacity of a weir is important in terms of transferring maximum discharges, this difference at low nappe loads does not have a great effect. In the experiments, it was observed that the weir was operating with maximum efficiency at minimum nappe loads for both weirs, but as the nappe load increased, it was observed that the weir eyes were insufficient and the discharge capacity decreased.

3.1. Rectangular labyrinth weir

For rectangular labyrinth weirs, five different flow rates were obtained for five different water heights in the experiments carried out in the laboratory. In CFD analyzes prepared according to the original situation, upstream water levels obtained from the laboratory were used for each design. In the experiments, discharges corresponding to dimensionless $H_0/P=0.1-0.5$ m were calculated (Figure 10-11). In both experiments and numerical solutions, it was waited until the flow become steady at the determined height and the data were taken. In CFD analyses, it was observed that stabilization of the flow in low nappe load conditions requires a longer solution time compared to high nappe loads.

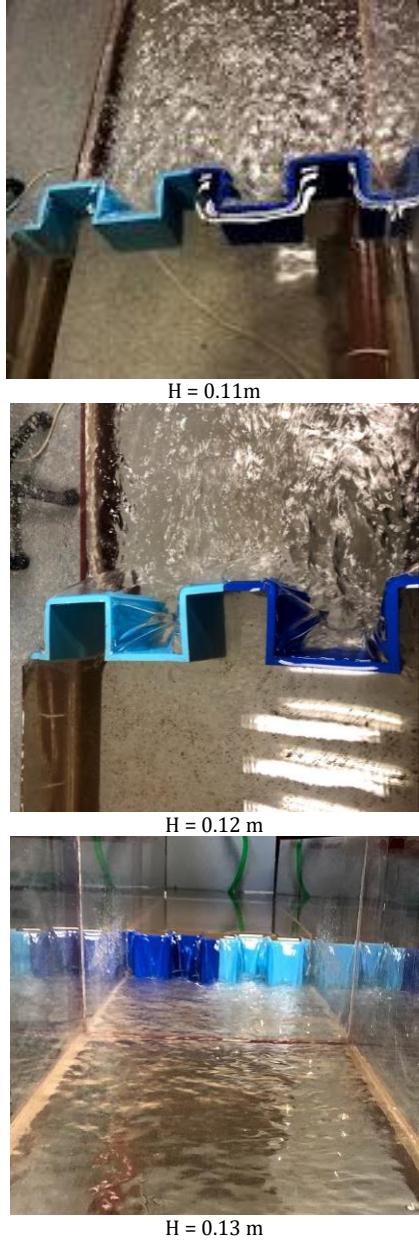


Figure 9. Some images from the moment of the experiment.

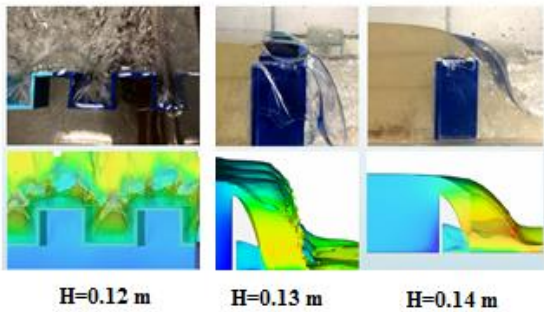


Figure 10. Comparison of flow conditions.

The situation where the difference between the tests is maximum was calculated at $H_0/P = 0.1$ m where the water load is the lowest. The reason for this difference at low nappe loads is thought to be due to insufficient mesh resolution compared to nappe load. It is predicted that better results can be obtained if a higher resolution mesh is used.

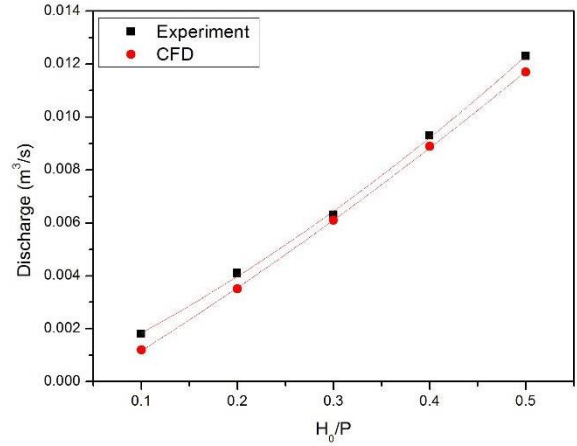


Figure 11. Comparison of rectangular labyrinth model experiment and CFD discharge.

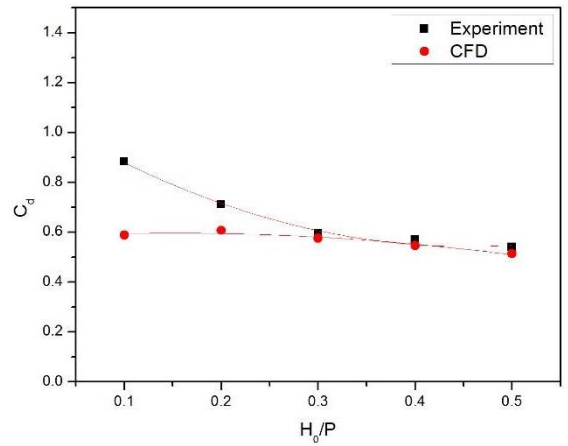


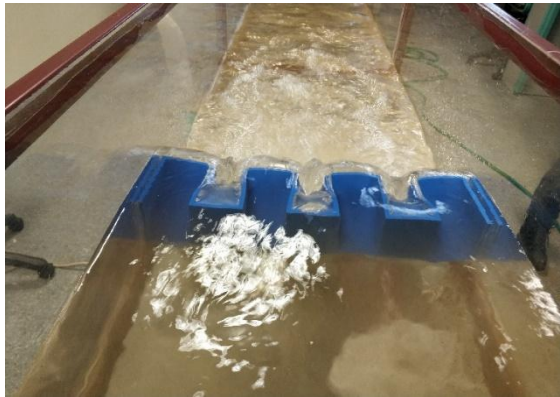
Figure 12. Experiment and CFD comparison of discharge coefficient of rectangular labyrinth model.

3.2. Inclined-bed rectangular weir

As in the rectangular labyrinth weir type, five different discharges were obtained in exchange for five water heights in these experiments. In CFD analyzes prepared according to the original situation, upstream water levels obtained from the laboratory were used for each design.

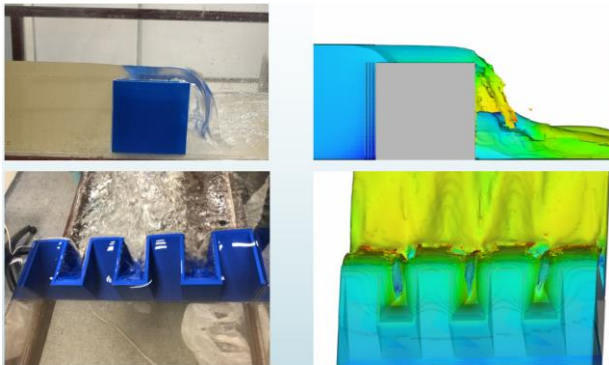


H = 0.12 m

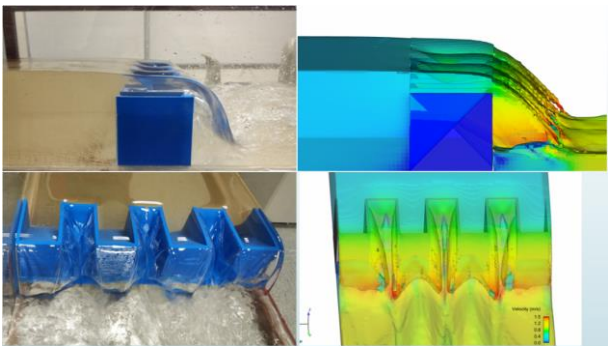


H = 0.12 m

Figure 13. Images from the moment of the experiment.



H= 0.11 m



H= 0.13 m

Figure 14. Comparison of flow conditions.

It was observed that the discharges obtained from $H_0/P = 0.4$ m and $H_0/P = 0.5$ m water head were very close to each other (Figure 15-16). It is seen that the discharge continues to increase linearly at maximum nappe load. It has been understood from the experimental results that if the nappe load continues to increase, the weir operates as a submerged flow.

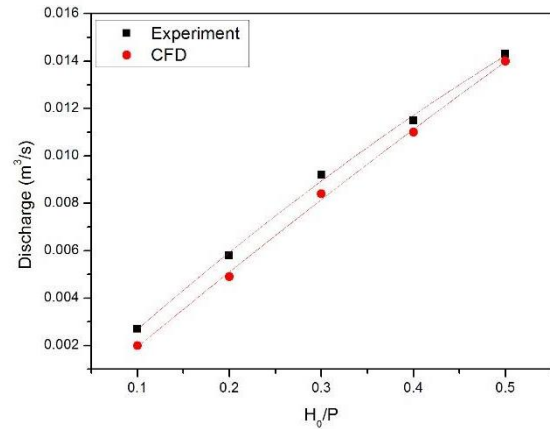


Figure 15. Comparison of inclined-bed rectangular model experiment and CFD discharge.

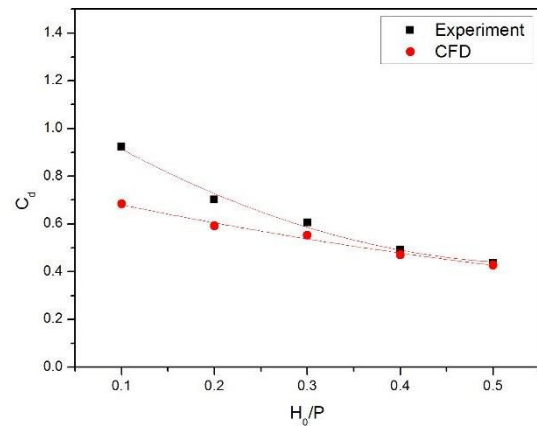


Figure 16. Experiment and CFD comparison of discharge coefficient of inclined-bed rectangular model.

3.3. Comparison of the weirs

Comparative CFD and experimental study discharge coefficients of weir structures with rectangular labyrinth and inclined-bed model are given in Figure 17-18. As can be seen from the graphs, the results of both cases show similar trends. In particular, it is seen that the data obtained from the experimental study are much closer. In addition to these, the comparison of numerical and experimental results also showed a good agreement. (Figure 19-20).

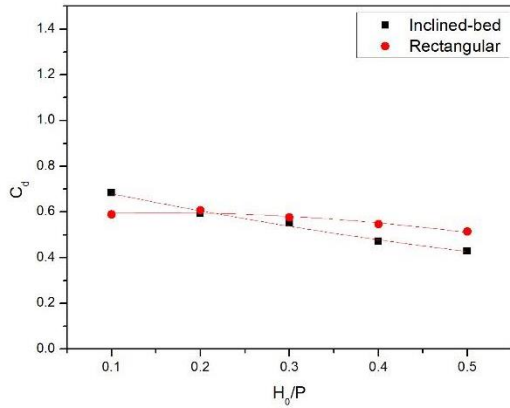


Figure 17. Comparison of rectangular labyrinth and inclined-bed model CFD discharge coefficients.

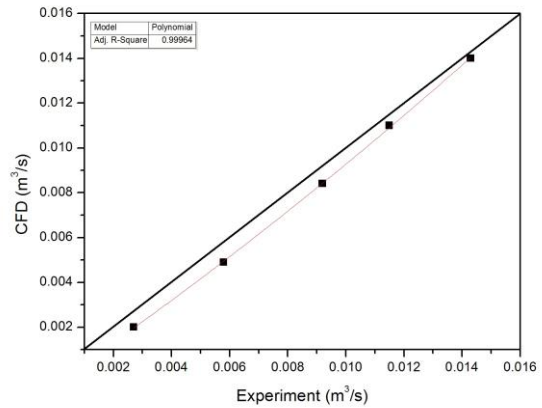


Figure 20. Comparison of inclined-bed rectangular weir discharge

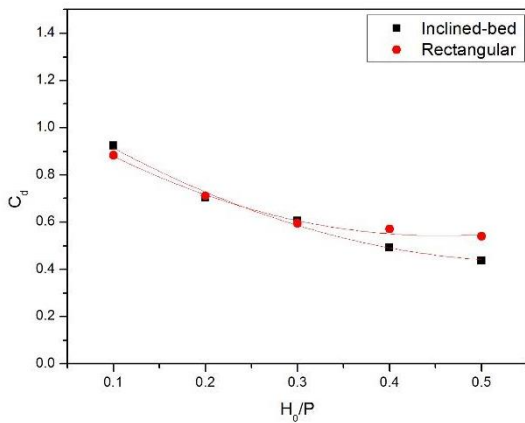


Figure 18. Comparison of rectangular labyrinth and inclined-bed model experiment discharge coefficients.

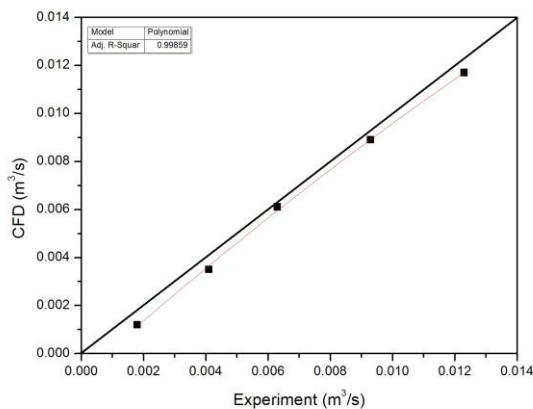


Figure 19. Comparison of rectangular labyrinth weir discharge

4. Conclusions

In the study, a rectangular labyrinth and an inclined-bed rectangular weir prepared in the CAD environment were produced with the help of a three-dimensional printer. Experiments of the produced parts were carried out in the laboratory using an open channel test set. Calculations in the experiments were made by measuring the discharges corresponding to five different upstream water levels of $H = 0.11$ m, $H = 0.12$ m, $H = 0.13$ m, $H = 0.14$ m and $H = 0.15$ m. Prototype dimensions were prepared in 3D digital environment and analyses were made under nap loads determined by using single-phase, Reynolds Averaged Navier-Stokes (RANS) turbulent flow model with the help of FLOW-3D. Parallel to the literature, it has been observed here that more discharge is obtained with the increase of the crest length. In both cases, the difference in discharge in the experimental and numerical results analyses was maximum at low nappe load. The reason for this was thought to be due to insufficient mesh resolution compared to nappe load, and it was predicted that the results would be the same when the mesh quality was increased. Since the spillway capacity of a weir is important in terms of transferring maximum discharges, this difference at low discharges does not have a great effect. According to the experimental results, it was observed that the weir was operating with maximum efficiency at minimum nappe loads for both weirs, but as the nappe load increased, it was observed that the weir eyes were insufficient and the flow capacity decreased.

Acknowledgements

In this study, the open channel experiment set obtained within the scope of Bitlis Eren University Scientific Research Project (BEBAP) was used.

References

- Anderson, R.M., and Tullis, B.P. 2012. Comparison of piano key and rectangular labyrinth weir hydraulics. *Journal of Hydraulic Engineering*, 138(4), 358-361.
- Anderson, R.M., and Tullis, B.P. 2013. Piano key weir hydraulics and labyrinth weir comparison. *Journal of Irrigation and Drainage Engineering*, 139(3), 246-253.
- Aydin, M.C., and Isik, E., 2015. Using CFD in Hydraulic Structures. *International Journal of Scientific and Technological Research*, Vol 1, No.5: 7-13
- Aydin, M.C., and Ulu, A.E. 2017. Antivortex effects on two-cycle trapezoidal labyrinth side weirs. *Journal of Irrigation and Drainage Engineering*, 143(7).
- Aydin, M.C., Bilhan, Ö., and Emiroğlu, M.E. 2019b. Trapez Labirent Savakların Hesaplamalı Akışkanlar Dinamiği (HAD) Kullanılarak Analizi. *DÜMF Mühendislik Dergisi* 10:2 (2019) :731-742
- Aydin, M.C., Işık, E., and Ulu, A.E. 2019a. Yüksek Düşülü Dolusavaklarda Su Yüzü Profillerinin Hesaplamalı Akışkanlar Dinamiğiyle Belirlenmesi. *DSİ Teknik Bülteni*, 133:1-11.
- Azimi, A.H., and Hakim, S.S. 2019. Hydraulics of flow over rectangular labyrinth weirs. *Irrigation Science*, 37(2), 183-193.
- Belzner, F., Merkel J., Gebhardt, M., and Thorenz, C. 2017. Piano Key and Labyrinth Weirs at German waterways: Recent and future research of the BAW. *Labyrinth and Piano Key Weirs III – PKW 2017*.
- Crookston, B.M., and Tullis, B.P. 2012. Labyrinth Weirs: Nappe Interference And Local Submergence, *Journal of Irrigation and Drainage Engineering*, Vol. 138, Number 8, pp. 757–765.
- Flow Science, 2019. *FLOW-3D User Manual*. Theory, Flow Science, Inc..
- Ghanbari, R., and Heidarnejad, M. 2020. Experimental And Numerical Analysis of Flow Hydraulics in Triangular and Rectangular Piano Key Weirs, *Water Science*, 2020, pp. 1–7.
- Ho Ta Khanh, M. 2017. History and development of Piano Key Weirs in Vietnam from 2004 to 2016. *Labyrinth and Piano Key Weirs III – PKW 2017*.
- Kabiri-Samani, A., Javaheri, A., and Borghei, S.M. 2013. Discharge coefficient of a rectangular labyrinth weir. In *Proceedings of the Institution of Civil Engineers-Water Management* (Vol. 166, No. 8, pp. 443-451).
- Le, A.T., Hiramatsu, K., and Nishiyama, T. 2021. Hydraulic Comparison Between Piano Key Weir and Rectangular Labyrinth Weir. *International Journal*, 20(82), 153-160.
- Sadeghian, H., Parvaneh, A., Nekooie, M.A., and Parvaneh, M. 2019. Discharge Characteristics of Triangular Labyrinth Side Weirs (With Inclined Bed) Located On A Straight Channel. *E-proceedings of the 38th IAHR World Congress September 1-6, 2019, Panama City, Panama*.
- Schleiss, A.J. 2011. From labyrinth to piano key weirs: A historical review. In *Proc. Int. Conf. Labyrinth and Piano Key Weirs Liège B* (pp. 3-15)



Available online at www.dergipark.gov.tr/beuscitech

Journal of Science and Technology

E-ISSN 2146-7706



Dynamic Conditional Dependence for Turkey Earthquake Data: CD Vine Copula Approach

Ayşe METİN KARAKAŞ^{a,*} , Aslihan DEMİR^b , Sinan ÇALIK^b 

^a Department of Statistic, Faculty of Art and Sciences, Bitlis Eren University, Bitlis, Turkey

^b Department of Statistic, Faculty of Sciences, Firat University, Elazığ, Turkey

ARTICLE INFO

Article history:

Received 14 October 2021

Received in revised form 16 November 2021

Accepted 16 November 2021

Keywords:

Dynamic Conditional Dependence,

Copula,

CD Vine Copula

ABSTRACT

The objective of this research was to use Turkey's major fault zones, which are located on fault lines, to describe the dependency structure. The current study also intended to show the dynamic structure of the conditional dependencies of the earthquake data in Turkey in terms of depth and magnitude, using the CD-vine copula method. Conditional dependence, also known as the CD-vine method, makes obtaining a complex dependency structure simpler. The current research uses 30 years of data from the Eastern Anatolian Fault line and the North Anatolian Fault line to describe the dynamic conditional dependency structure. As a consequence, this dependency structure is represented graphically and numerically in tables and graphs.

© 2021. Turkish Journal Park Academic. All rights reserved.

1. Introduction

[1] Investigated the dynamics co movement between capital markets in ASEAN Exchanges for during period of 2012-2013 and studied based on C-D Vine copula approach found the dynamics co-movement among of capital markets in ASEAN Exchanges. [2] studied focuses on the pattern of relation among major world exchanges such as the United States stock market (S & P 500), European stock markets (the united kingdom and German), Asia stock markets (Japan and China) and ASEAN stock markets (Indonesia and Philippine) in the pre-crisis period (2000 ~ 2008) and post-crisis period (2000 ~ 2016). Using the C-D Vine copula approach and in their results, they found the dynamic change between stock markets in the world financial markets. [3] used the vine copula analysis to analyze the composite stock price index and some of the macroeconomics (inflation, IDR to USD exchange rate and interest rate). In addition, the dependent structure was applied to obtain the common density function and they calculated the expected value as a copula regression model. [4]

presented, the canonical vine (C-vine) and D-vine copulas provide functions and tools for the extraction of stolen R-package presents CDVine. [5] examined the daily informational structure and common movements of the Thai Baht (THB) and Malaysian Ringgit (MYR) currencies in the period 2006-2013. [6] proposed vine copula mixes for the dependency structure hidden in multidimensional data. They tested a finite number of C- and D-vine model mixtures using the same copula family and finally studied the original CD-vine model, which enables the analysis of the dependency structure between many variables. [7] examined the relationship between bitcoin and other cryptocurrency indicators using the CD Vine Approach method.[8] To uncover and fully understand complex and latent dependence patterns in multivariate data, they proposed a D-vine copula mix that incorporates D-vine copula into a finite mix model. In addition, the model they propose can facilitate the scope of their multivariable complex and confidential content models.[9] presented the design of the R package copula, other implementation details.[10] have presented an intuitive systemic risk model for analyzing complex complex problems between different borrowers.

* Corresponding author. Tel.: +90 434 2220020

E-mail address: aysekarakas5767@gmail.com

ORCID : 0000-0003-3552-0105 (A. Metin Karakas), 0000-0003-4532-1564 (A. Demir) , 0000-0002-4258-1662 (S. Çalık)

Then, they used the state-of-the-art canonical (C-) and D-vine bridge to investigate the correlation structure between the divisions between the groups. [11] have used vine copula models to capture climate-efficiency dependency patterns, including the occurrence of extreme events (i.e. tail dependencies). Inc et al. [12] obtained approximate solutions of nonlinear time-dependent generalized Fitzhugh–Nagumo equation with time-dependent coefficients and Sharma–Tasso–Olver equation subjected to certain initial conditions and showed that this method is efficient and convenient; thus it can be applied to variety of problems. The approximate solutions are compared with the exact solutions. Then, Acay and Inc [13] proposed non-local singular fractional operators and examined this model, which has a very important place in everyday life. In 2020, Houwe et al. [14] studied analytical solutions of nonlinear differential equations (DED) with fractional derivatives and used the discrete tanh method for the calculations. In addition, Akinlar et al. [15] take an epidemic system with additional fractional white noise, build a new SIRS model and mix it into the fractional model, to show that epidemics can be modeled more competently in fractional-stochastic environments than those modeled by fractional-stochastic environments. deterministic differential equations. -stochastic systems and their chaotic behavior at unscathed and endemic equilibrium points have been studied. Later, Akinlar et al. [16], optimal control formulations, digital solutions, stability analysis for the fractional malchus model is considered a new contribution because it is studied for the first time in this article. Later in the same year, Korpınar et al. [17] analyzed the fractional-cubic-cubic-stochastic non-linear-stochastic schrödinger equation, which describes the propagation of the solitons through the optical fibers, and used it to obtain stochastic solutions in space White noise with hermit transform. In addition, Hashemi et al. [18] used the diagram of Adams-Bashforth-Moulton (ABMS) to determine the approximate solution of the fractional three-dimensional chaotic process at varying degrees, showing the results of the simulation. In this study, it is a question of explaining the dependency structure using the Copulule CD-Vigne approach for the main zones of faults located on the fault lines of Turkey. Conditional dependency, in other words CD-vine approach, provides convenience in obtaining the complex dependency structure. The present study explains the dynamic conditional dependency structure using 30 years of data of the regions on the Eastern Anatolian Fault line and the North Anatolian Fault line. As a result, this dependency structure is presented in graphics and tables.

2. Materials and Methods

Definition 2. 1. 1. Copula Function

A copula is a multivariate distribution whose marginals are all uniform over [0, 1]. For a n -dimensional vector U on the unit hyper cube, a copula C is defined as,

$$C(u_1, u_2, \dots, u_n) = \Pr(U_1 \leq u_1, U_2 \leq u_2, \dots, U_n \leq u_n) \quad (1)$$

This definition is the main result of the Sklar's theorem [17], namely building block of the theory of copulas, given below.

Theorem 2.1.2. (Sklar's Theorem) Let F be a n -dimensional distribution function with univariate margins F_1, F_2, \dots, F_n .

Let A_i define the range of F_i and $A_i = [-\infty, \infty]$ where $i = 1, 2, \dots, n$. At that case, there exists a copula function C whole $(x_1, x_2, \dots, x_n) \in [-\infty, \infty]$

$$F(x_1, x_2, \dots, x_n) = C(F(x_1), F(x_2), \dots, F(x_n)) \quad (2)$$

where the random variables (X_1, X_2, \dots, X_n) are assumed to be continuous.

Definition 2. 1. 2. Kendall Tau and Spearman Rho

rank correlations are defined as Spearman ρ and Kendall τ

For both rank based correlation measures, the general term in their formulations is the rank of the observation, indicated below

$$\widehat{\rho}_S(X, Y) = 12 \iint_U (C(u, v) - uv) dudv \quad (3)$$

$$\widehat{\rho}_\tau(X, Y) = 4 \iint_U C(u, v) \partial C(uv) - 1 \quad (4)$$

where, $U = I^2$ is the unique square.

Definition 2. 1. 3. Tail Dependence

The case of queue dependency is directly related to the extreme value relation defined mainly as a function of the queues. Suppose X and Y are two random variables having distributions F_X and F_Y respectively. Therefore, two important asymptotic measures for tail dependence, called upper and lower tail dependency coefficients, are mentioned below.

$$\lambda_l = \lim_{u \rightarrow 0} P(F_X(x) \leq u | F_Y(x) \leq u) = \lim_{u \rightarrow 0} C(u, u)/u \quad (5)$$

$$\lambda_u = \lim_{u \rightarrow 1} P(F_X(x) > u | F_Y(x) > u) = \lim_{u \rightarrow 1} 1 - 2u - C(u, u)/1 - u \quad (6)$$

where λ_l and $\lambda_u \in [0, 1]$.

Definition 2. 1. 4. Elliptical Copulas

Let F be the multivariate cumulative distribution function (cdf) of an elliptical distribution. Let F_i be CDF of the i 'th margin and

F_i^{-1} be its inverse function for $i = 1, 2, \dots, n$, the elliptical copula determined by F is;

$$C(u_1, u_2, \dots, u_n) = F[F_1^{-1}(u_1) + \dots + F_n^{-1}(u_n)] \quad (7)$$

For example; normal copulas (derived from the bivariate normal with zero mean, unitary and correlated variance) and Student's t pairs (derived from the bivariate t distribution with

zero mean, ν degrees of freedom and association) are two types of elliptic families.

Definition 2.1.5. Archimedean Copulas

An Archimedean copula is built using a generator ϕ as;

$$C(u_1, u_2, \dots, u_n) = \phi^{[-1]} [\phi(u_1) + \dots + \phi(u_n)] \quad (8)$$

where, $\phi^{[-1]}$ is the pseudo-inverse of the generator, ϕ defined by,

$$\phi^{[-1]} = \begin{cases} \phi^{-1}(t) & 0 \leq t \leq \phi(0) \\ 0 & \phi(0) \leq t \leq \phi(\infty) \end{cases} \quad (9)$$

In bivariate case,

$$C(u_1, u_2) = \phi^{[-1]} (\phi(u_1) + \phi(u_2)) \quad (10)$$

defines the so-called Archimedean bivariate copula function.

Definition 2.1.6. Vine Copulas

Let $T = U_1, U_2, \dots, U_{n-1}$ denote the regular vine for n variables, where U_i is a connected tree with nodes

$M_i = 1, 2, \dots, n$ and edges E_i for $i = 2, \dots, n-1$. In this tree structure, U_i is a connected tree with nodes $M_i = E_{i-1}$

A regular vine with p variables is a vine where two edges in tree i are connected by an edge in tree $i + 1$, only if these edges share a common node. In general, there are totally $n(n-2) / 2$ possible edges in a regular vine for n variables [19].

Definition 2.1.7. Conditional Copula

Given [19]

$$f(x_1, x_2, \dots, x_n) = \left(\prod_{k=2}^n f(x_k | x_1, x_2, \dots, x_{k-1}) \right) f_1(x_1) \quad (11)$$

and for distinct values of i, j, i_1, \dots, i_m with $i < j$ and $i_1 < \dots < i_m$ and describe

$$c_{i, j | i_1, i_2, \dots, i_m} = c_{i, j | i_1, i_2, \dots, i_m} (F(x_i | x_{i_1}, \dots, x_{i_m}), F(x_j | x_{i_1}, \dots, x_{i_m})) \quad (12)$$

where f and c respectively define the marginal probability density function (pdf.) and the copula density function. Then the conditional pdf can be written;

$$f(x_k | x_1, x_2, \dots, x_{k-1}) = c_{1, k | 2, \dots, k-1} f(x_k | x_2, \dots, x_{k-1}) = \sum_{q=1}^{k-2} (c_{q, k | q+1, \dots, k-1}) c_{k-1, k} f_k(x_k) \quad \dots(13)$$

by using equation (12) and (13) writing,

$$f(x_1, x_2, \dots, x_n) = \left(\sum_{j=1}^{n-1} \sum_{i=1}^{n-j} c_{i, i+j | i+1, \dots, i+j-1} \right) \sum_{m=1}^n f_m(x_m). \quad (14)$$

CD Vine Copula

A vine copula structure is simply defined as a nested set of trees that define binary copula functions unconditionally in the first tree and conditionally for the rest of the related trees. This structure is as follows;

Definition 2.1.8.C Vine Copula

It is a sort of regular vine distribution where each tree has a unique node connected to all the other nodes in the tree. It only uses star shaped trees and is useful for sorting by importance. The corresponding probability density function (pdf) can be written as:

$$f(x_1, x_2, \dots, x_n) = \prod_{k=1}^n f(x_k) \prod_{j=1}^{n-1} \prod_{i=1}^{n-j} c_{j, j+i | 1, \dots, j-1} \quad (15)$$

$$\left\{ F(x_j | x_1, \dots, x_{j-1}), F(x_{j+i} | x_1, \dots, x_{j-1}) \right\}.$$

Definition 2.1.8.D Vine Copula

D-vine is another special case for the normal vine tree structure which has no nodes in any tree but connects to more than two edges. It uses paths like trees and is useful for the temporal ordering of variables. The density function (pdf) can be written:

$$f(x_1, x_2, \dots, x_n) = \prod_{k=1}^n f(x_k) \prod_{j=1}^{n-1} \prod_{i=1}^{n-j} c_{i, i+j | i+1, \dots, i+j-1}$$

$$\left\{ F(x_i | x_{i+1}, \dots, x_{i+j-1}) F(x_{i+j} | x_{i+1}, \dots, x_{i+j-1}) \right\}.$$

3. Results

We use magnitude and depth of Eastern Anatolian fault line and North Anatolian fault line data of stations the period 1999-2019. Table 1 and Table 2 summarizes statistics of magnitude and depth of Eastern Anatolian fault line and North Anatolian fault line data. In Table 1, Table 2 and Figure 1, Figure 2 shows different mean values for the for data set, and the corresponding standard deviations are different. Skewness of data set is positive, indicating that this data is skewed right. The high kurtosis of data set reveals that extreme value changes often occur when the tail of return distributions shows fatness. The Jarque-Bera (JB) test shows that the normality of each return series distribution is strongly rejected at 0.05 level, which means all price index distributions are non-normal. The empirical distribution functions used in modelling the dependence of Eastern Anatolian fault line and North Anatolian fault line depth and magnitude data pairs are as shown in Figure 3,4,5,6,7,8,9,10 and Table 3,4. For this, we used C Vine and D Vine copula. In table 3,4,5 and Figure 1, 2, 3, 4 it is shown that for the relationship between North Anatolian fault line depth and North Anatolian fault line magnitude, in table 3,4,5 Figure 5,6,7,8 it is shown that for the relationship between Eastern Anatolian fault line depth and Eastern Anatolian fault line magnitude, we use C Vine and D Vine copula modelling. In Table 3,4, the preferred copula families for branching and the parameter summaries of these families are given. In Figure figure 3,4,5,6,7,8,9,10 for C Vine, D Vine matrix summaries and

appropriate branch graphs are shown. From table 3,4,5 Figure 3,4,5,6,7,8,9,10 for dependency structure of North Anatolian fault line depth, C vine branching was found to be appropriate according to the information criteria. Similarly, for North Anatolian fault line magnitude data. From table 3,4,5 Figure 3,4,5,6,7,8,9,10, for dependency structure of North Anatolian fault line magnitude, C vine branching was found to be appropriate according to the information criteria, for Eastern Anatolian fault line depth data, in table 3,4,5 Figure 3,4,5,6,7,8,9,10, for dependency structure of Eastern Anatolian fault line depth, D vine branching was found to be appropriate according to the information criteria and for Eastern Anatolian fault line magnitude data, in table 3,4,5 Figure 3,4,5,6,7,8,9,10 for dependency structure of Eastern Anatolian fault line magnitude, D vine branching was found to be appropriate according to the information criteria.

Table 1. Summary Statistics for Eastern Anatolian fault line

	Adıyaman	Elazığ	K.Maraş	Malatya	Şırnak
Depth					
Mean	8,243636	16,15455	18,00909	17,65455	15,19273
Maksimum	15,35000	45,40000	64,20000	45,40000	35,00000
Minumum	2,600000	2,000000	6,900000	9,500000	5,000000
Std.Dev	3,393636	15,43421	16,86265	11,13008	10,19934
Skewness	0,344330	0,929670	2,087951	1,594602	1,348772
Kurtosis	3,165211	2,248423	6,270340	4,557203	3,287966
Jarque Bera	0,229876	1,843424	12,89442	5,773121	3,373180
Probability	0,891421	0,397837	0,001585	0,055768	0,185150
Magnitude					
Mean	4,500000	4,309091	4,145455	4,318182	4,300000
Maksimum	5,500000	5,100000	4,500000	5,100000	5,100000
Minumum	4,000000	4,000000	4,000000	4,000000	4,000000
Std.Dev	0,473286	0,311302	0,180907	0,345885	0,354965
Skewness	0,908170	1,601171	0,874018	1,192958	1,097454
Kurtosis	2,771923	4,845286	2,344167	3,250882	3,163643
Jarque Bera	1,535924	6,260866	1,597635	2,637954	2,220351
Probability	0,463958	0,043699	0,449861	0,267409	0,329501

Table 2. Summary Statistics for North Anatolian fault line

	Çankırı	Düzce	Erzincan	İzmit	Sakarya
Depth					
Mean	11,04286	20,00000	27,87143	13,51429	17,64286
Maksimum	22,30000	65,60000	66,10000	22,60000	56,00000
Minumum	7,000000	10,00000	7,000000	7,000000	3,700000
Std.Dev	5,110074	20,70394	23,37404	5,863852	17,79671
Skewness	1,791256	1,828218	0,512661	0,553095	1,668841
Kurtosis	4,681279	4,624956	1,852352	1,783947	4,292637
Jarque Bera	4,567817	4,669584	0,690778	0,788212	3,736549
Probability	0,101885	0,096831	0,707945	0,674283	0,154390
Magnitude					
Mean	4,042857	4,685714	5,200000	4,928517	4,300000
Maksimum	4,200000	7,100000	6,600000	7,600000	4,500000
Minumum	4,000000	4,000000	4,600000	4,000000	4,100000
Std.Dev	0,078680	1,080785	0,797914	1,237894	0,163299
Skewness	1,357727	1,916392	0,822842	1,652398	0,248039
Kurtosis	3,233728	4,893136	2,175256	4,331803	1,421875
Jarque Bera	2,166593	5,329972	0,988305	3,702817	0,798167
Probability	0,338478	0,069600	0,610088	0,157016	0,670935

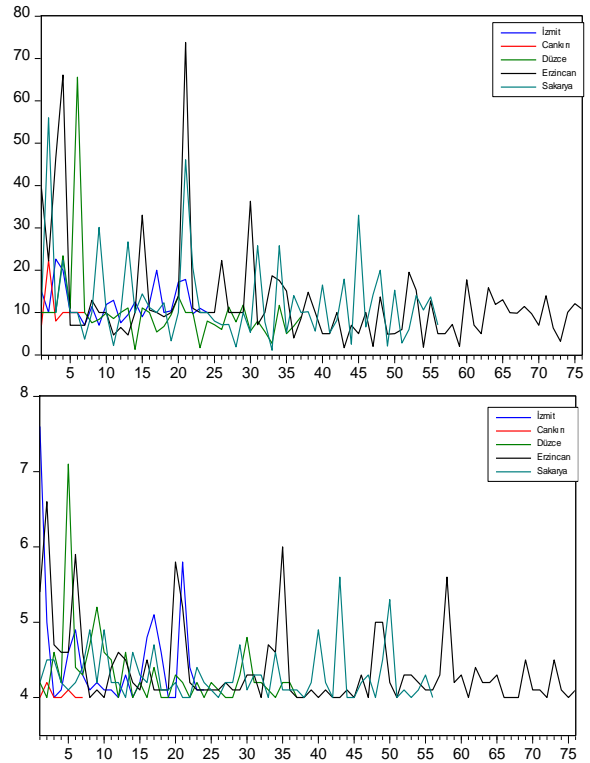


Figure 1. Respectively, Depth and Magnitude of North Anatolian fault line.

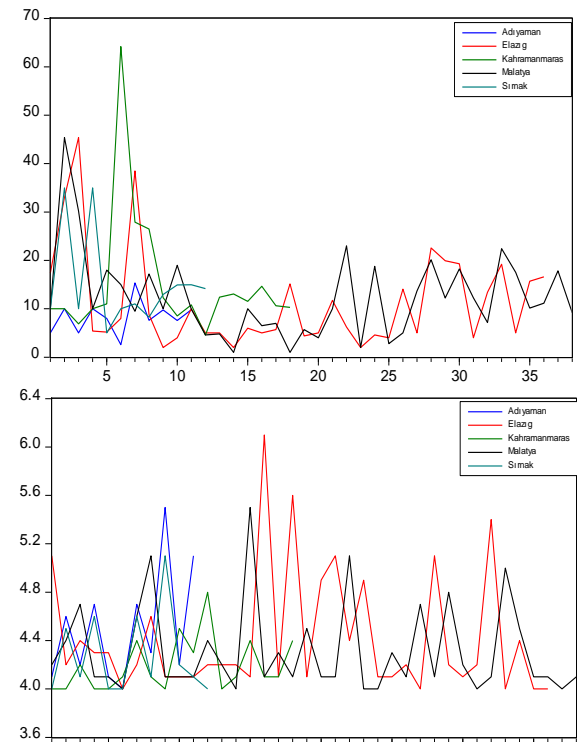


Figure 2. Respectively, Depth and Magnitude of Eastern Anatolian fault

Table 3. C-vine copula estimation results.

Depth of North Anatolian fault line	Copula	Par1	Par2	Tau	Lower tail dependency	Upper tail dependency
$C_{\text{Çankırı-İzmit}}$	I	-	-	0.00	-	-
$C_{\text{Düzce-İzmit}}$	C	2.88	0.00	0.59	-	0.79
$C_{\text{Sakarya-İzmit}}$	C	1.05	0.00	0.34	-	0.52
$C_{\text{Erzincan-İzmit}}$	C	0.56	0.00	0.22	-	0.29
$C_{\text{Erzincan,Çankırı/İzmit}}$	I	-	-	0.00	-	-
$C_{\text{Erzincan,Düzce/İzmit}}$	Tawn	18.00	0.90	0.85	0.89	-
$C_{\text{Erzincan,Sakarya/İzmit}}$	Tawn2_180	16.10	0.90	0.85	-	0.89
$C_{\text{Sakarya,Çankırı,Erzincan/İzmit}}$	I	-	-	0.00	-	-
$C_{\text{Sakarya,Düzce,Erzincan/İzmit}}$	SBB6	6.00	6.00	0.95	-	0.98
$C_{\text{Düzce,Çankırı,Sakarya,Erzincan/İzmit}}$	I	-	-	0.00	-	-
Magnitude of North Anatolian fault line	Copula	Par1	Par2	Tau	Lower tail dependency	Upper tail dependency
$C_{\text{Çankırı-İzmit}}$	I	-	-	0.00	-	-
$C_{\text{Düzce-İzmit}}$	C	2.88	0.00	0.59	-	0.79
$C_{\text{Sakarya-İzmit}}$	N	0.03	0.00	0.02	-	-
$C_{\text{Erzincan-İzmit}}$	C	0.56	0.00	0.22	-	0.29
$C_{\text{Erzincan,Çankırı/İzmit}}$	I	-	-	0.00	-	-
$C_{\text{Erzincan,Düzce/İzmit}}$	Tawn	18.00	0.90	0.85	0.89	-
$C_{\text{Erzincan,Sakarya/İzmit}}$	J	8.48	0.00	0.79	0.91	-
$C_{\text{Sakarya,Çankırı/Erzincan/İzmit}}$	I	-	-	0.00	-	-
$C_{\text{Sakarya,Düzce/Erzincan/İzmit}}$	C90	-0.96	0.00	-0.32	-	-
$C_{\text{Düzce,Çankırı/Sakarya,Erzincan/İzmit}}$	I	-	-	0.00	-	-
Depth of Eastern Anatolian fault line	Copula	Par1	Par2	Tau	Lower tail dependency	Upper tail dependency
$C_{\text{Elazığ-Şırnak}}$	Tawn2_90	-5.32	0.06	-0.06	-	-
$C_{\text{Malatya-Şırnak}}$	Tawn90	-20.00	0.30	-0.29	-	-
$C_{\text{Adıyaman-Şırnak}}$	Tawn2	5.45	0.47	0.42	0.46	-
$C_{\text{Kahramanmaraş-Şırnak}}$	Tawn2_270	-18.59	0.10	-0.10	-	-
$C_{\text{Kahramanmaraş,Elazığ/Şırnak}}$	Tawn2_270	-20.00	0.06	-0.06	-	-
$C_{\text{Kahramanmaraş,Malatya/Şırnak}}$	J90	-1.24	0.00	-0.12	-	-
$C_{\text{Kahramanmaraş,Adıyaman/Şırnak}}$	Tawn	4.17	0.43	0.38	0.43	-
$C_{\text{Adıyaman,Elazığ,Kahramanmaraş/Şırnak}}$	SBB1	0.93	1.00	0.32	0.48	0.00
$C_{\text{Adıyaman,Malatya,Kahramanmaraş/Şırnak}}$	Tawn90	-20.00	0.20	-0.20	-	-
$C_{\text{Malatya,Elazığ,Adıyaman,Kahramanmaraş/Şırnak}}$	t	0.07	2.00	0.04	0.20	0.20

Magnitude of Eastern Anatolian fault line	Copula	Par1	Par2	Tau	Lower tail dependency	Upper tail dependency
$C_{Elazığ-Şırnak}$	t	0.03	30.00	0.02	0.00	0.00
$C_{Malatya-Şırnak}$	J270	-1.07	0.00	-0.04	-	-
$C_{Adıyaman-Şırnak}$	SJ	15.94	0.00	0.88	-	0.96
$C_{Kahramanmaraş-Şırnak}$	SJ	15.94	0.00	0.88	-	0.96
$C_{Kahramanmaraş,Elazığ/Şırnak}$	C270	-0.00	0.00	-0.00	-	-
$C_{Kahramanmaraş,Malatya/Şırnak}$	F	-0.88	0.00	-0.10	-	-
$C_{Kahramanmaraş,Adıyaman/Şırnak}$	BB7_270	-1.02	-0.00	-0.01	-	-
$C_{Adıyaman,Elazığ,Kahramanmaraş/Şırnak}$	Tawn	2.76	0.32	0.26	0.30	-
$C_{Adıyaman,Malatya,Kahramanmaraş/Şırnak}$	Tawn2_180	1.85	0.00	0.00	-	0.00
$C_{Malatya,Elazığ,Adıyaman,Kahramanmaraş/Şırnak}$	G	1.09	0.00	0.08	0.11	-

Table 4. D-vine copula estimation results.

Depth of North Anatolian fault line	Copula	Par1	Par2	Tau	Lower tail dependency	Upper tail dependency
$C_{Erzincan-Sakarya}$	C	4.32	0.00	0.68	-	0.85
$C_{Sakarya-Izmir}$	C	1.05	0.00	0.34	-	0.52
$C_{Izmir-Düzce}$	C	2.88	0.00	0.59	-	0.79
$C_{Düzce-Çankırı}$	I	-	-	0.00	-	-
$C_{İzmit,Erzincan/Sakarya}$	N	-0.78	0.00	-0.57	-	-
$C_{Düzce,İzmit/Sakarya}$	Tawn2	20.00	0.93	0.89	0.92	-
$C_{Çankırı,İzmit/Düzce}$	I	-	-	0.00	-	-
$C_{Düzce,Erzincan/Sakarya,İzmir}$	BB7_270	-1.00	-1.65	-0.45	-	-
$C_{Çankırı,Sakarya/Düzce,İzmir}$	I	-	-	0.00	-	-
$C_{Çankırı,Erzincan/Düzce,İzmir,Sakarya}$	I	-	-	0.00	-	-

Magnitude of North Anatolian fault line	Copula	Par1	Par2	Tau	Lower tail dependency	Upper tail dependency
$C_{Erzincan-Izmir}$	C	0.56	0.00	0.22	-	0.29
$C_{Izmir-Sakarya}$	N	0.03	0.00	0.02	-	-
$C_{Sakarya-Düzce}$	C	0.02	0.00	0.01	-	0.00
$C_{Düzce-Çankırı}$	I	-	-	0.00	-	-
$C_{Sakarya,İzmit/Erzincan}$	J	8.48	0.00	0.79	0.91	-
$C_{Düzce,İzmit/Sakarya}$	C	3.57	0.00	0.64	-	0.82
$C_{Çankırı,Sakarya/Düzce}$	I	-	-	0.00	-	-
$C_{Düzce,Erzincan/Sakarya,İzmit}$	Tawn90	-10.77	0.31	-0.30	-	-
$C_{Çankırı,İzmit/Düzce,Sakarya}$	I	-	-	0.00	-	-
$C_{Çankırı,Erzincan/Düzce,Sakarya,İzmit}$	I	-	-	0.00	-	-

Depth of Eastern Anatolian fault line	Copula	Par1	Par2	Tau	Lower tail dependency	Upper tail dependency
$C_{\text{Şirnak-Kahramanmaraş}}$	Tawn90	-18.59	0.10	-0.10	-	-
$C_{\text{Kahramanmaraş-Adıyaman}}$	t	0.22	2.00	0.14	0.26	0.26
$C_{\text{Adıyaman-Malatya}}$	C270	-0.83	0.00	-0.29	-	-
$C_{\text{Malatya-Elazığ}}$	t	0.48	2.00	0.32	0.38	0.38
$C_{\text{Adıyaman,Şirnak/Kahramanmaraş}}$	J	2.88	0.00	0.50	0.73	-
$C_{\text{Malatya,Kahramanmaraş,/ Adıyaman}}$	C90	-0.70	0.00	-0.26	-	-
$C_{\text{Elazığ,Adıyaman/ Malatya}}$	J	1.20	0.00	0.10	0.21	-
$C_{\text{Malatya,Şirnak/ Adıyaman,Kahramanmaraş}}$	Tawn2_270	-19.27	0.43	-0.42	-	-
$C_{\text{Elazığ,Kahramanmaraş/ Malatya,Adıyaman}}$	Tawn	12.92	0.09	0.09	0.09	-
$C_{\text{Elazığ,Şirnak/ Malatya,Adıyaman,Kahramanmaraş}}$	BB1_90	-1.13	-1.00	-0.36	-	-
Magnitude of Eastern Anatolian fault line	Copula	Par1	Par2	Tau	Lower tail dependency	Upper tail dependency
$C_{\text{Adıyaman-Şirnak}}$	SJ	15.94	0.00	0.88	-	0.96
$C_{\text{Şirnak-Kahramanmaraş}}$	SJ	15.94	0.00	0.88	-	0.96
$C_{\text{Kahramanmaraş-Malatya}}$	SC	0.13	0.00	0.06	0.00	-
$C_{\text{Malatya-Elazığ}}$	Tawn270	-5.29	0.12	-0.11	-	-
$C_{\text{Kahramanmaraş,Adıyaman/Şirnak}}$	BB7_270	-1.02	-0.00	-0.01	-	-
$C_{\text{Malatya,Şirnak/Kahramanmaraş}}$	C	0.00	0.00	0.00	-	0.00
$C_{\text{Elazığ,Kahramanmaraş/ Malatya}}$	SJ	1.01	0.00	0.00	-	0.01
$C_{\text{Malatya,Adıyaman/Şirnak,Kahramanmaraş}}$	N	0.06	0.00	0.04	-	-
$C_{\text{Elazığ,Şirnak/Kahramanmaraş,Malatya}}$	Tawn2_180	20.00	0.01	0.00	-	0.01
$C_{\text{Elazığ,Adıyaman/ Malatya,Kahramanmaraş,Şirnak}}$	N	0.16	0.00	0.10	-	-

Table 5. Comparison of the C-vine and D-vine.

Tree	C vine	D vine.
Depth of North Anatolian fault line		
Loglike	62.7	55.79
AIC	-107.39576	-95.57715
BIC	-86.42	-76.93
Magnitude of North Anatolian fault line		
Loglike	38.83	39.39
AIC	-63.66569	-60.78
BIC	-47.35	-44.47
Depth of Anatolian fault line		
Loglike	21.47	22.52
AIC	-10.93	-13.034703
BIC	20.18	13.17
Magnitude of Anatolian fault line		
Loglike	30267.22	30285.76
AIC	-60506.43	-60545.53
BIC	-60483.51	-60524.24

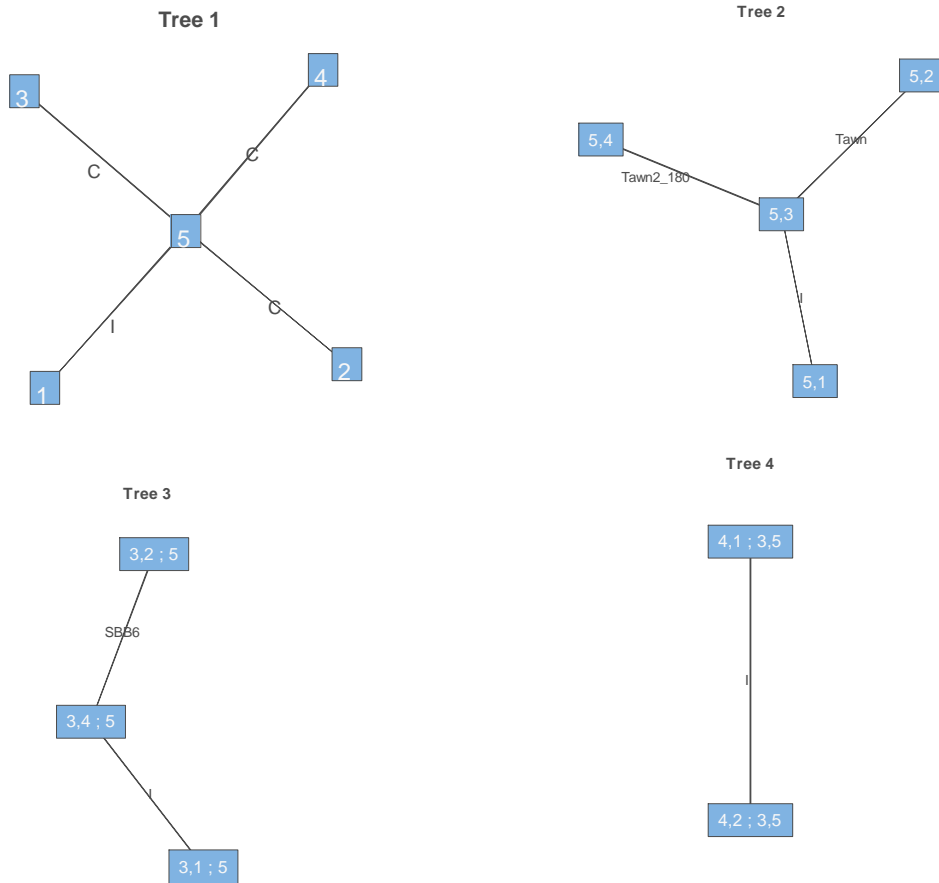


Figure 3. C Vine Copula Summary for Depth of North Anatolian fault line (1. Cankırı, 2. Düzce, 3. Erzincan, 4. Sakarya, 5. İzmit)

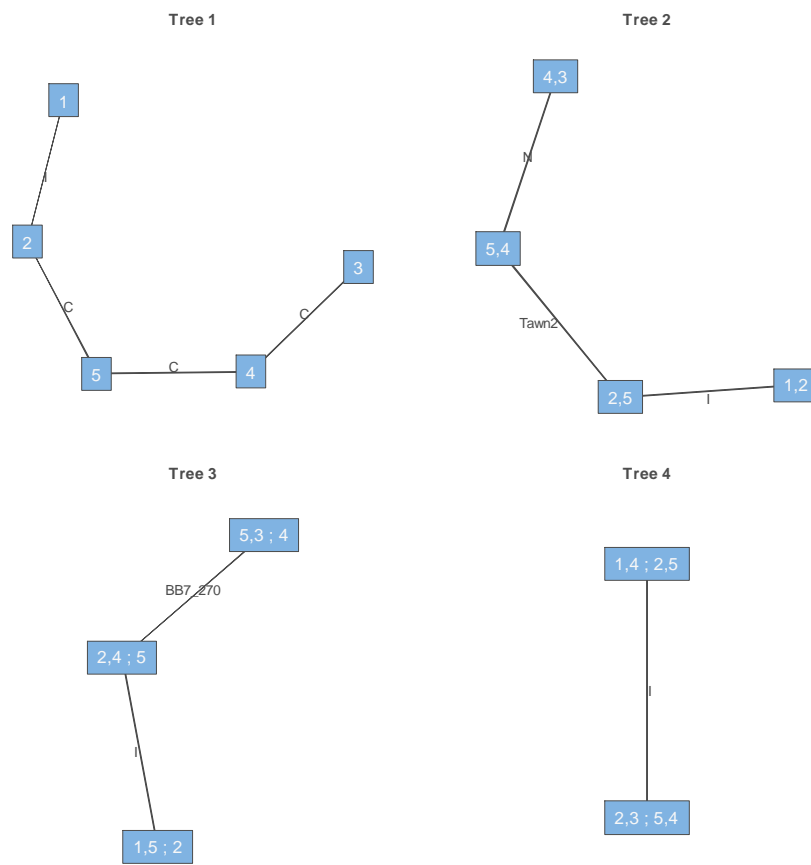


Figure 4. D Vine Copula Summary for Depth of North Anatolian fault line (1. Cankırı, 2. Düzce, 3. Erzincan, 4. Sakarya, 5. İzmit).

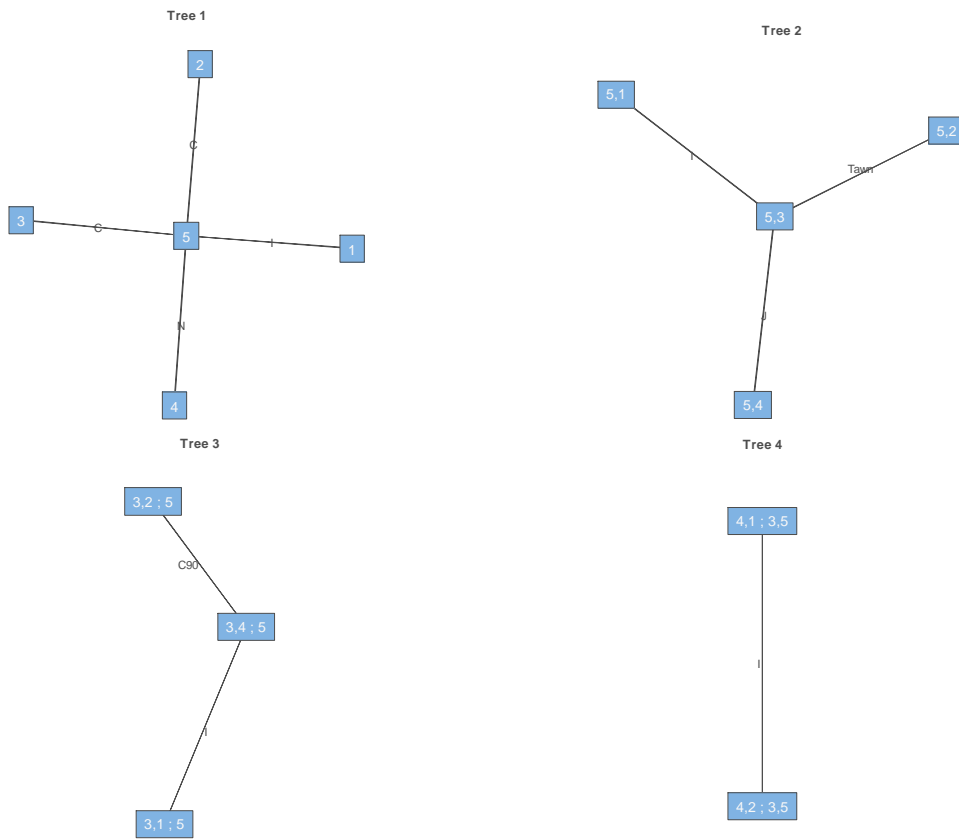


Figure 5. C Vine Copula Summary for magnitude of North Anatolian fault line (1. Cankırı, 2. Düzce, 3. Erzincan, 4. Sakarya, 5. İzmit).

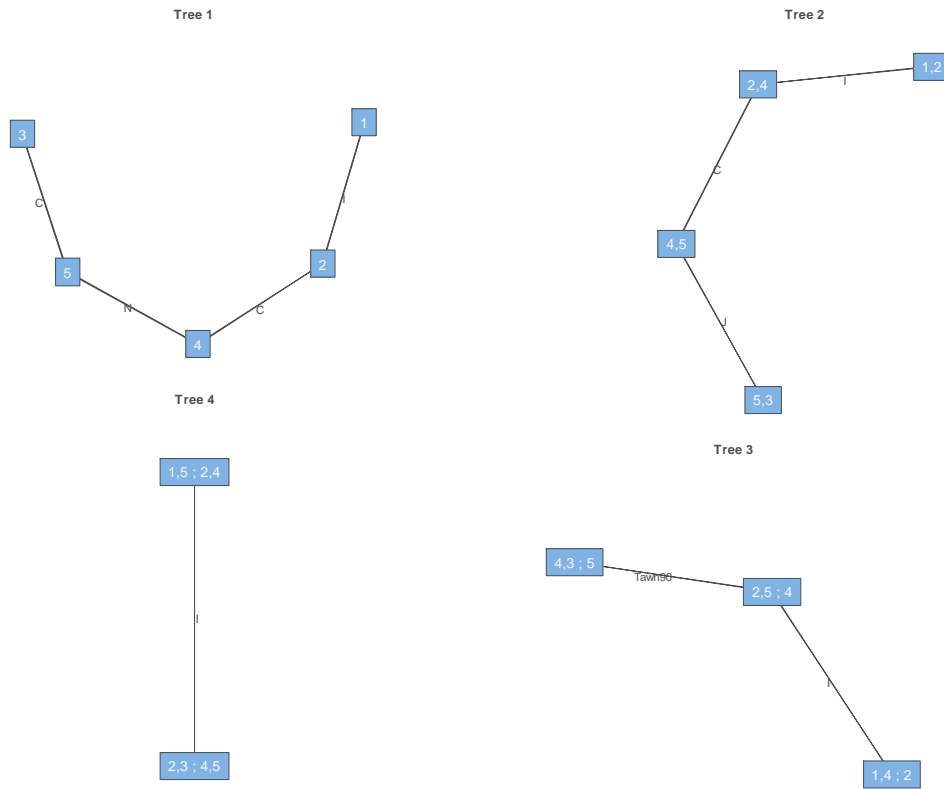


Figure 6. D Vine Copula Summary for Magnitude of North Anatolian fault line (1. Cankırı, 2. Düzce, 3 .Erzincan, 4. Sakarya, 5. İzmit).

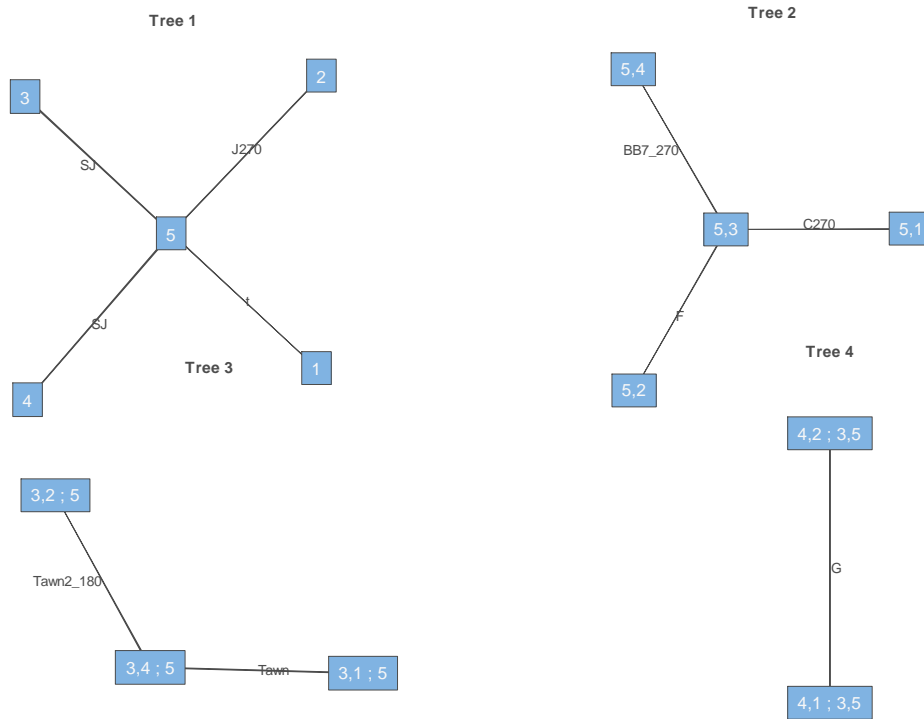


Figure 7. C Vine Copula Summary for depth of Eastern Anatolian fault line (1. Elazığ, 2. Malatya, 3. Kahramanmaras, 4. Adıyaman, 5. Sırnak)

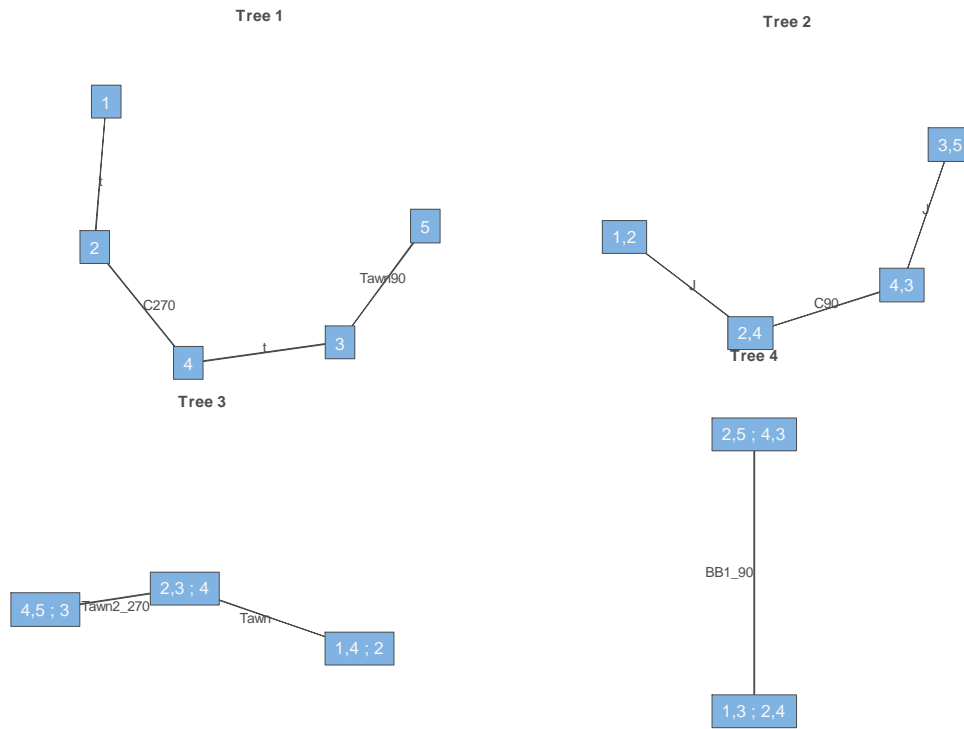


Figure 8. D Vine Copula Summary for depth of Eastern Anatolian fault line (1. Elazığ, 2. Malatya, 3. Kahramanmaras, 4. Adıyaman, 5. Sırnak).

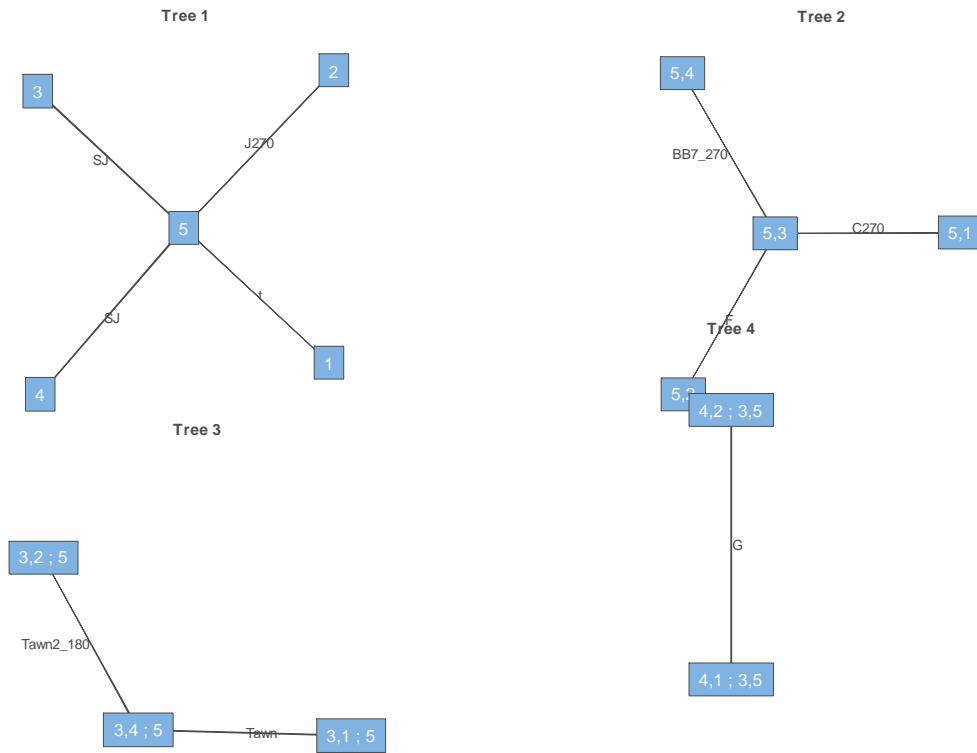


Figure 9. C Vine Copula Summary for Magnitude of Eastern Anatolian fault line (1. Elazığ, 2. Malatya, 3. Kahramanmaraş, 4. Adıyaman, 5. Sırnak)

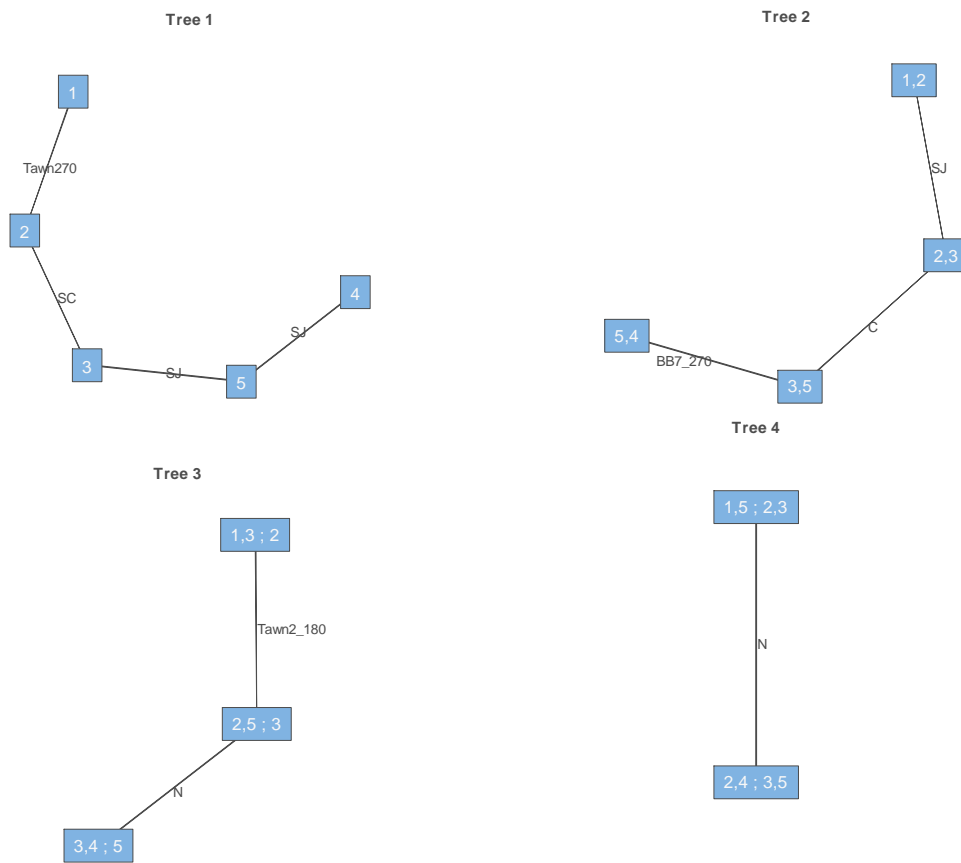


Figure 10. D Vine Copula Summary for Magnitude of Eastern Anatolian fault line (1. Elazığ, 2. Malatya, 3. Kahramanmaraş, 4. Adıyaman, 5. Sırtak)

Acknowledgments

Thank you to the Kandilli Observatory and Earthquake Research Institute and Turkey's Interior Ministry Disaster and Emergency Management Presidency for our data set.

References

- [1] Sriboonchitta, S., & Chaiboonsri, C. 2013. The dynamics Co-movement toward among capital markets in ASEAN exchanges: CD Vine Copula approach. *Procedia Economics and Finance*, 5, 696-702.
- [2] Chaiboonsri, C., & Singvejsakul, J. 2017. The Dynamics Co-

- Movement toward and the Pattern of Relation among Stock Market in World Exchanges during the Period 2000~ 2016: CD vine Copula Approach. *International Journal of Intelligent Technologies & Applied Statistics*, 10(2).
- [3] Hikmah, I. R., Saefuddin, A., & Mangku, I. 2017. Identification of Dependent Structure and Prediction of Composite Stock Price Index with CD Vine Copula Approach. *International Journal of Scientific & Engineering Research*, 7, 249-252.
- [4] Schepsmeier, U., & Brechmann, E. C. 2013. Modeling dependence with C-and D-vine copulas: The R package CD vine. *J. Stat. Software*, 52(3), 1-27.
- [5] Chokethaworn, K., Chaitip, P., Sriwichailamphan, T., & Chaiboonsri, C. 2013. The Dependence Structure and Co-movement toward between Thai's Currency and Malaysian's Currency: Markov Switching Model in Dynamic Copula Approach (MSDC). *Procedia Economics and Finance*, 5, 152-161.
- [6] Evkaya, Ö. O. 2018. Mixture of vines for dependence modeling: Finite mixture and CD-vine approaches with applications.
- [7] Karakas, A., Demir, A., Çalik, S. 2019. Interdependence of Bitcoin and Other Crypto Money Indicators: Cd Vine Copula Approach. *Bitlis Eren Üniversitesi Fen Bilimleri Dergisi*, 9(4), 1527-1536.
- [8] Kim, D., Kim, J.-M., Liao, S.-M., and Jung, Y.-S., 2013. Mixture of d-vine copulas for modeling dependence. *Computational Statistics and Data Analysis*, 64(C):1-19.
- [9] Yan, J. 2007. Enjoy the joy of copulas: with a package copula. *Journal of Statistical Software*, 21(4), 1-21.
- [10] Pourkhanali, A., Kim, J. M., Tafakori, L., Fard, F. A. (2016). Measuring systemic risk using vine copula. *Economic modelling*, 53, 63-74.
- [11] Nguyen-Huy, T., Deo, R. C., Mushtaq, S., An-Vo, D. A., & Khan, S. 2018. Modeling the joint influence of multiple synoptic-scale, climate mode indices on Australian wheat yield using a vine copula-based approach. *European journal of agronomy*, 98, 65-81.
- [12] İnç, M., Korpınar, Z. S., Al Qurashi, M. M., & Baleanu, D. 2016. A new method for approximate solutions of some nonlinear equations: Residual power series method. *Advances in Mechanical Engineering*, 8(4), 1687814016644580.
- [13] Acay, B., Inc, M. 2020. Fractional modeling of temperature dynamics of a building with singular kernels. *Chaos, Solitons & Fractals*, 110482.
- [14] Houwe, A., Inc, M., Doka, S. Y., Acay, B., & Hoan, L. V. C. 2020. The discrete tanh method for solving the nonlinear differential-difference equations. *International Journal of Modern Physics B*, 34(19), 2050177.
- [15] Akinlar, M. A., Inc, M., Gómez-Aguilar, J. F., & Boutarfa, B. 2020. Solutions of a disease model with fractional white noise. *Chaos, Solitons & Fractals*, 109840.
- [16] Akinlar, M. A., Tchier, F., Inc, M. 2020. Chaos control and solutions of fractional-order Malkus waterwheel model. *Chaos, Solitons & Fractals*, 135, 109746.
- [17] Korpınar, Z., Tchier, F., Inc, M., Bousbahi, F. T., Tawfiq, F. M., & Akinlar, M. A. 2020. Applicability of time conformable derivative to Wick-fractional-stochastic PDEs. *Alexandria Engineering Journal*.
- [18] Hashemi, M. S., Inc, M., Yusuf, A. 2020. On three-dimensional variable order time fractional chaotic system with nonsingular kernel. *Chaos, Solitons & Fractals*, 133, 109628.
- [19] Dorota K., and Roger, C., 2006, *Uncertainty Analysis with High Dimensional Dependence Modelling*. John Wiley and Sons, Ltd.

Available online at www.dergipark.gov.tr/beuscitech

Journal of Science and Technology

E-ISSN 2146-7706



Some inclusion results for the new Tribonacci-Lucas matrix

Murat KARAKAŞ^{a,*} ^a Bitlis Eren University, Department of Mathematics, TR-13000, Bitlis, Turkey

ARTICLE INFO

Article history:

Received 22 October 2021

Received in revised form 09 December 2021

Accepted 10 December 2021

Keywords:

Tribonacci-Lucas numbers

Fibonacci numbers

Toeplitz matrix

Summability method

ABSTRACT

The main purpose of this paper is first to establish a new regular matrix by using one of the important sequences of integer number called Tribonacci-Lucas. Also, we class this new Tribonacci-Lucas matrix with some well-known summability methods such as Riesz means, Nörlund means and Cesaro means. To do this, we show that the Tribonacci-Lucas matrix is a regular summability method and in addition to this, we give some inclusion results and finally prove that Cesaro matrix is stronger than the Tribonacci-Lucas matrix.

© 2021. Turkish Journal Park Academic. All rights reserved.

1. Introduction

In 1963, Tribonacci concept was introduced by Feinberg in [1]. Later, Tribonacci and Tribonacci-Lucas numbers were investigated by Catalani in [2]. These numbers must be regarded as a generalization of the well-known Fibonacci numbers. Also, the Tribonacci-Lucas numbers are members of the following general Tribonacci recurrence

$$U_{n+1} = U_n + U_{n-1} + U_{n-2}, \quad U_0 = 0, U_1 = U_2 = 1.$$

The Tribonacci-Lucas sequence is

$$(v_n) = (3, 1, 3, 7, 11, 21, 39, 71, 131, 241, \dots)$$

and it can be easily seen from the elements of the sequence (v_n) that $v_0 = 3, v_1 = 1, v_2 = 3$ and

$$v_{n+1} = v_n + v_{n-1} + v_{n-2}.$$

The following expressions for the sums of the Tribonacci and Tribonacci-Lucas numbers can be found in [3-4]:

$$\sum_{k=1}^n U_k = \frac{U_{n+2} + U_n - 1}{2},$$

$$\sum_{k=1}^n (-1)^{k-1} U_k = \frac{(-1)^{n+1} (U_{n+1} - U_{n-1}) + 1}{2},$$

$$\sum_{k=1}^n v_k = \frac{v_{n+2} + v_n - 6}{2},$$

$$\sum_{k=1}^n (-1)^{k-1} v_k = \frac{(-1)^{n+1} (v_{n+1} - v_{n-1}) + 2}{2}.$$

The sequences of integer number defined by recurrence relations have been studied by many authors in [5-10]. In these studies, authors have given Fibonacci, Lucas, Padovan and Catalan numbers and their various properties.

Let us denote the space of all real valued sequences by w and each vector subspace of w is named sequence space. We indicate the spaces of null, convergent, bounded sequences and

* Corresponding author. Tel.: +0 434 222 0020; fax: +0 434 222 9143

E-mail address: mkarakas@beu.edu.tr

ORCID :0000-0002-5174-0282(M. Karakaş)

p - absolutely convergent series by c_0, c, ℓ_∞ and $\ell_p (1 \leq p < \infty)$.

Let $s = (s_n)$ be a sequence of non-negative real numbers with $s_0 > 0$ and take $S_n = \sum_{k=0}^n s_k$ for all $n \in \mathbb{N}$. Now, we give the following some well-known examples of particular summability matrices which satisfy the Toeplitz conditions.

Definition 1.1. The Riesz means according to the sequence $s = (s_n)$ is defined by the following matrix for all $n, k \in \mathbb{N}$:

$$a_{nk} = \begin{cases} \frac{s_k}{S_n}, & 0 \leq k \leq n \\ 0, & k > n \end{cases}.$$

Riesz mean (R, s) is also stated for a sequence (x_n) as follows:

$$s_n = \frac{s_1 x_1 + s_2 x_2 + \dots + s_n x_n}{S_n} \quad [11].$$

Definition 1.2. The Nörlund means according to the sequence $s = (s_n)$ is defined by the following matrix for all $n, k \in \mathbb{N}$:

$$\tilde{a}_{nk} = \begin{cases} \frac{s_{n-k+1}}{S_n}, & k \leq n \\ 0, & k > n \end{cases}.$$

Nörlund mean (N, s) is also stated for a sequence (x_n) as follows:

$$\tilde{s}_n = \frac{s_n x_1 + s_{n-1} x_2 + \dots + s_1 x_n}{S_n} \quad [11].$$

The transformation (R, s) is regular if $S_n \rightarrow \infty (n \rightarrow \infty)$ and (N, s) is regular if $s_n / S_n \rightarrow 0 (n \rightarrow \infty)$ [12]. Also, both the Riesz and the Nörlund means are reduced to the following Cesaro mean $(C, 1)$ in the case $s_n = 1$ for all n :

$$C_{nk} = \begin{cases} \frac{1}{n}, & k \leq n \\ 0, & k > n \end{cases}.$$

Definition 1.3. Let (λ_n) be a strictly increasing sequence of positive integers. For a sequence (x_n) , C_λ -transformation is defined as follows:

$$s_n = \frac{x_1 + x_2 + \dots + x_{\lambda_n}}{\lambda_n} \quad [13].$$

Definition 1.4. The matrix $B = (B_{m,n})$ is a (M) matrix if B is triangular and

$$\left| \sum_{k=1}^n b_{m,k} x_k \right| \leq T \left| \sum_{k=1}^{n'} b_{n',k} x_k \right|$$

for some $n', n' = n'(n) (0 \leq n' \leq n), (n = 1, 2, 3, \dots)$ and for all $m (m \geq n)$ [11]. Herein, n' is interdependent n and $\{x_n\}$ but it is independent of m . Also, the class (M) isn't confined to the regular matrices.

If $k < n+1$ for the matrix $(C, 1)$, then we have $\frac{1}{n+1} \sum_{m=0}^k t_m \leq \frac{1}{k+1} \sum_{m=0}^k t_m$ and so the matrix $(C, 1)$ is a (M) matrix [11].

Theorem 1.5. Let $A = (a_{m,n})$ and $B = (b_{m,n})$ be regular triangular matrices and A be a (M) matrix. Therefore, if

$$\sum_{n=1}^m \left| \frac{b_{m,n}}{a_{m,n}} - \frac{b_{m,n+1}}{a_{m,n+1}} \right| < K,$$

from which it is concluded that B is stronger than A [11].

Theorem 1.6. The matrix $A = (a_{m,n})$ is (M) matrix if it is triangular and holds the following conditions:

$$a_{m,k} = 0, 0 \leq \frac{a_{m,k}}{a_{n,k}} \leq T (0 \leq k \leq n \leq m) \quad (1)$$

and

$$\frac{a_{m,k}}{a_{n,k}} \geq \frac{a_{m,k+1}}{a_{n,k+1}} (0 \leq k \leq n \leq m) \quad (2)$$

2. Inclusion results for the Tribonacci-Lucas matrix

In this part of the paper, we are first going to introduce a new Tribonacci-Lucas matrix. Then, we give some relations and inclusion results between the matrix $V = (v_{nk})$ and some well-known summability matrices by comparing them.

Now, let us define our new Tribonacci-Lucas matrix as follows:

$$V = (v_{nk}) = \begin{cases} \frac{2v_k}{v_{n+2} + v_n - 6}, & 1 \leq k \leq n \\ 0, & k > n \end{cases} \quad (3)$$

If we write the terms of this matrix, then we have

$$V = \begin{bmatrix} \frac{2v_1}{v_3 + v_1 - 6} & 0 & 0 & 0 & \dots \\ \frac{2v_1}{v_4 + v_2 - 6} & \frac{2v_2}{v_4 + v_2 - 6} & 0 & 0 & \dots \\ \frac{2v_1}{v_5 + v_3 - 6} & \frac{2v_2}{v_5 + v_3 - 6} & \frac{2v_3}{v_5 + v_3 - 6} & 0 & \dots \\ \frac{2v_1}{v_6 + v_4 - 6} & \frac{2v_2}{v_6 + v_4 - 6} & \frac{2v_3}{v_6 + v_4 - 6} & \frac{2v_4}{v_6 + v_4 - 6} & \dots \\ \vdots & \vdots & \vdots & \vdots & \ddots \end{bmatrix}$$

and so,

$$V = \begin{bmatrix} 1 & 0 & 0 & 0 & \dots \\ \frac{1}{4} & \frac{3}{4} & 0 & 0 & \dots \\ \frac{1}{11} & \frac{3}{11} & \frac{7}{11} & 0 & \dots \\ \frac{1}{22} & \frac{3}{22} & \frac{7}{22} & \frac{11}{22} & \dots \\ \vdots & \vdots & \vdots & \vdots & \ddots \end{bmatrix}.$$

It can be clearly seen from above that the Tribonacci-Lucas matrix is triangular.

Now, let us define the following real valued sequence $y = (y_n)$ which is named V – transform of a sequence $x = (x_n)$ for all $n \in \mathbb{N}$:

$$y_n = V(x_n) = \frac{2}{v_{n+2} + v_n - 6} \sum_{k=1}^n v_k \tag{4}$$

First, we are going to give the definition of V – convergence in defiance of F – convergence in [14].

Definition 2.1. If $(V(x_n - l)) \rightarrow 0$ for $n \in \mathbb{N}$ and $l \in \mathbb{R}$, then a real valued sequence $x = (x_n)$ is named V – convergent to l .

Theorem 2.2. The Tribonacci-Lucas matrix $V = (v_{nk})$ is a regular summability method $\Leftrightarrow v_{n+2} + v_n - 6 \rightarrow \infty$ as $n \rightarrow \infty$.

Proof. Let $V = (v_{nk})$ be a regular summability method. Then,

$$\lim_{n \rightarrow \infty} v_{nk} = \lim_{n \rightarrow \infty} \frac{2v_k}{v_{n+2} + v_n - 6} = 0 \text{ from Silverman-Toeplitz theorem}$$

in [8]. Thus, $v_{n+2} + v_n - 6 \rightarrow \infty, n \rightarrow \infty$. Now contrarily, assume that $v_{n+2} + v_n - 6 \rightarrow \infty$ as $n \rightarrow \infty$. Therefore,

$$\sum_{k=1}^{\infty} \frac{2v_k}{v_{n+2} + v_n - 6} = \sum_{k=1}^n \frac{2v_k}{v_{n+2} + v_n - 6} = 1 \quad \text{and} \quad \text{also,}$$

$$\lim_{n \rightarrow \infty} v_{nk} = \lim_{n \rightarrow \infty} \frac{2v_k}{v_{n+2} + v_n - 6} = 0$$

and

$$\lim_{n \rightarrow \infty} \sum_{k=1}^{\infty} v_{nk} = \lim_{n \rightarrow \infty} \sum_{k=1}^n v_{nk} = \lim_{n \rightarrow \infty} \sum_{k=1}^n \frac{2v_k}{v_{n+2} + v_n - 6} = 1.$$

In that case, the Tribonacci-Lucas matrix V is a regular summability method.

Theorem 2.3. The Tribonacci-Lucas matrix $V = (v_{nk})$ is a (M) matrix.

Proof. Since the inequalities

$$0 \leq \frac{2v_k}{v_{m+2} + v_m - 6} \cdot \frac{v_{n+2} + v_n - 6}{2v_k} = \frac{v_{n+2} + v_n - 6}{v_{m+2} + v_m - 6} \leq \frac{v_{n+2}}{v_{m+2}} \leq 1$$

and

$$\begin{aligned} \frac{2v_{k+1}}{v_{m+2} + v_m - 6} &= \frac{v_{n+2} + v_n - 6}{v_{m+2} + v_m - 6} \leq \frac{v_{n+2} + v_n - 6}{v_{m+2} + v_m - 6} \cdot \frac{2v_k}{2v_k} \\ &= \frac{2v_k}{v_{m+2} + v_m - 6} \cdot \frac{v_{n+2} + v_n - 6}{2v_k} \end{aligned}$$

hold, the Tribonacci-Lucas matrix V is (M) matrix.

Definition 2.4. Let $x = (x_n)$ and $y = (y_n)$ be two real valued sequences. Then, if there are two positive real numbers t and T such that the inequality $t.x_n \leq y_n \leq T.x_n$ holds for all $n \in \mathbb{N}$, they are named equivalent.

Now, let us give the relation between V and (R,s) :

Theorem 2.5. Let $V = (v_{nk})$ be a Tribonacci-Lucas matrix and $x = (x_n)$ be a real valued sequence. Then, $x_n \rightarrow I(V) \Leftrightarrow x_n \rightarrow I(R,s)$ for any sequence (s_n) such that (s_n) and (v_n) are equivalent for all $n \in \mathbb{N}$.

Proof. Assume that $x_n \rightarrow I(V)$. In this case, we get

$$\lim_{n \rightarrow \infty} \frac{2}{v_{n+2} + v_n - 6} \sum_{k=1}^n v_k (x_k - l) = 0.$$

From here, under the supposition on (s_n) , the following inequality holds:

$$\begin{aligned} \frac{1}{S_n} \sum_{k=1}^n s_k (x_k - l) &\leq \frac{1}{S_n} \sum_{k=1}^n T.v_k (x_k - l) \\ &\leq \frac{T}{t} \frac{2}{v_{n+2} + v_n - 6} \sum_{k=1}^n v_k (x_k - l). \end{aligned} \tag{5}$$

Also, by using the similar technique, we find

$$\frac{t}{T} \frac{2}{v_{n+2} + v_n - 6} \sum_{k=1}^n v_k (x_k - l) \leq \frac{1}{S_n} \sum_{k=1}^n s_k (x_k - l). \tag{6}$$

Resulting from $x_k \rightarrow I(V)$, the inequalities (5) and (6) give us

$$\text{that } \lim_{n \rightarrow \infty} \frac{1}{S_n} \sum_{k=1}^n s_k (x_k - l) = 0.$$

The sufficient condition of this theorem can be easily shown by use of the same method. So, the proof is completed.

Theorem 2.6. Let $B = (b_{nk})$ be a regular matrix and suppose that $\sum_{k=1}^n |b_{nk} - v_{nk}| \rightarrow 0$ as $n \rightarrow \infty$. Then for any bounded sequence, $x_n \rightarrow I(B) \Leftrightarrow x_n \rightarrow I(V)$.

Proof. For any n and bounded sequence $x = (x_n)$, we have

$$\begin{aligned} |(Bx)_n - (Vx)_n| &= \left| \sum_{k=1}^n b_{nk}x_k - \sum_{k=1}^n v_{nk}x_k \right| \\ &\leq \sum_{k=1}^n |b_{nk} - v_{nk}| |x_k| \leq \|x\| \sum_{k=1}^n |b_{nk} - v_{nk}|. \end{aligned}$$

Hence, if $x_n \rightarrow l(B)$ and $x_n \rightarrow l(V)$, then we get

$$|(Vx)_n - l| \leq |(Vx)_n - (Bx)_n| + |(Bx)_n - l| \rightarrow 0, n \rightarrow \infty \tag{7}$$

and in a similar way

$$|(Bx)_n - l| \leq |(Bx)_n - (Vx)_n| + |(Vx)_n - l| \rightarrow 0, n \rightarrow \infty. \tag{8}$$

Consequently, the inequalities (7) and (8) complete the proof.

Now, we are going to establish the following associate matrix $\tilde{V} = (\tilde{v}_{nk})$:

$$\tilde{v}_{nk} = \begin{cases} \frac{2v_{n-k}}{v_{n+2} + v_n - 6}, & k \leq n \\ 0, & k > n \end{cases} \tag{9}$$

We can state the associate matrix $\tilde{V} = (\tilde{v}_{nk})$ as a Nörlund type Tribonacci-Lucas matrix when the matrix $\tilde{V} = (\tilde{v}_{nk})$ can be written as a Riesz type Tribonacci-Lucas matrix. Accordingly, we first give the following lemma which will be used in the next theorems.

Lemma 2.7. The series $\sum_{n=1}^{\infty} s_n x^{n-1}$ and $\sum_{n=1}^{\infty} S_n x^{n-1}$ are convergent for all x where $|x| < 1$, if (N, s_n) is a regular Nörlund matrix.

This lemma is also suitable for the matrix $\tilde{V} = (\tilde{v}_{nk})$ just because the matrix $\tilde{V} = (\tilde{v}_{nk})$ is a Nörlund type matrix. In the continuation of this study, we can use V_n in place of \tilde{V}_n having regard to the definition of $\tilde{V} = (\tilde{v}_{nk})$.

Remark 2.8. Due to the fact that the series $v(x) = \sum_{n=1}^{\infty} v_n x^{n-1}$

and $V(x) = \sum_{n=1}^{\infty} V_n x^{n-1}$ are convergent for all $|x| < 1$, the series below are also convergent:

$$q(x) = \frac{s(x)}{v(x)} = \frac{S(x)}{V(x)}, \quad q(x) = \sum_{n=1}^{\infty} q_n x^{n-1},$$

$$r(x) = \frac{v(x)}{s(x)} = \frac{V(x)}{S(x)}, \quad r(x) = \sum_{n=1}^{\infty} r_n x^{n-1}.$$

Theorem 2.9. $(N, s_n) \subseteq (\tilde{V})$ if and only if there is $T > 0$ such that for every n $|q_1|S_n + |q_2|S_{n-1} + \dots + |q_n|S_1 \leq T.V_n$ and

$$\lim_{n \rightarrow \infty} \frac{q_n}{V_n} = 0.$$

Proof. Let (k_n) and (h_n) be the (N, s) - transformation and (\tilde{v}) - transformation of a real valued sequence (p_n) . Then, we get

$$\begin{aligned} \sum_{n=1}^{\infty} V_n h_n x^{n-1} &= \sum_{n=1}^{\infty} V_n \frac{(v_n p_1 + v_{n-1} p_2 + \dots + v_1 p_n)}{V_n} x^{n-1} \\ &= (v_1 p_1) x^0 + (v_2 p_1 + v_1 p_2) x^1 + (v_3 p_1 + v_2 p_2 + v_1 p_3) x^2 + \dots \\ &\quad + (v_n p_1 + v_{n-1} p_2 + \dots + v_1 p_n) x^{n-1} + \dots \\ &= p_1 (v_1 x^0 + v_2 x^1 + v_3 x^2 + \dots) + p_2 (v_1 x + v_2 x^2 + v_3 x^3 + \dots) \\ &\quad + p_3 (v_1 x^2 + v_2 x^3 + v_3 x^4 + \dots) + \dots + p_n (v_1 x^{n-1}) + \dots \\ &= p_1 x^0 (v_1 x^0 + v_2 x^1 + v_3 x^2 + \dots + v_n x^{n-1}) + p_2 x^1 (v_1 x^0 + v_2 x^1 + v_3 x^2 + \dots + v_{n-1} x^{n-2}) \\ &\quad + \dots + p_n x^{n-1} (v_1 x^0) + \dots \\ &= \left(\sum_{n=1}^{\infty} p_n x^{n-1} \right) \left(\sum_{n=1}^{\infty} v_n x^{n-1} \right) = p(x)v(x). \end{aligned} \tag{10}$$

In a similar way, we also have

$$\sum_{n=1}^{\infty} S_n k_n x^{n-1} = p(x)s(x). \tag{11}$$

Now, from the hypothesis, we know that $v(x) = q(x)s(x)$ and $v(x)p(x) = q(x)s(x)p(x)$.

If we consider (17), (18) and the Cauchy product of series, then

we find $\sum_{n=1}^{\infty} V_n h_n x^{n-1} = \sum_{n=1}^{\infty} \sum_{m=1}^n q_{n-m+1} S_m k_m x^{n-1}$ and so for all $n \in \mathbb{N}$,

$$V_n h_n = q_n S_1 k_1 + q_{n-1} S_2 k_2 + \dots + q_1 S_n k_n. \quad \text{Thus, } h_n = \sum_{m=1}^n b_{nm} k_m \quad \text{and}$$

$$b_{nm} = \begin{cases} \frac{q_{n-m+1} S_m}{V_n}, & m \leq n \\ 0, & m > n \end{cases}. \quad \text{The matrix } b_{nm} \text{ is regular, in truth}$$

$$\lim_{n \rightarrow \infty} b_{nm} = \lim_{n \rightarrow \infty} \frac{q_{n-m+1} S_m}{V_n} = \lim_{n \rightarrow \infty} \frac{q_{n-m+1} S_m}{V_{n-m+1}} = 0,$$

$$\sum_{m=1}^{\infty} |b_{nm}| = \frac{|q_1|S_n + \dots + |q_n|S_1}{V_n} \leq T,$$

$$\lim_{n \rightarrow \infty} \sum_{m=1}^n b_{nm} = \frac{q_1 S_n + \dots + q_n S_1}{V_n} = \frac{V_n}{V_n} = 1.$$

Therefore, the proof of sufficient condition is completed. The proof of necessary condition can be done by taking advantage of the specifications in the expression of theorem.

Definition 2.10. Let $\beta = (\beta_n)$ be a strictly increasing sequence of positive integers. Let us define the V_β - transformation of a sequence $x = (x_n)$ as follows:

$$z_n = \frac{2}{v_{\beta(n)+2} + v_{\beta(n)} - 6} \sum_{k=1}^{\beta(n)} v_k x_k.$$

Little o notation, also called Landau's symbol is usually used in mathematics. Informally, $f(t) = o(g(t))$ is supposed to mean that f grows much slower than g and it is insignificant in comparison. Formally, we write $f(t) = o(g(t))$ if and only if for every $T > 0$ there exists a real number N such that for all $t > N$ we get $|f(t)| < T|g(t)|$ and if $g(t) \neq 0$, this is equivalent to $\lim_{t \rightarrow \infty} \frac{f(t)}{g(t)} = 0$.

Theorem 2.11. Let $\beta = \{\beta(n)\}$ and $\gamma = \{\gamma(n)\}$ be a strictly increasing sequences of natural number. Then, V_β is equivalent to V_γ on ℓ_∞ if $\lim_{n \rightarrow \infty} \frac{v_{\beta(n)+2} + v_{\beta(n)} - 6}{v_{\gamma(n)+2} + v_{\gamma(n)} - 6} = 1$.

Proof. Let $x = x(n)$ be a bounded sequence and $T(n) = \max\{\beta(n), \gamma(n)\}, t(n) = \min\{\beta(n), \gamma(n)\}$. Then, we have for any n

$$\begin{aligned} |(V_\beta x)_n - (V_\gamma x)_n| &= \left| \frac{2}{v_{\beta(n)+2} + v_{\beta(n)} - 6} \sum_{k=1}^{\beta(n)} v_k x_k - \frac{2}{v_{\gamma(n)+2} + v_{\gamma(n)} - 6} \sum_{k=1}^{\gamma(n)} v_k x_k \right| \\ &= \left| \frac{2}{v_{T(n)+2} + v_{T(n)} - 6} \sum_{k=1}^{T(n)} v_k x_k - \frac{2}{v_{t(n)+2} + v_{t(n)} - 6} \sum_{k=1}^{t(n)} v_k x_k \right| \\ &= \left| \frac{2}{v_{T(n)+2} + v_{T(n)} - 6} \sum_{k=1}^{t(n)} v_k x_k + \frac{2}{v_{T(n)+2} + v_{T(n)} - 6} \sum_{k=t(n)+1}^{T(n)} v_k x_k - \frac{2}{v_{t(n)+2} + v_{t(n)} - 6} \sum_{k=1}^{t(n)} v_k x_k \right| \\ &= \left| \sum_{k=1}^{t(n)} v_k x_k \left(\frac{2}{v_{T(n)+2} + v_{T(n)} - 6} - \frac{2}{v_{t(n)+2} + v_{t(n)} - 6} \right) + \frac{2}{v_{T(n)+2} + v_{T(n)} - 6} \sum_{k=t(n)+1}^{T(n)} v_k x_k \right| \\ &\leq \|x\|_\infty \left(\sum_{k=1}^{t(n)} v_k \left| \frac{2(v_{T(n)+2} + v_{t(n)} - v_{T(n)+2} - v_{T(n)})}{(v_{T(n)+2} + v_{T(n)} - 6)(v_{t(n)+2} + v_{t(n)} - 6)} \right| + \sum_{k=t(n)+1}^{T(n)} v_k \left| \frac{2}{v_{T(n)+2} + v_{T(n)} - 6} \right| \right) \\ &\leq \|x\|_\infty \left(\frac{(v_{T(n)+2} + v_{t(n)} - v_{T(n)+2} - v_{T(n)})(v_{t(n)+2} + v_{t(n)} - 6) + v_{T(n)+2} + v_{T(n)} - v_{t(n)+2} - v_{t(n)}}{(v_{T(n)+2} + v_{T(n)} - 6)(v_{t(n)+2} + v_{t(n)} - 6)} + \frac{v_{T(n)+2} + v_{T(n)} - v_{t(n)+2} - v_{t(n)}}{v_{T(n)+2} + v_{T(n)} - 6} \right) \\ &\leq 2 \|x\|_\infty \left(\frac{(v_{T(n)+2} + v_{T(n)} - 6) - (v_{t(n)+2} + v_{t(n)} - 6)}{v_{T(n)+2} + v_{T(n)} - 6} \right) \\ &\leq 2 \|x\|_\infty \left(1 - \frac{v_{t(n)+2} + v_{t(n)} - 6}{v_{T(n)+2} + v_{T(n)} - 6} \right) = o(1) \end{aligned}$$

since $\lim_{n \rightarrow \infty} \frac{v_{\beta(n)+2} + v_{\beta(n)} - 6}{v_{\gamma(n)+2} + v_{\gamma(n)} - 6} = 1$ and $\lim_{n \rightarrow \infty} \frac{v_{t(n)+2} + v_{t(n)} - 6}{v_{T(n)+2} + v_{T(n)} - 6} = 1$.

Therefore, if x is V_β -summable to L , then we obtain

$$0 \leq |(V_\gamma x)_n - L| \leq |(V_\gamma x)_n - (V_\beta x)_n| + |(V_\beta x)_n - L| = o(1) + o(1) = o(1)$$

and in a similar way, if x is V_γ -summable to L , then we obtain

$$0 \leq |(V_\beta x)_n - L| \leq |(V_\beta x)_n - (V_\gamma x)_n| + |(V_\gamma x)_n - L| = o(1) + o(1) = o(1).$$

Theorem 2.12. Cesaro matrix C_{nk} is stronger than Tribonacci-Lucas matrix $V = (v_{nk})$.

Proof. From Theorem 1.5, if we take $B = V$ (Tribonacci-Lucas matrix) and $A = C$ (Cesaro matrix), then we find

$$\begin{aligned} \sum_{k=1}^n \left| \frac{2nv_k}{v_{n+2} + v_n - 6} - \frac{2nv_{k+1}}{v_{n+2} + v_n - 6} \right| &= \sum_{k=1}^n \frac{2n}{v_{n+2} + v_n - 6} (v_k - v_{k+1}) \\ &= \frac{2n}{v_{n+2} + v_n - 6} \sum_{k=1}^n (v_k - v_{k+1}). \end{aligned}$$

Since the inequality $2n \leq v_{n+2} + v_n - 6$ holds for all $n \in \mathbb{N}$, we have

$$\begin{aligned} \frac{2n}{v_{n+2} + v_n - 6} \sum_{k=1}^n (v_k - v_{k+1}) &\leq \frac{v_{n+2} + v_n - 6}{v_{n+2} + v_n - 6} \sum_{k=1}^n (v_k - v_{k+1}) \\ &\leq v_1 - v_2 + v_2 - v_3 + v_3 - v_4 + \dots + v_n - v_{n+1} \leq 1 - v_{n+1} < 1. \end{aligned}$$

Consequently, we obtain $V \subset C$ and the proof is completed.

In general, the converse of this theorem is not true. Indeed, for the sequence $x_n = \frac{(-1)^n}{n}$, $(C_n x) = \frac{1}{n} \sum_{k=1}^n \frac{(-1)^k}{k}$ is convergent but the V -transformation of (x_n) , that is

$$(V_n x) = \frac{2}{v_{n+2} + v_n - 6} \sum_{k=1}^n v_k \frac{(-1)^k}{k}$$

is not convergent.

3. Summary and Conclusions

In our study, a new regular matrix was first defined by using the well-known sequence of integer number called Tribonacci-Lucas. Then, we compared the Tribonacci-Lucas matrix with the other summability matrices such as Nörlund mean, Riesz mean and Cesaro mean and also investigated the relation between these matrices. Since the matrix $V = (v_{nk})$ is regular, the sequence $(V_n x)$ is convergent for a sequence (x_n) . So, for the matrix $V = (v_{nk})$, both statistical convergence and the studies with regular matrices can be investigated.

References

- [1] Feinberg, M., 1963. Fibonacci-Tribonacci. The Fibonacci Quarterly, 1 (3), 70-74.
- [2] Catalani, M., 2002. Identities for Tribonacci-related Sequences, Cornell University Library, arXiv:0209179.
- [3] Frontczak, R., 2018. Sums of Tribonacci and Tribonacci-Lucas Numbers, International Journal of Mathematical Analysis, 12 (1), 19-24.
- [4] Kılıç, E., 2008. Tribonacci Sequences with Certain Indices and Their Sums, Ars Combinatoria, 86, 13-22.
- [5] Kara, E.E., and Başarır, M., 2012. An Application of Fibonacci Numbers into Infinite Toeplitz Matrices, Caspian Journal of Mathematical Sciences, 1 (1), 43-47.
- [6] Karakaş, M., and Karakaş, A.M., 2017. New Banach Sequence Spaces That is Defined By The Aid of Lucas

- Numbers, İğdır University Journal of the Institute of Science and Technology, 7 (4), 103-111.
- [7] Karakaş, M., and Karakaş, A.M., 2018. A Study on Lucas Difference Sequence Spaces $l_p(\hat{E}(r,s))$ and $l_\infty(\hat{E}(r,s))$, Maejo International Journal of Science and Technology, 12 (1), 70-78.
- [8] Yaying, T., Hazarika, B., and Mohiuddine, S.A., 2021. On Difference Sequence Spaces of Fractional Order Involving Padovan Numbers, Asian-European Journal of Mathematics, 14 (6), 1-24.
- [9] Yaying, T., and Hazarika, B., 2020. On Sequence Spaces Defined by the Domain of a Regular Tribonacci Matrix, Mathematica Slovaca, 70 (3), 697-706.
- [10] Ercan, S., and Bektaş, Ç., 2017. Some Topological and Geometric Properties of a New BK-space Derived by Using Regular Matrix of Fibonacci Numbers, Linear and Multilinear Algebra, 65 (5), 909-921.
- [11] Petersen, G.M., 1966. Regular Matrix Transformations. McGraw Hill Publishing Company Limited.
- [12] Başar, F., 2011. Summability Theory and Its Applications. Bentham Science Publishers.
- [13] Armitage, D.H., and Maddox, I.J., 1989. A New Type of Cesaro Mean, Analysis, 9, 195-204.
- [14] Küçükaslan, M., and Aris, B., 2019. Sequence Spaces Defined by Fibonacci Matrix, General Letters in Mathematics, 6 (2), 45-60.

Available online at www.dergipark.gov.tr/beuscitech

Journal of Science and Technology

E-ISSN 2146-7706



The Possible External Factor Effecting On NO₂ Molecule During Lightning Flash Under Corona Discharge

Ezman KARABULUT^{a,*} ^a Bitlis Eren University, Vocational School of Health Services, 13000, Bitlis, Turkey

ARTICLE INFO

Article history:

Received 26 October 2021

Received in revised form 03 November 2021

Accepted 01 December 2021

Keywords:

Corona discharge

Lightning Flash

Electric Field

NO₂ molecule

Cloud

ABSTRACT

The focus in this study is on the formation of the NO₂ molecule on the O+NO system, which is the atom-atom reaction that occurs the most according to the molecular concentrations formed as a result of lightning flashes. In this study, it was mentioned that another external effect that affects NO₂ molecule concentrations, other than temperature and visible electromagnetic radiation, is the electric field. This will suppress the formation of O₂ at high temperatures and the formation of NO concentration at low temperature, as it increases the barrier in the product channel on the reaction pathway and NO+O recombination in the reactant channel under favorable conditions. Under these two conditions, the NO₂ population might be supported by electric field

© 2021. Turkish Journal Park Academic. All rights reserved.

1. Introduction

Troposphere is an atmospheric layer in which the activity of anthropogenic and greenhouse gases is high (C, Cl, F etc.), and where water molecules are important for all living activity in the world. This layer has a height of approximately 18 km from the ground in the equator, but extends up to 5 km at the poles. Within this layer, many reactions can take place by means of reactive scattering, recombination, and photo-dissociation. Apart from human activity and sunlight, another reaction medium in this layer is the lightning flash, which provides rapid combustion and cooling environment. Lightning is a natural radioactive source with its fusion and fission reactions at high temperature (Levine, 1995). To nearly a height of clouds from the ground surface, the concentrations of O₂ and N₂ molecules are about 99% when compared to other molecules. For this reason, NO molecule shows the most formation with atomization of these molecules in the air environment as a result of electron discharge. Other molecules formed rather than this molecule are respectively, from large ones toward small ones according to their concentration

density, listed as NO₂, HONO, N₂O, H₂O₂, HO₂, CO. The change in the number of NO molecules is proportional to the electron flux per lightning flash. Lightning is redirected to the earth from cloud, to cloud from the earth and cloud from cloud. However, this is not a factor affecting the formation of molecules. It only affects concentration. Another factor affecting the molecular density of NO is the electric field in the environment, also known as a parameter that initializes lightning. The electric field is predominantly vertical between the cloud and the earth's surface and is continually active before, after and during the flash. With flash, magnitude of the electric field changes in the degree of kV/m. It varies in the range of 25-100kV/m in size (Rakov and Uman, 2003). The minimum stretch of electric field to start lightning is around a few kV/m. In addition, width of the electric field can be up to range of several km [Jacobson and Streets, 2009; Coleman et al., 2003]. In the open and clean air, the electric field power is 20-30 V/m and in the lightning-free cloudy environments it is around 800 V/m (Larossi et al., 2011). Unlike the above mentioned electric fields, in positive and negative Corona discharge events, it can occur under high electric field, from 10⁶ to 10⁸ V/m (1 a.u. = 5.14x10¹¹ V/m) (Riba et al., 2018; Bazelyan et al., 2008;

* Corresponding author. Tel.: +0 434 222 00 20

E-mail address: ezman.fizik@gmail.com

ORCID : 0000-0003-4806-8576 (E. Karabulut)

Kherbouche et al., 2016; MacGorman and Rust, 1998). If assuming that there are no greenhouse gases (H_2O , CO_2 , O_3 , N_2O , CH_4 and NO_2 , formed as a result of combustion reaction and of human activity) in lightning flash, and that lightning occurs in dry weather (no rain), NO (nitrogen oxide) and NO_2 (nitrogen dioxide) are the most two concentrated gases in the environment (Salonen et al., 2019; Smirnov and Marapulets, 2012). In fact, when considering the concentrations of trace gases such as H_2O and CO_2 at the temperature considered, they have no effect on the formation of gases such as NO and NO_2 . Typical hurricane produces $2\text{-}40 \times 10^{25}$ molecules of NO per flash (Schumann and Huntrieser, 2007). NO is known as short-lived trace gases and can be converted to stable free radical NO_2 by $\text{NO} + \text{O}$ reaction (Lagzi et al., 2013). Since the concentrations of greenhouse gases in the environment are relatively low, the effect of X-ray, Gamma rays and free electrons in the reaction medium known as the center of lightning, which can reach temperatures up to 40000 K, is more effective on the NO_2 molecule. $\text{NO}_2 + hc/\mu$ ($\mu < 420$ nm) can be re-separated into $\text{NO} + \text{O}$ by depending on lifetime of the excited complex (Michalski et al., 2004; Grebenshchikov et al., 1999; Ivanov et al., 2007). In addition, under the influence of lightning in the environment, interaction of cold environment O_2 molecules with the dissociated hot O atoms can form O_3 and this molecule is a strong radical which is prone to reaction (Franzblau and Popp, 1989). The presence of trace gases in the environment, such as water vapor, makes the formation of nitrogen oxides HNO_2 (nitrous acid) and HNO_3 (nitric acid) more efficient (Tuck, 1976). Since a number of chain reactions caused by charge discharges in the air environment in the mixture of nitrogen and oxygen affect each other's intensities, they support different formations (Fedotov and EYa, 2015). Thus, the NO molecule decreases over time. Lightning system was tried to be done in the laboratory by Hill et al. (1980). The production of NO and NO_2 was attempted to be detected with mixed of heated air by lightning and surrounding air molecules (air cooling channel). Two important ions between 3000-10000 K are e^- (electron) and NO^+ . $\text{NO}^+ e^- \rightarrow \text{N} + \text{O}$ reaction has reaction rate constant of $10^{-7} \text{ cm}^3/\text{s}$. Lightning is a heating system that can affect the area of 20 cm from the surface of the main electron flow line. At the same time, it emits heat in the shape of a shock wave. Therefore, if considered the ambient temperature to be 200-300 K and the ambient pressure below about 1 atm, an effective reaction medium is formed up to 9 cm from the main energy line. Temperature varies at every point in order of microseconds. In other words, the environment first goes into the process of heating and then cooling. Kunova and Nagnibeda (2017) showed that the rate constant of the $\text{NO} + \text{O} \rightarrow \text{N} + \text{O}_2$ reaction is $1.56 \times 10^9 \cdot T \cdot \exp(-19450 / T)$ in simulation of the gaseous molecular reaction. They also achieved experimentally the highest NO concentration at 4000 K and examined $\text{N}_2 + \text{O} \rightarrow \text{NO} + \text{N}$ and $\text{O}_2 + \text{N} \rightarrow \text{NO} + \text{O}$ reactions according to vibrational quantum numbers of product and reactant molecular. In the work is seen that the increased vibration energy of the reactant molecule causes the product molecule in high vibration quantum states. At the program designed under shock wave was used in non-equilibrium air environment. It

has been observed that the shock has dropped from 12000K to 8000K temperature up to 0.5 cm from the center. It has also been observed that ambient temperature decreases linearly from 8000 to 6500K from 0.5 cm to 3.5 cm distance. This temperature change has also effected on the concentration of molecules and atoms in the environment. As seen in that work, while number of O and N atoms increase up to 0.5 cm, NO molecules increase at the same rate and at the same range. From 0.5 cm to 3.5 cm the increase rate in O and N atoms is less while NO and O_2 molecules start to decrease. NO formed in the range of 0-0.5 cm start to decrease by means of reacting with O atom in the range of 0.5 and 3.5 cm. Thus NO_2 which has the second highest concentration in the medium starts to form. Thus the current process constitutes the $\text{NO} + \text{O}$ reaction from the reactant channel to the transition state region. In order to form the system as $\text{N} + \text{O}_2$, it needs to receive external energy. UV radiation generated by high electric current, which continues in milliseconds, can affect the molecular system created by the shock wave occurring in microseconds. Such a system takes place under appropriate temperature, electric field and ro-vibration energies.

The aim of this study is to investigate the NO_2 that occurs during lightning flashing under an electric field which is an effective factor in the corona discharge event. To do this, after optimizing the system in all minimum and transition state regions along the reaction path, it is necessary to re-optimize by applying electric fields in three dimension. In regions showing the most effective change, a new total electronic energy is determined. Thus, a new fit function that defines the energy difference in those regions is needed. When this is applied, the system acts as if it were under a constant electric field.

2. Computational Details and Approaches

The present calculations are performed on DFT-B3LYP function with aug-cc-pvTZ, basis set in doublet spin in Gaussian09 (Frisch et al., 2009). The potential energy surface (in Sayos et al. (2002)) used by modifying in this work is based on CASPT2 (17,12) G2/aug-cc-pvTZ. The Table 1 shows the equilibrium bond distances and total energies of the related region for both works. The molecular system is kept under an electric field of 10^8 V/m in these regions. This value of used electric field is the maximum electric field value observed between the clouds and the earth surface in the Corona discharge event. The transition state and minimum energy zones in the Table 1 have been recalculated under the electric field with the base function in present calculations. In the calculations, the effects of electric field in three dimensions are examined. As a result, under such a high electric field, the total energy has only changed in the TS-1 and Min-1 regions. The other regions are exposed 100 times more to electric field just to see how far it can go. But their total energies have no an effective change. The changes related to corona discharge are shown in detail in both Table 1 and the following reaction path graph (Figure 1).

There is no a serious inconsistency between the basis function used in Sayos et al. (2002) and basis function used to show the effect of electric field in the present work. The meaning of the most effective change mentioned in the title is to determine the maximum affected direction under the maximum electric field. That is, the maximum change in the electric field applied in Ts-1 is shown in the x-direction and one in Min-1 is achieved in the y-direction. Figure 1 shows the differences in total energy between ordinary lightning flash and corona discharge event. To apply the energy changes obtained by basing on another potential function to the potential energy surface in Sayos et al. (2002) causes a small amount of error. However, differences in these potential and distances among atoms are not very effective at the related areas. Other regions are not affected much in any way under the electric field although this is not mentioned in detail. Because the energy differences under the electric field in these regions are in the order of 10^{-4} eV. Therefore, it is not taken into account.

Figure 1. The reaction path of $O+NO \rightarrow N+O_2$ Reaction. Reactant asymptote is referenced to 0 au. Note that the energy values in Table 1 are not referenced to zero.

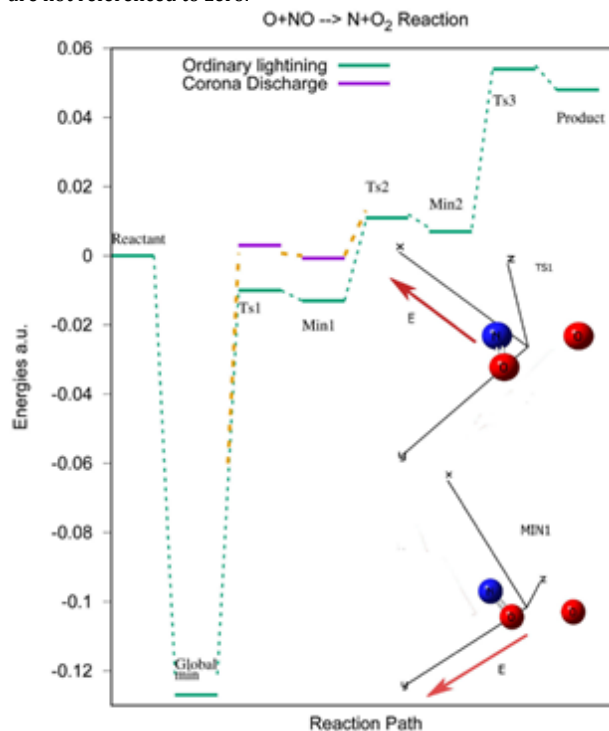


Table 1. Equilibrium bond distances and total energies belonging to transition state and minimum energy points on $O+NO \rightarrow N+O_2$ reaction system. The calculated values in Sayos et al. (2002) are indicated by the upper index "a". Energies are atomic units and distances are angstrom. O_2 is the coming atom, E.F is the case applied of electric field and E is total energy of system.

Regions	$R_e(NO_2)^a$	$R_e(NO_2)$	$R_e(O_1O_2)^a$	$R_e(O_1O_2)$	$\langle NO_2O_1^a \rangle$	$\langle NO_2O_1 \rangle$	E^a	E
Global Min	1.218	1.191	-----	-----	-----	-----	-0.1731	-0.1760
Ts-1	1.151	1.125	2.007	2.293	88.4	89.76	-0.0545	-0.0586
TS-1-E.F	-----	1.103	-----	1.934	-----	87.32	-----	-0.0028
Min-1	1.168	1.125	1.966	2.186	116.98	118.11	-0.0599	-0.0613
Min-1-E.F	-----	1.126	-----	2.188	-----	118.02	-----	-0.0082
TS-2	1.202	1.132	1.475	1.557	125.81	131.78	-0.043	-0.037
Min-2	1.241	1.194	1.338	1.358	121.7	124.83	-0.0454	-0.0405
TS-3	1.901	1.864	1.233	1.220	109.06	114.18	0.0109	0.0061

Another neglected point is the reactant minimum. The reactant minimum could be optimized under the electric field applied in the direction of $O \cdots O-N$ atomic distribution. There was no effective change in such a situation. However, if an electric field is applied in a direction perpendicular to this direction, the reactant minimum cannot be optimized and tends to form a global minimum. That is, the electric field for the reactant minimum is parallel to the $O \cdots O-N$ distribution. This case is a limitation for the global approach. As a result, under an electric field of 10^8 V / m, Ts-1 shows the most effective change with an increase of 0.37 eV, and secondly by 0.33 eV, Min-1 changes. Others have been neglected with a

change of 10^{-4} eV as mentioned above. The final shape of the potential energy surface was fit using the difference polynomial in the Mathematica 12.0 program (Wolfram Research, Inc., (2019)). This difference polynomial as a function of the distances between atoms is $\Delta V = 0.416678 - 0.0143469 * RO_2N - 0.13848 * RO_1O_2 - 0.0813487 * RO_1N$. Here distances between atoms are unit of Angstrom and are defined as $1.60 \leq RO_2N \leq 2.69$, $1.55 \leq RO_1O_2 \leq 2.15$ and $1.15 \leq RO_1N \leq 2.20$. These values start from a point that is close to the global minimum region and continue up to Ts-2. Energy changes in the global minimum and Ts-2 regions is considered as 0. They act as the node point for the exchange

polynomial. To take a picture of potential energy surface in 3 dimensions, it should be showed in the geometry that indicates the most effective change. This region is between Ts-1 and Min-1 as seen Figure1. The factor that facilitates to polynomial fit between these two regions is that the distance between O_1 and N changes effectively. As seen in Table 1, the distances between atoms do not change much, while the angle is more variable. This angle on the O_2 atom (the atom transferred from N atom to O_1 atom) in the system varies between 20-27 degrees. The change of 3-dimensional potential energy at approximately 25 degrees is seen in Figure 2.

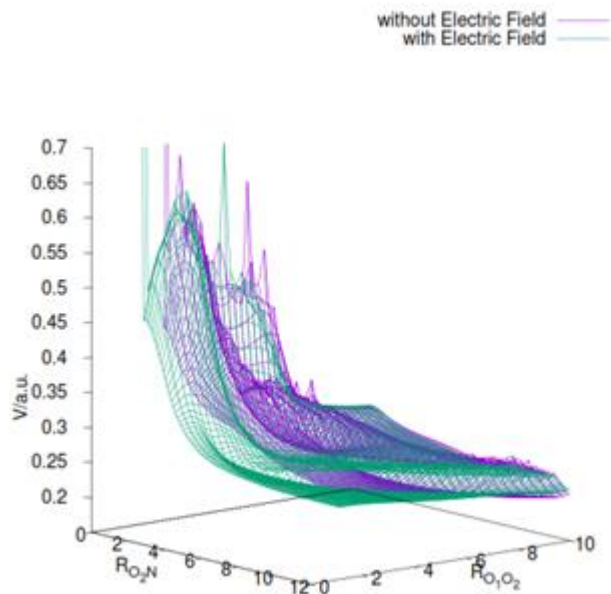


Figure 2. Potential energy surface at approximately 25 degrees in 3 dimensions with and without electric field. Here distances between atoms is unit of atomic.

The potential energy surface region that is fit is a very small surface once compared to the global surface. The fact that the atomic distance between Ts-1 and Min-1 does not change very effectively (except for the change of distance between O_1 -N) made it easier to make fit. Another simplicity is that it does not require a very detailed convergence test in time propagation.

3. Conclusions

The focus was on the formation of the NO_2 molecule on the $O+NO$ system, which is the atom-diatom reaction that occurs the most according to the molecular concentrations formed as a result of lightning flashes. In this study, it was mentioned that another external effect that affects NO_2 molecule concentrations, other than temperature and visible electromagnetic radiation, is the electric field. It was observed that the electric field in question affected only two transition regions (Ts-1 and Min-1) on the $O+NO \rightarrow N+O_2$ reaction system. It also increased the barrier energy by increasing the

total energy in these regions. In such increased barrier reactions, the reaction rate slows down. So, these situations suppress the formation of O_2 at high temperatures and the formation of NO concentration at low temperature, as it increases the barrier in the product channel on the reaction pathway and $NO+O$ recombination in the reactant channel under favorable conditions. Under these two conditions, the NO_2 population might be supported by electric field. It is important to research the reactions belonging to $O(^3P)$ (atom used in present study) with high concentration occurred in airglow events such as lightning flash. O_2 can be produced by the interaction of $O(^3P)$ atoms to each other, which also causes the emergence of the $O(^1S)$ atom (it interacts with excited oxygen molecules and disappears to form ozone) in the high temperature region. However, it is 10^6 times less than NO molecules in population. Moreover, in the low temperature region, these stimulated oxygen contributes very little to O_2 production. Another reaction that produces O_2 in atmospheric chemistry in the presence of NO and O_3 in high population is $NO+O_3 \rightarrow NO_2 + O_2$. This reaction is defined below 500 K. However, this reaction does not show Arrhenius behaviour in the studied shock wave temperature range as can be seen from the change in concentrations in the study of Ripoll et al. (2014). To produce O_2 around 1000 K as in atmospheric and experimental, higher reactant vibrational energy must be obtained. High vibration energy is the reaction starter in reactions occurring under such shock waves.

Acknowledgements

The numerical calculations reported in this paper were partially performed at TUBITAK ULAKBIM, High Performance and Grid Computing Center (TRUBA resources). That is why, the author is grateful to the Scientific and Technological Research Council of Turkey for TR-Grid facilities and to Bitlis Eren University for Gaussian09W and GaussView5.0 Program support.

References

- Bazelyan EM, Raizer YP, Aleksandrov NL. 2008. Corona Initiated from Grounded Objects Under Thunderstorm Conditions and its Influence on Lightning Attachment, Plasma Sources Sci. Technol. 17: 024015. doi:10.1088/0963-0252/17/2/024015.
- Coleman LM, Marshall TC, Stolzenburg M, Hamlin T, Krehbiel PR et al. 2003. Effects of Charge and Electrostatic Potential on Lightning Propagation. Journal of Geophysical Research 108 (D9): 4298. doi:10.1029/2002JD002718.
- Fedotov VG, EYa F. 2015. The Chain Reaction of Atmospheric Nitrogen Oxidation, Initiated by an Electric Discharge in Air, J. Phys. Chem. Biophysics, 5: 195. doi:10.4172/2161-0398.1000195.
- Franzblau E, Popp CJ. 1989. Nitrogen Oxides Produced from

- Lightning, *Journal of Geophysical Research*, 94 (D8): 89-104. doi:10.1029/JD094iD08p11089.
- Frisch MJ, Trucks GW, Schlegel HB, Scuseria GE, Robb MA, et al. 2009. Gaussian 09, Revision A.1, Gaussian Inc., Wallingford CT.
- Grebenshchikov SY, Beck C, Flöthmann H, Schinke R, Kato S. 1999. Unimolecular Dissociation of NO₂. I. Classical Trajectory and Statistical Calculations on a Global Potential Energy Surface, *J. Chem. Phys.* 111: 619. doi.org/10.1063/1.479342.
- Hill RD, Rinker RG, Wilson HD. 1980. Atmospheric Nitrogen Fixation by Lightning, *Journal of Atmos. Sci.* 37: 179-192. doi.org/10.1175/1520-0469(1980)037<0179:ANFBL>2.0.CO;2.
- Ivanov MV, Zhu H, Schinke R. 2007. Theoretical Investigation of Exchange and Recombination Reactions in O(³P) + NO (²Π) Collisions, *The Journal of Chemical Physics* 126: 054304. doi.org/10.1063/1.2430715.
- Jacobson MZ and Streets DG. 2009. Influence of Future Anthropogenic Emissions on Climate, Natural Emissions and Air Quality. *Journal of Geophysical Research* 114: D08118. doi:10.1029/2008JD011476.
- Kherbouche F, Benmimoun Y, Tilmatine A, Zouaghi A, Zouzou N. 2016. Study of a New Electrostatic Precipitator with Asymmetrical Wire-to- Cylinder configuration for Cement Particles Collection, *Journal of Electrostatics* 83: 7-15. doi.org/10.1016/j.elstat.2016.07.001.
- Kunova O, Nagnibeda E. 2017. On the Influence of State-Resolved Rates of Zeldovich Reactions on Shock Heated Air Flow Parameters, *J. Phys., Conf. Ser.* 815: 012009. pp. 1-8.
- Lagzi I, Meszaros R, Gelybo G, Leelossy A. 2013. Atmospheric Chemistry, Eötvös Lorand University, Consortium Members: ELTE Faculties of Science Student Foundation, ITStudy Hungary Ltd.
- Larossi S, Poscolieri M, Rafanelli C, Franceschinis D, Rondini A et al. 2011. The Measure of Atmospheric Electric Field. In G. Neri et al. (eds.), *Sensors and Microsystems, Lecture Notes in Electrical Engineering* 91, Springer Science+Business Media B.V, pp. 175-179.
- Levine IN. 1995. *Physical Chemistry*. 4th Edition, McGraw-Hill, Inc., New York.
- MacGorman DR, Rust WD. 1998. *The Electrical Nature of Storms*, Oxford University Press. Inc., 198 Madison Avenue, New York 10016.
- Michalski G, Jost R, Sugny D, Joyeux M, Thiemens M. 2004. Dissociation Energies of Six NO₂ Isotopologues by Laser Induced Fluorescence Spectroscopy and Zero-Point Energy of Some Triatomic Molecules, *J. Chem. Phys.* 121: 7153. doi:10.1063/1.1792233
- Rakov VA, Uman MA. 2003. *Lightning Physics and Effects*. Cambridge University Press, Cambridge, CB2 2RU, UK.
- Riba JR, Morosini A, Capelli F. 2018. Comparative Study of AC and Positive and Negative DC Visual Corona for Sphere-Plane Gaps in Atmospheric Air, *Energies*, 11: 2671. doi.org/10.3390/en11102671.
- Ripoll J-F, Zinn J, Jeffery CA, and Colestock PL. 2014. On the Dynamics of Hot Air Plasmas Related to Lightning Discharges: 1. Gas dynamics. *J. Geophys. Res. Atmos.*, 119, 9196–9217.
- Salonen H, Salthammer T, Morawska L. 2019. Human exposure to NO₂ in School and indoor environments, *Environment International*, 130: 104887. doi: 10.1016/j.envint.2019.05.081.
- Sayos R, Oliva C, Gonzalez M. 2002. New Analytical (²A', ⁴A') Surfaces and Theoretical Rate Constants for the N(⁴S) + O₂ Reaction, *Journal of chemical Physics*, 117 (2): 670-679. doi.org/10.1063/1.1483853.
- Schumann U, Huntrieser H. 2007. The global Lightning-Induced Nitrogen Oxides Source, *Atmos. Chem. Phys.*, 7: 3823-3907. doi.org/10.5194/acp-7-3823-2007.
- Smirnov SE, Marapulets YV. 2012. Influence of a Single Lightning Discharge on the Intensity of an Air Electric Field and Acoustic Emission of Near-Surface Rocks, *Soild Earth*, 3: 307-311. doi.org/10.5194/se-3-307-2012.
- Tuck AF. 1976. Production of Nitrogen Oxides by Lightning Discharges, *Quart. J. R. Met. Soc.*, 102: 749-755. doi.org/10.1002/qj.49710243404.
- Wolfram Research, Inc., 2019. *Mathematica*, Version 12.0, Champaign, IL.

Available online at www.dergipark.gov.tr/beuscitech

Journal of Science and Technology

E-ISSN 2146-7706



Study on crystallization process of SiO₂ based SiO₂-Li₂O nano-wire glass ceramic: A molecular dynamics simulation based on SCC-DFTB calculations

Fatih Ahmet CELIK ^{a,*} ^a Bitlis Eren University, Faculty of Arts & Sciences, Physics Department, TR-13000, Bitlis, Turkey

ARTICLE INFO

Article history:

Received 02 November 2021

Received in revised form 01 December 2021

Accepted 01 December 2021

Keywords:

SCC-DFTB

Molecular dynamics

SiO₂-Li₂O glass ceramic

Nano-wire

ABSTRACT

The aim of this study was to investigate the crystallization behavior of nano-wire SiO₂-Li₂O glass ceramic (GC) during the slow cooling process by using density functional theory (DFT). For this purpose, the extended tight-binding with self-consistent charge (SCC-DFTB) was used to investigate the geometric optimization and molecular dynamics (MD) process for model system. The structural development was analysed by radial distribution function (RDF) at determined temperatures. The results show that the system tends to crystallization at lower temperatures and transforms from liquid phase to crystal phase with a slow cooling rate.

© 2020. Turkish Journal Park Academic. All rights reserved.

1. Introduction

Today, glass-ceramics (GC) are applied in many advanced technology areas due to their superior corrosion resistance and toughness properties compared to traditional glasses and metals [1, 2]. Some of them include biomedical applications, superconducting materials, materials with high dielectric constant and applications to the field of electronics [3]. In addition, they are produced in many lithium-based materials and have great advantages in terms of their physical and mechanical properties [4]. Among these, lithium dioxide (Li₂O) is mild compared to other compounds, has a low viscous temperature, high conductivity, good formability and high optical properties [5-7].

Being used as materials in different technological areas, lithium-silicate glass-ceramics are well known for their good mechanical properties [7]. Lithium silicates are particularly interesting materials due to their tritium-forming and similar properties and their compatibility with building materials [4-

7]. Lithium silicate glass-ceramics have superior mechanical and optical properties when used in multi-component systems. Due to these properties, they have many studies in theory and many applications in practice. Lithium silicate GCs are mostly used in ceramic-metal sealing joints and dental applications [8]. However, most of their characteristic behaviours are still unexplained. In particular, there are deficiencies in the nanostructure related to processes based on a number of experimental measurements, such as crystallization mechanism and kinetics. The use of computational methods to eliminate such deficiencies is increasing day by day. Especially, molecular dynamics (MD) simulations based on DFT and classical interactions are useful way to investigate many physical properties of molecules as a function of time and temperature [9-11]. This method used to calculate, for example, the total energy during physical and chemical processes can be determine because it provides thermal treatment for a period of time [12].

* Corresponding author. Tel.: +90 (434) 222 00 00; fax: +90 (434) 222 01 01

E-mail address: facelik@beu.edu.tr

ORCID : 0000-0001-7860-5550 (F.A. Çelik)

2. Material and Method

2.1. DFT and MD details

The extended tight-binding with self-consistent charge (SCC-DFTB) approach based on quantum mechanical methodology is a DFT-based method regarding to the electron density fluctuations [13, 14]. The set of parameters QUASINANO2013.1 [15] available in the Amsterdam Density Functional (ADF) library is utilized for single point calculations of molecules [16-18]. More details about the SCC-DFTB method can be found in Refs. [13, 14]. The MD simulations are performed using the ADF software (version 2020.104) [18]. In our study, SCC-DFTB is used for MD simulations. The Berendsen [19] thermostat and barostat are adopted to control temperature and pressure of the system and time-step is set as 1.25 fs during the simulation. Firstly, the system is equilibrated for 12.5 ps at 2500 K and secondly, the temperature of system decreases from 2500 K to 300 K within 625 ps with a cooling rate of 3.52×10^{12} K/s. The main parameters and atomic configurations are recorded at every 12.5 ps to investigate the structural and thermal changes.

3. Results and Discussions

We have built a $\text{SiO}_2\text{-Li}_2\text{O}$ glass ceramic structure to investigate the geometric optimization and MD process using SCC-DFTB. For this purpose, SiO_2 crystal lattice has been set up according to Fd3m space group by using builder option in SCIGRESS software [20]. Li_2O atoms are distributed to upper and top side of SiO_2 in the simulation box which contains 120 atoms. As a start, the bulk GC system is transformed to a nanowire structure with 39 Å lattice parameter at one dimension. Then, this nano-wire GC is optimized to determine most stable structure. The nanowire $\text{SiO}_2\text{-Li}_2\text{O}$ GC model system is shown in Fig. 1.

Fig. 2 shows the geometric optimization process and the final structure of $\text{SiO}_2\text{-Li}_2\text{O}$ GC at the end of optimization with respect to the frame number or optimization iteration steps. The energy of the GC system has the maximum value at the beginning of optimization. The energy reaches its minimum value at the final optimization because the system has high stability compared with the beginning structure.

Fig. 3 and Fig. 4 show the variation of some physical parameters with frame number or MD steps during the MD process for $\text{SiO}_2\text{-Li}_2\text{O}$ GC. As seen from figure that the temperature of system is linearly decrease with MD time after relaxation. The total energy of system decreases with increasing MD time during slow cooling process. The bond lengths between some selected atoms exhibit the fluctuations at liquid phase due to increase of atomic mobility. These fluctuations dramatically decrease after 400 ps because the system transforms a stable crystal phase.

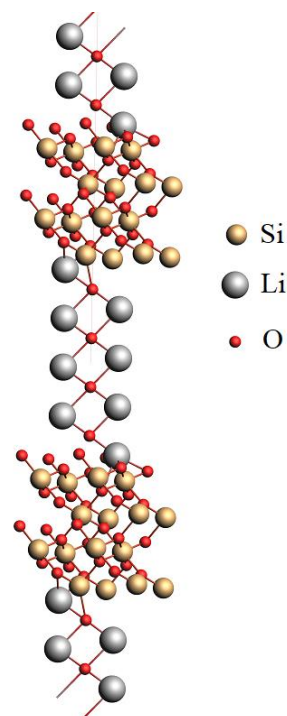


Figure 1. The nanowire $\text{SiO}_2\text{-Li}_2\text{O}$ GC model (Gray atoms, yellow atoms and red atoms represent Li, Si and O, respectively).

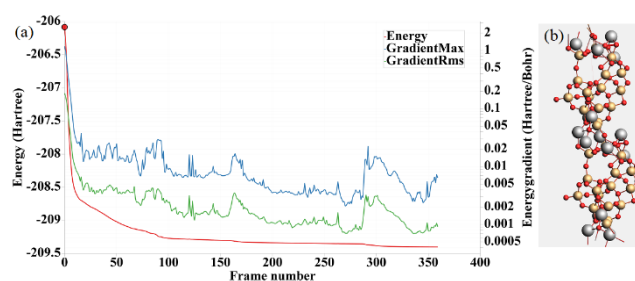


Figure 2. Optimization process of model system (a) variation of energy with optimization iteration (b) final structure of $\text{SiO}_2\text{-Li}_2\text{O}$ nano-wire GC at the end of optimization.

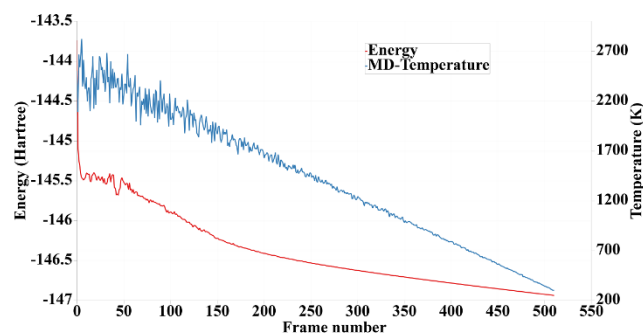


Figure 3. The variation of total energy and temperature of system during MD process.

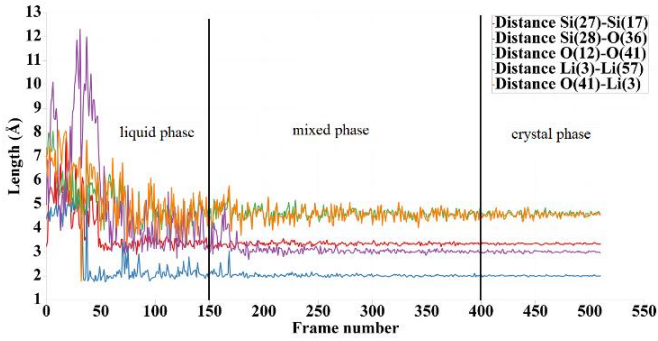


Figure 4. Variation of distance between some selected atoms during MD process.

Fig. 5 shows a snapshot from MD simulations corresponding to nanowire model system at beginning structure, the structure at 2500 K and final structure at 300 K, respectively. We can say from figure that the atomic distribution in the system at 2500 K more disordered than beginning structure due to increase of atomic mobility as seen Fig. 4. Hence, the volume of system is seen broadly at 2500 K. But, the atomic mobility increases with the decreasing of temperature. It can be said that the system has a more ordered structure. These results can be support with radial distribution function (RDF) analysis.

The structural characteristics of a system can be analysed by radial distribution function (RDF, $g(r)$) which provides the probability of finding neighbor atoms at a distance of r from an atom [21]. Fig. 6 shows the partial RDFs or $g(r)$ of bond pairs (Si-Si, Si-O, O-O and Si-Li) for system at 2500 K, respectively. The first peak in the RDFs represents the short-range order, and the second peak becomes more broadened compared to the first peak of the RDF curve because the periodic crystal order is not dominant at the liquid phase. Fig. 7 shows the partial RDFs of bond pairs (Si-Si, Si-O, O-O and Si-Li) for system at 300 K, respectively. From figure, the much higher order peaks at long atomic distances in the RDFs represent the long-range order because of formation of stable crystal structure. We observe that slow cooling rate causes in better-defined crystal peaks with higher values of the first and second maximum of $g_{Si-O}(r)$.

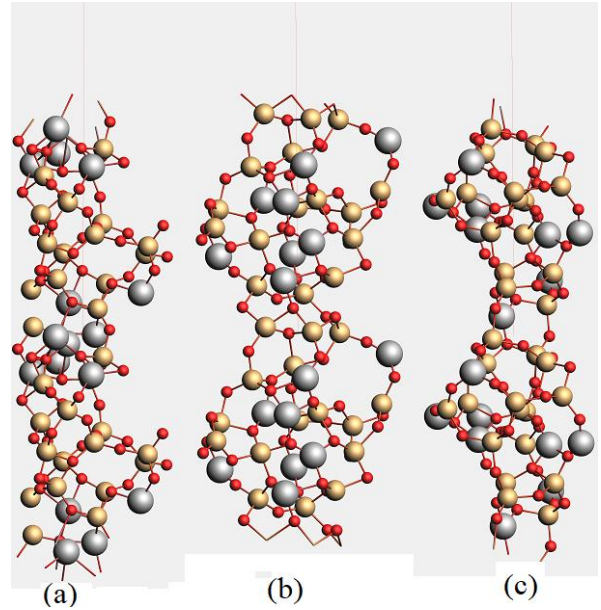


Figure 5. A snapshot corresponding to nanowire model (a) beginning structure b) structure at 2500 K c) final structure at 300 K.

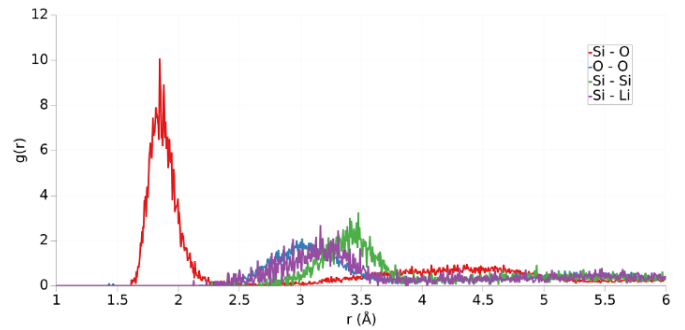


Figure 6. The partial RDF curves at 2500 K.

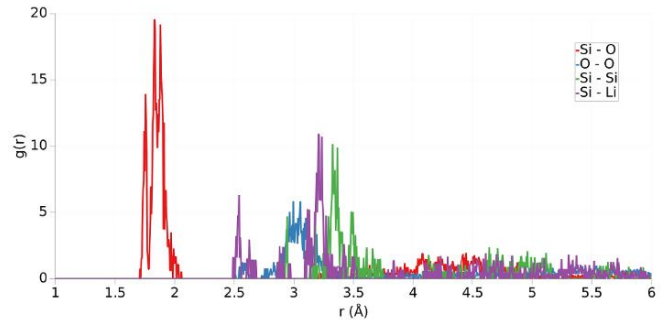


Figure 7. The partial RDF curves at 300 K.

4. Conclusions

In summary, we performed SCC-DFTB based on density functional theory calculations on the crystallization process of nano-wire $\text{SiO}_2\text{-Li}_2\text{O}$ glass ceramic with molecular dynamics simulation method. The total energy was minimum value at the final of optimization. With the DFTB calculations, MD simulations for the slow cooling of system have been conducted. The atomic mobility's decreased during solidification and the position of the RDFs peaks emerged at longer atomic distances because the crystallization occurs at lower temperatures with a slow cooling rate.

Acknowledgements

We grateful to Bitlis Eren University Scientific Research coordination center (BEBAP Project number 2021.13) for the financial support of this work

References

- [1] Wendler, M., Belli, R., and Lohbauer, U., 2019. Factors influencing development of residual stresses during crystallization firing in a novel lithium silicate glass-ceramic. *Dental Materials*, 35(6), 871-882.
- [2] Konar, B., Van Ende, M.A., and Jung, I.H., 2017. Critical evaluation and thermodynamic optimization of the Li-O, and LiO-SiO₂ systems. *Journal of the European Ceramic Society*, 37(5), 2189-2207.
- [3] Ota, R., Mishima, N., Wakasugi, T., and Fukunaga, J., 1997. Nucleation of Li₂O-SiO₂ glass and its interpretation based on a new liquid model. *Journal of non-crystalline solids*, 219, 70-74.
- [4] Doremus, R.H., and Turkalo, A.M., 1972. Crystallization of Lithium Disilicate in Lithium Silicate Glasses. *Phys. Chem. Glasses*, 13(1), 14.
- [5] Ray, C.S., Day, D.E., Huang, W., Narayan, K.L., Cull, T. S., and Kelton, K.F., 1996. Non-isothermal calorimetric studies of the crystallization of lithium disilicate glass. *Journal of Non-Crystalline Solids*, 204(1), 1-12.
- [6] Anspach, O., Keding, R., and Rüssel, C., 2005. Oriented lithium disilicate glass-ceramics prepared by electrochemically induced nucleation. *Journal of non-crystalline solids*, 351(8-9), 656-662.
- [7] Fernandes, H.R., Tulyaganov, D.U., Goel, I.K., and Ferreira, J.M., 2008. Crystallization process and some properties of Li₂O-SiO₂ glass-ceramics doped with Al₂O₃ and K₂O. *Journal of the American Ceramic Society*, 91(11), 3698-3703.
- [8] Qi, J., Liu, C., and Jiang, M., 2021. Effect of Li₂O on the crystallization behavior of CaO-Al₂O₃-SiO₂-Li₂O-Ce₂O₃ mold slags. *Ceramics International*, 47, 20850.
- [9] Slater, J.C., and Koster, G.F., 1954. Simplified LCAO method for the periodic potential problem. *Physical Review*, 94(6), 1498.
- [10] Porezag, D., Frauenheim, T., Köhler, T., Seifert, G., and Kaschner, R., 1995. Construction of tight-binding-like potentials on the basis of density-functional theory: Application to carbon. *Physical Review B*, 51(19), 12947.
- [11] Oliveira, A.F., Seifert, G., Heine, T., and Duarte, H.A., 2009. Density-functional based tight-binding: an approximate DFT method. *Journal of the Brazilian Chemical Society*, 20, 1193-1205.
- [12] Celtek, M., Sengul, S., Domekeli, U., and Guder, V., 2021. Dynamical and structural properties of metallic liquid and glass Zr₄₈Cu₃₆Ag₈Al₈ alloy studied by molecular dynamics simulation. *Journal of Non-Crystalline Solids*, 566, 120890.
- [13] Liu, H., Seifert, G., and Di Valentin, C., 2019. An efficient way to model complex magnetite: Assessment of SCC-DFTB against DFT. *The Journal of chemical physics*, 150(9), 094703.
- [14] Chopra S., 2020. Performance study of the electronic and optical parameters of thermally activated delayed fluorescence nanosized emitters (CCX-I and CCX-II) via DFT, SCC-DFTB and B97-3c approaches, *J Nanostruct Chem.* 10, 115-124.
- [15] Oliveira A.F., Philipsen, P., and Heine T., 2015. DFTB Parameters for the Periodic Table, Part 2: Energies and Energy Gradients from Hydrogen to Calcium, *Journal of Chemical Theory and Computation* 11 (11), 5209-5218.
- [16] Te Velde, G.T., Bickelhaupt, F.M., Baerends, E.J., Fonseca Guerra, C., van Gisbergen, S.J., Snijders, J.G., and Ziegler, T., 2001. Chemistry with ADF. *Journal of Computational Chemistry*, 22(9), 931-967.
- [17] Guerra, C.F., Snijders, J.G., te Velde, G.T., and Baerends, E.J., 1998. Towards an order-N DFT method. *Theoretical Chemistry Accounts*, 99(6), 391-403.
- [18] ADF2013.01, SCM, Theoretical Chemistry, Vrije Universiteit Amsterdam, The Netherlands, 2013 <http://www.scm.com>.
- [19] Berendsen, H.J., Postma, J.V., van Gunsteren, W.F., DiNola, A.R.H.J., and Haak, J.R., 1984. Molecular dynamics with coupling to an external bath. *The Journal of chemical physics*, 81(8), 3684-3690.
- [20] Fujitsu Limited., 2021, Tokyo, Japan.
- [21] Yuan, Y.Q., Zeng, X.G., Chen, H.Y., Yao, A.L., and Hu, Y.F., 2013. Molecular dynamics simulation on microstructure evolution during solidification of copper nanoparticles. *Journal of the Korean Physical Society*, 62(11), 1645-1651.

Available online at www.dergipark.gov.tr/beuscitech

Journal of Science and Technology

E-ISSN 2146-7706



Trace element geochemistry of Bitlis ignimbrites sourced by Quaternary Nemrut Volcano: inferences for A₂-type magma generation in Eastern Anatolia post-collisional extensional setting

Hakan ÇOBAN ^{a,*} , Özcan Ali KALKAN ^b 

^a Bitlis Eren University, Department of Civil Engineering, TR-13000, Bitlis, Turkey

^b Batman University, Department of Geological Engineering, TR-72100, Batman, Turkey

ARTICLE INFO

Article history:

Received 10 November 2021

Received in revised form 22 November 2021

Accepted 01 December 2021

Keywords:

Bitlis ignimbrite

A₂-type magma

K-Ar dating

Eastern Anatolia

ABSTRACT

In the study presented here, we investigated the whole-rock K-Ar dating and petrological significance of trace element compositions Bitlis (Eastern Anatolia) ignimbrites associated with explosive activities of the well-known Quaternary Nemrut volcano. Considering the previous age determinations (40.9 ka – 264.1 ka) of ignimbrites sourced in Nemrut volcano, and because they contain lithic clasts, obtained whole-rock K-Ar age of Bitlis ignimbrite flow deposits suggest that they are younger than late Pleistocene (< 790 ka), and occurred as the first products of pre-caldera stages of Nemrut stratovolcano. Bitlis trachydacitic ignimbrites with shoshonitic affinity are characterized by the typical negative anomalies of Eu, Nb-Ta, and Ti in chondrite-normalized spider and multi-element variation diagrams, and plot in the fields of within-plate and post-collisional tectonic setting in Rb vs Y+Nb discrimination diagram. Accordingly, similar to that of Nemrut volcanic products, trace element signatures (e.g., high Nb, Ce, Y, and Zr contents) of Bitlis ignimbrites show coincidence with geochemical characteristics of A₂-type silicic magmas. Relative to the upper crust, higher La/Ba and Nb/La, and lower Ba/Ta and La/Ta ratios of Bitlis ignimbrites, which are close to that of Nemrut basalts previously reported as the most recent volcanic products, suggest an interaction between OIB-like basaltic magma and upper crust. Our results point to A₂-type silicic magma generation in Eastern Anatolia post-collisional extensional setting, and Nemrut lava and pyroclastic rocks (e.g., Bitlis ignimbrites) formed by partial melting of upper crustal rocks at shallow level via interaction with OIB-like basaltic magma derived from a common mantle source.

© 2021. Turkish Journal Park Academic. All rights reserved.

1. Introduction

Felsic ignimbrite flows generated by explosive Quaternary active Nemrut volcano from Eastern Anatolia (e.g., Karaoğlu et al., 2005; Özdemir et al., 2006; Koralay et al., 2011, 2014; Çubukcu et al., 2012, Sumita and Schminke et al., 2013; Schminke and Sumita, 2014) are well exposed along with Bitlis valley. Although, stratigraphic position, mineralogical, petrographical, and major-chemical compositions of Bitlis ignimbrites have been studied by some researchers (e.g., Karaoğlu et al., 2005; Koralay et al., 2011, 2014), geochronological dating and trace element compositions of these rocks are still lacking. Hence, in this study, K-Ar age determination and trace and rare earth element (REE) analysis

have been performed on bulk-rock samples of Bitlis ignimbrites. The magma type, from which they produced, geochemical characteristics and petrological signatures of Bitlis ignimbrites and associated felsic-silicic volcanic rocks of Nemrut volcano, which are derived from a common magma source, have also been discussed.

1.1. Bitlis ignimbrites in the geological setting

Quaternary active Nemrut volcano is situated 12 km north of the Bitlis-Zagros suture zone, southern margin of continental collision between Arabian and Anatolian plates (Çubukcu et al., 2012) (Figure 1). The Bitlis ignimbrites exposed in the Bitlis area (Eastern Anatolia) are a restricted-volume, pyroclastic deposit generated by Nemrut volcano in the Quaternary (Fig.

* Corresponding author. Tel.: +0 532 730 6733

E-mail address: hcoban@beu.edu.tr

ORCID : 0000-0002-9614-6818 (H. Çoban), 0000-0002-1743-4425 (O.A. Kalkan)

1, Özdemir et al., 2003; Karaoğlu et al., 2005; Koralay et al., 2011, 2014). The Bitlis ignimbrite flows overly the metamorphic basements (known as Bitlis metamorphics) comprising Devonian to Cretaceous metasedimentary rocks along with Bitlis valley (Fig. 1). Recent alluvium and travertines are the youngest lithological units in the study area (Fig. 1). The columnar structures of Bitlis ignimbrites along with Bitlis valley are their most characteristic feature (Fig. 2). They have a massive, matrix-supported structure, poorly sorted, with lithic and pumice clasts of varying size scattered in the ash matrix, not showing evident grading of coarse clasts (Koralay et al., 2011). They are generally homogeneous throughout their thickness. The Bitlis silicic ignimbrites associated with Quaternary Nemrut explosive stratovolcano have a high thickness (up to 8m) in Bitlis valley. Detailed mineralogical and petrographical properties of these ignimbrites are not given here and can be found in Koralay et al., (2011 and 2014).



Figure 2. Field view of Bitlis ignimbrites showing the columnar structure, in Bitlis valley.

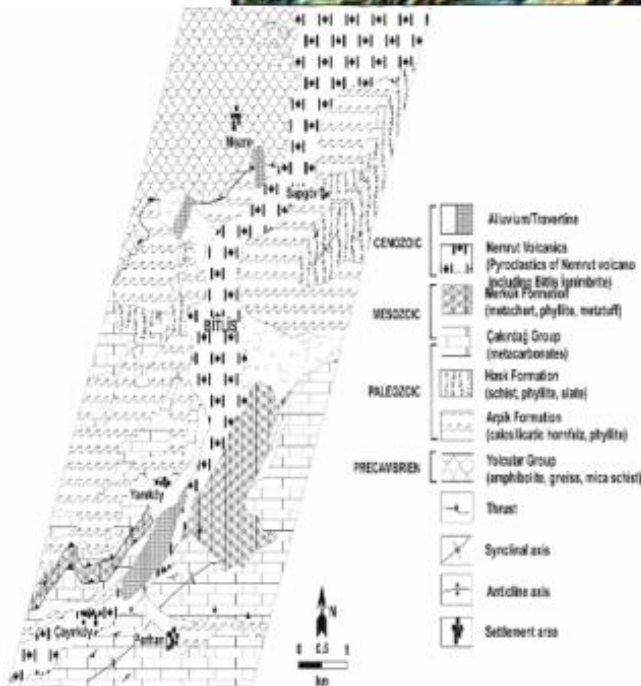


Figure 1. Location (upper figure) and geological (lower figure) maps of the study area (modified from Sumita and Schminke et al., 2013, and Şengün et al., 1991).

2. Methodology

Whole-rock K-Ar isotopic age analyses of the sample BH4 from Bitlis ignimbrites were conducted in the ACT-LAB (Canada), using the MI-1201 IG mass spectrometer. Aliquots of the sample were weighted into Al container, loaded into the sample system of the extraction unit, degassed at $\sim 100^{\circ}\text{C}$ during 2 days to remove the surface gases. Argon is extracted from the sample in a double vacuum furnace at 1700°C . The determination of radiogenic argon content was carried out twice on MI-1201 IG mass-spectrometer by isotope dilution method with ^{38}Ar as the spike, which is introduced to the sample system prior to each extraction. The extracted gases were cleaned up in a two-step purification system. Then pure Ar is introduced into a custom-built magnetic sector mass spectrometer (Reinolds type). Two globally accepted standards (P-207 Muscovite and 1/65 "Asia" rhyolite matrix) were measured for ^{38}Ar spike calibration. For age calculations the international values of constants were used as follow:

$$\lambda_K = 0.581 \cdot 10^{-10} \text{y}^{-1}, \quad \lambda_{\beta} = 4.962 \cdot 10^{-10} \text{y}^{-1}, \quad 40\text{K} = 0.01167 \text{ (at.\%)}$$

The major, trace and REE analyses of five bulk-rock samples of Bitlis ignimbrites have been performed in the Geochemistry Research Laboratories of Istanbul Technical University (ITU/JAL). The samples were grounded using a Tungsten Carbide milling device. Major elements of the samples were analyzed using a BRUKER S8 TIGER model X-ray fluorescence spectrometer with a wavelength range from 0.01–12 nm. Trace elements were analyzed by Inductively Coupled Plasma-Mass Spectrometry using an ELAN DRC-e Perkin Elmer model. Approximately 50 mg of powdered sample was digested in two steps. The first step was completed with 6 ml of 37% HCl, 2 ml of 65% HNO₃, and 1 ml of 38–40% HF in a pressure- and temperature-controlled Teflon beaker using a Berghoff Microwave at 135 °C. The second step was completed with the addition of 6 ml of 5% boric acid solution.

3. Results and Discussion

3.1. K-Ar dating

Obtained data from the whole-rock K-Ar geochronological dating of Bitlis ignimbrites gave the age of 790 ka (late Pleistocene) and presented in Table 1. The historically active Nemrut Volcano (Eastern Anatolia) has been the source of intense Plinian eruptions for >530.000 years (Sumita and Schmincke, 2013). Previous age determinations of ignimbrites sourced in Nemrut volcano gave the ages of between 40.9 ka and 264.1 ka (Sumita and Schmincke, 2013). Çubukcu et al., (2012) indicated that the oldest volcanic rocks (~1.0 Ma) from Nemrut caldera are determined from metaluminous trachytes/rhyolites. Apart from the older age of 2.5 Ma for a widespread basaltic lava flow exposed along the Bitlis Gorge, all other dates range from ca. 0.5 Ma to the Holocene (Sumita and Schmincke, 2013). Considering the overall eruptive history of Quaternary Nemrut stratovolcano (e.g., Özdemir et al., 2006; Çubukcu et al., 2012; Sumita and Schmincke et al., 2013; Schmincke and Sumita, 2014), obtained age data of the Bitlis ignimbrites including lithic clasts indicate that they are younger than late Pleistocene (< 790.000 years), and corresponds to the first silicic products of the pre-caldera stage of Nemrut volcano, which confirm the initiation of early-stage silicic pyroclastic products with trachydacitic ignimbritic flow deposits at the south of caldera.

Table 1. K-Ar isotopic age analyses of Bitlis ignimbrites

Sample	K, % ± σ	⁴⁰ Ar rad, (ng/g)	% ⁴⁰ Ar air	Age, Ma	Ma Error 2σ
BH-4	4.27±0.05	0.235±0.006	78.7	0.79	0.04

3.2. Trace element inferences for magma style of Bitlis ignimbrites and Nemrut felsic volcanic rocks

Major oxide, trace, and REE analyses of five samples from Bitlis ignimbrites are presented in Table 2. In terms of the TAS (total alkali-silica) diagram of Le Maitre et al., (2002), Bitlis ignimbrites can be classified as trachydacite in composition (not shown). Bitlis trachydacitic ignimbrites (K_2O/Na_2O ratios range between 1.1 to 1.5) and Nemrut felsic-silicic volcanic rocks with potassic character (e.g., Özdemir et al., 2006; Çubukcu et al., 2012) show a shoshonitic affinity ($K_2O/Na_2O = \approx 1$) (not shown). As shown in Figs. 3a and b, Bitlis ignimbrites demonstrate pronounced Nb-Ta, P, and Ti depletions in the primitive-mantle normalized multi-element diagram, and an obvious negative Eu anomaly in chondrite-normalized REE diagram, which are consistent with that of the upper crust (Rudnick and Gao, 2004). Such geochemical anomalies are also akin to Nemrut felsic-silicic volcanic rocks having slightly but remarkable negative anomalies of Nb-Ta, P, and Ti (Özdemir et al., 2006; Çubukcu et al., 2012). Slight negative Nb-Ta depletion is also observed in Nemrut basalts (Özdemir et al., 2006). Considering their geochemical characteristics, the Bitlis ignimbrites and Nemrut felsic-silicic volcanic rocks demonstrate a chemical affinity to A-type silicic magmas with high $FeO_{tot}/(FeO_{tot}+MgO)$ and Ga/Al ratios, $\Sigma(K_2O+Na_2O)$,

and $\Sigma(Zr+Nb+Ce+Y)$ contents (Whalen et al., 1987; Eby, 2011), and the Bitlis ignimbrites and Nemrut felsic-silicic volcanic rocks fall well within the fields of A-type silicic magmas (Figs. 4a and b). For A-type magmas, Eby (1992) further divided them into genetically distinct A1-anorogenic and A2-post-orogenic chemical subgroups. As shown in Fig 4c, the Bitlis ignimbrites and Nemrut felsic volcanic rocks plot within the A2 subgroup, which are also compatible with within-plate and post-collisional settings, which are shown in Fig. 4d.

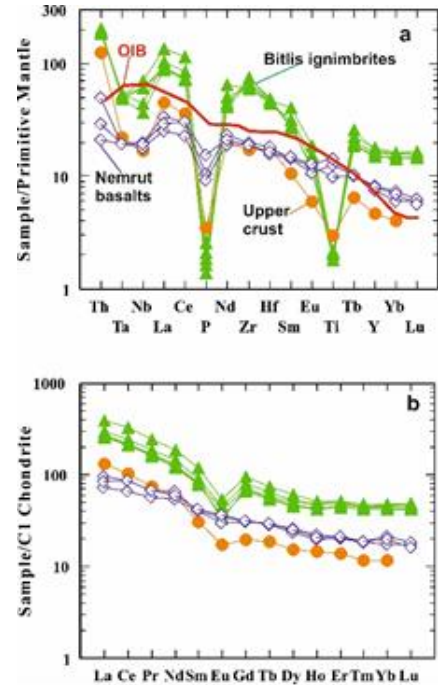


Figure 3. Primitive mantle-normalized multi-element (a) and chondrite-normalized REE (b) diagrams of the Bitlis ignimbrites. Normalized values and OIB are from Sun and McDonough (1989). The upper crust is from Rudnick and Gao (2004). Nemrut basalts are from Özdemir et al., (2006).

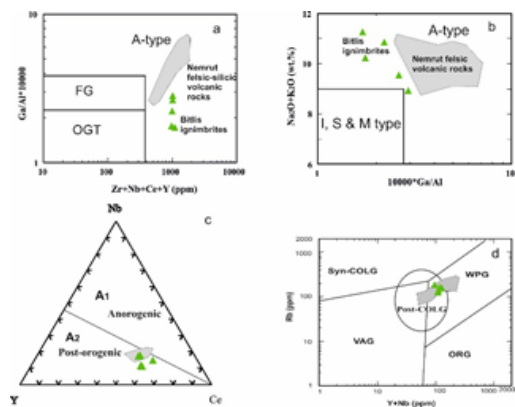


Figure 4. Ga/Al vs $Zr+Nb+Ce+Y$ (a), Na_2O+K_2O vs Ga/Al (b), Y-Nb-Ce triangle (c) and Rb vs Y+Nb (d) variation diagrams for Bitlis ignimbrites. For comparison, Nemrut felsic-silicic volcanic rocks (Özdemir et al., 2006) are also plotted. A-type, A1 and A2 type, FG, OGT, I, S, and M type magma fields are from Whalen et al., (1987) and Eby, (2011). Syn-COLG, ORG, VAG, WPG, and Post-COLG fields in d are from Pearce (1996).

Table 2. Major, trace and REE analysis of Bitlis ignimbrites.

(wt.%)	BH1	BH2	BH3	BH4	BH5
SiO ₂	67,14	66,99%	65,06%	64,64%	67,08%
TiO ₂	0,46%	0,46%	0,46%	0,44%	0,39%
Al ₂ O ₃	14,12%	13,96%	15,47%	15,39%	13,71%
Fe ₂ O ₃	3,95%	3,97%	3,49%	4,43%	4,46%
MgO	0,13%	0,21%	0,12%	0,16%	0,17%
CaO	1,32%	1,36%	1,25%	1,27%	1,16%
Na ₂ O	3,54%	4,54%	5,31%	4,90%	4,14%
K ₂ O	5,33%	5,65%	5,91%	5,91%	5,36%
MnO	0,05%	0,11%	0,08%	0,10%	0,08%
P ₂ O ₅	0,11%	0,08%	0,07%	0,09%	0,06%
LOI	3,48%	2,26%	2,34%	2,25%	3,02%
Total	99,63%	99,59%	99,56%	99,58%	99,63%

(trace element in ppm)					
Sc	7	6	4	4	4
Co	39	21	36	15	12
Ni	59	83	33	25	130
Ga	21	13	142	18	19
Rb	157	138	186	127	165
Sr	104	52	84	57	50
Zr	665	681	835	724	748
Nb	50	31	26	43	43
Ba	749	763	772	657	566
Pb	66	105	41	45	43
U	9	8	8	7	6
Y	76,000	81,000	69,000	67,000	73,000
Hf	14,000	13,600	15,000	14,400	19,000
Ta	2,100	2,000	1,900	2,100	2,000

(REE in ppm)					
La	92,987	70,603	61,865	60,710	64,771
Ce	202,761	149,41	131,69	128,13	130,28
Pr	23,343	17,592	15,461	15,119	16,123
Nd	87,620	68,152	57,639	56,159	60,480
Sm	18,131	14,025	12,360	11,858	12,449
Eu	3,154	2,596	2,425	2,054	1,906
Gd	19,604	16,281	14,113	13,342	14,565
Tb	2,788	2,405	2,057	2,007	2,176
Dy	15,328	13,502	11,791	11,640	12,813

Ho	2,934	2,789	2,449	2,403	2,688
Er	8,461	8,478	7,663	7,348	8,121
Tm	1,140	1,210	1,121	1,064	1,166
Yb	7,782	8,026	7,325	7,076	7,874
Lu	1,147	1,228	1,106	1,066	1,220
Th	15,736	16,637	16,494	16,104	17,127

3.3. Petrological inferences

Based on the trace element variations, it can be concluded that the Nemrut stratovolcano and derivative felsic volcanic and pyroclastic products (e.g., Bitlis ignimbrites) were derived from an A2-type silicic magma, which occurs in post-collisional or post-tectonic setting (Eby, 2011). In tectonic discrimination diagrams, overlapping post-orogenic and within-plate settings of A2-type Quaternary Nemrut felsic-silicic volcanic and pyroclastic products are consistent with the magma emplacement in a post-collisional extensional tectonic environment in Eastern Anatolia. Although Nemrut volcanic and pyroclastic products (e.g., Bitlis ignimbrites) show close affinity to the upper crust (see Figs. 3a-b), their A2-type magma character also requires the role of mantle-derived basaltic magma on their genesis (Medlin et al., 2015). The interaction of mantle-derived magma with crust can also be inferred from exposed basaltic magma eruptions of Nemrut caldera (e.g., Özdemir et al., 2006; Çubukçu et al., 2012). To confirm the interaction between mantle-derived magma and upper crust in the genesis of Nemrut volcanic and associated pyroclastic rocks (e.g., Bitlis ignimbrites), we used the La/Ba versus La/Nb (Saunders et al., 1992), and Ba/Ta versus La/Ta (Kay and Copeland, 2006) variation diagrams and shown in Figs. 5a-b. In these diagrams, there is a close affinity between Bitlis ignimbrites and Nemrut basalts, and they show a geochemical tendency between OIB and the upper crust, suggesting an interaction between them. Based on all these results, we conclude that Nemrut felsic-silicic volcanic and pyroclastic rocks derived from partial melting of an upper crustal source interacting with OIB-like (possibly asthenospheric) mantle-derived magma. Emplacement of asthenospheric magma in the shallow upper crustal level along with extensional faults in post-collisional tectonic setting caused the partial melting and assimilation of the upper crust. OIB-like basaltic magma possibly contributed to the silicic A2-type magma batch, and explosive activity of Nemrut volcano produced felsic-silicic volcanic and pyroclastic (e.g., Bitlis ignimbrites) products during the Quaternary period.

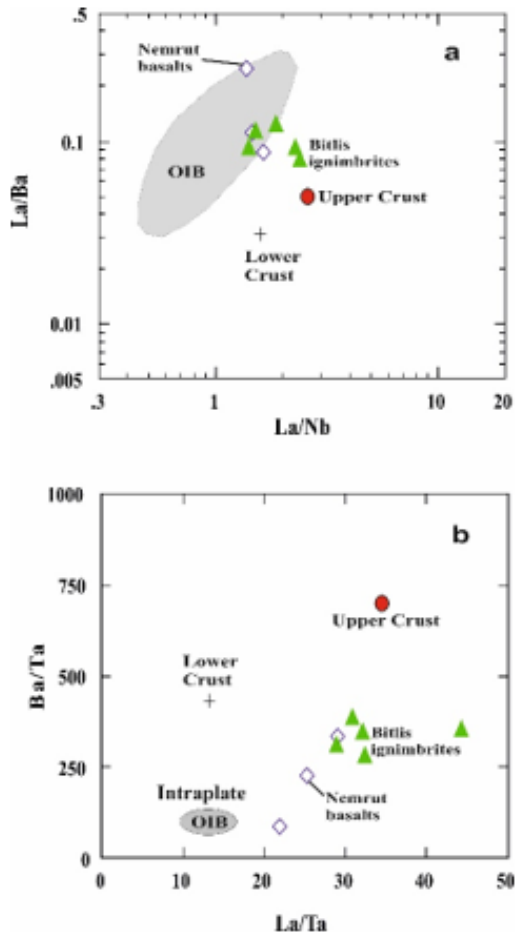


Figure 5. La/Ba vs La/Nb (a) and Ba/Ta vs La/Ta (b) variation diagrams of Bitlis ignimbrites. For comparison, Nemrut basalts (Özdemir et al., 2006) are also plotted. The upper and lower crust are from Rudnick and Gao (2004). The field intraplate is adapted from Kay and Copeland (2002). OIB field in 'a' is from Saunders et al., (1992).

4. Conclusions

Eruptions of Bitlis trachydacitic ignimbrites, produced by the Quaternary Nemrut stratovolcano during the pre-caldera stage in Eastern Anatolia post-collisional setting are younger than 790 ka, and similar to felsic-silicic volcanic rocks of Nemrut volcano, exhibit the chemical characteristics of A2-type silicic magmas. Trace element variations also suggest that the magma producing the Nemrut volcano was originated by partial melting of upper crustal rocks via emplacement of the mantle-derived OIB-like magma at the shallow crustal level under extensional tectonic. OIB-like basaltic magma was also contributed to the composition of the magma chamber during its interaction with the upper crust. Trace element variations and magma style of Nemrut volcanic and pyroclastic (e.g., Bitlis ignimbrites) rocks confirm the A2-type silicic magma generation in Eastern Anatolia post-collisional extensional setting during Quaternary.

Acknowledgments

We would like to thank Dr. Mustafa KUMRAL (ITU), who conducted geochemical analyses of rock samples at Istanbul Technical University. The authors also thanks Dr. Sema TETIKER, who contributed to K-Ar isotopic analysis.

References

- Çubukçu, H.E., Ulusoy, I., Aydar, E., Ersoy, O., Şen, E., Gourgaud, A., and Guillou, H., 2012. Mt. Nemrut volcano (Eastern Turkey): temporal petrological evolution. *J Volcanol Geotherm Res* 209–210:33–60.
- Eby, G.N., 2011. A-type granites: magma sources and their contribution to the growth of the continental crust. *Seventh Hutton Symposium on Granites and Related Rocks*, pp. 50–51.
- Karaoğlu, Ö., Özdemir, Y., Tolluoğlu, A.Ü., Karabıyıkoglu, M., Köse, O., and Froger, J.-L., 2005. Stratigraphy of the volcanic products around Nemrut Caldera: implications for reconstruction of the caldera formation. *Turkish Journal of Earth Sciences* 14, 123–143.
- Kay, S.M., and Copeland, P., 2006. Early to middle Miocene back-arc magmas of the Neu-quén Basin: geochemical consequences of slab shallowing and the westward drift of South America. *Geological Society of America Special Paper* 407, 185–213.
- Koralay, T., Özkul, M., Kumsar, H., Çelik, S.B., and Pektaş, K., 2011. The effect of welding degree on geotechnical properties of an ignimbrite flow unit: the Bitlis castle case (eastern turkey). *Environ. Earth Sci.* 64, 869–881.
- Koralay, T., Özkul, M., Kumsar, H., Çelik, S.B. ve Pektaş, K., 2014. Tarihi Yapılarda Mineralojik, Petrografik ve Jeoteknik Çalışmaların Önemi: Bitlis Kalesi Örneği (Bitlis-Doğu Anadolu). *Selçuk Üniv. Müh.-Mim. Fak. Dergisi, Sayı, 2-3*, s.54-68.
- Le Maitre, R.W., Streckeisen, A., Zanettin, B., Le Bas, M.J., Bonin, B., Bateman, P., Bellieni, G., Dudek, A., Efremova, S., Keller, J., Lameyre, J., Sabine, P.A., Schmid, R., Sorensen, H., and Woolley, A.R., 2002. *Igneous Rocks: A Classification and Glossary of Terms. Recommendations of the International Union of Geological Sciences Subcommittee on the Systematics of Igneous Rocks* Cambridge University Press, p. 236.
- Medlin, C., Jowitt, S., Cas, R., Smithies, R., Kirkland, C., Maas, R., Raveggi, M., Howard, and H., Wingate, M., 2015. Petrogenesis of the A-type, Mesoproterozoic intra-caldera rheomorphic Kathleen ignimbrite and comagmatic Rowland suite intrusions, West Musgrave Province, Central Australia: products of extreme fractional crystallization in a failed rift setting. *J. Petrol.* 56, 493–525.
- Özdemir, Y., Karaoglu, Ö., Tolluoğlu, A.U., and Gulec, N., 2006. Volcanostratigraphy and petrogenesis of the Nemrut stratovolcano, East Anatolian High Plateau): the most recent post-collisional volcanism in Turkey. *Chemical Geology* 226, 189–211.
- Pearce, J.A., 1996. Sources and settings of granitic rocks. *Episodes* 19, 120–125.
- Rudnick, R.L., and Gao, S., 2004. Composition of the Continental Crust. In: Rudnick, R.L.(Ed.), *Treatise on Geochemistry*.

- Elsevier-Pergamon, Oxford, pp. 1–64.
- Saunders, A.D., Storey, M., Kent, R.W., and Norry, M.J., 1992. Consequences of plume-lithosphere interactions. In: B.C. Storey, T. Alabaster & R.J. Pankhurst, Eds., *Magmatism and the causes of continental break-up*. Geol. Soc. Spec. Publ., 68, 41-60.
- Schmincke, H-U., Sumita, M., and Paleovan scientific team., 2014. Impact of volcanism on the evolution of Lake Van (eastern Anatolia). III. Periodic (Nemrut) vs. episodic (Süphan) explosive eruptions and climate forcing reflected in a tephra gap between ca. 14 ka and ca. 30 ka. *J Volcanol Geotherm Res* 285:195–213.
- Sumita, M., and Schmincke, H-U., 2013. Impact of volcanism on the evolution of Lake Van I: evolution of explosive volcanism of Nemrut Volcano (eastern Anatolia) during the past >400,000 years. *Bull Volcanol* 75:1–32.
- Sun, S.S., and Mc Donough, W.F., 1989. Chemical and isotopic systematics of oceanic basalts: implications for mantle composition and processes. In: Saunders, A.D., Norry, M.J. (Eds.), *Magmatism in Ocean Basins*, Geological Society of London Spec. Publ., vol. 42, pp. 313–345.
- Şengün, M., Çağlayan, A., and Sevin, M., 1991. Bitlis Masifi; Bitlis-Tatvan-Hizan-Şirvan dolayının jeolojisi (in Turkish). MTA Report No 9105.
- Whalen, J.B., Currie, K.L., and Chappell, B.W., 1987. A-type granites geochemical characteristics, discrimination, and petrogenesis. *Contributions to Mineralogy and Petrology* 95, 407–419.

Available online at www.dergipark.gov.tr/beuscitech

Journal of Science and Technology

E-ISSN 2146-7706



A case study on the updates of Turkish rapid visual screening methods for reinforced-concrete buildings

Ercan IŞIK^{a,*} , Ali Emre ULU^a , M. Cihan AYDIN^a ^a Bitlis Eren University, Department of Civil Engineering, TR-13000, Bitlis Turkey

ARTICLE INFO

Article history:

Received 15 November 2021

Received in revised form 01 December 2021

Accepted 10 December 2021

Keywords:

Rapid visual screening
Reinforced-concrete
PDRB
Site-specific

ABSTRACT

The changes in rapid seismic assessment methods that can be used to determine the regional earthquake risk distribution of buildings have become inevitable, with the Turkish Building Earthquake Code and Turkish Earthquake Hazard Map which updated in 2018. Within the scope of this study, risk prioritization was made according to the last two regulations for ten different settlements that located in the same earthquake zone in the previous earthquake map. With the current regulation, it has once again emerged that site-specific based analysis and evaluations are necessary. While the building performance scores in the previous regulation were the same for all provinces since they were located in the same earthquake zone, different values were obtained for the provinces with the current regulation. As the PGA value increased, the design spectral acceleration coefficient increased and the building's performance score was lower. This increases the risk in these regions.

© 2021. Turkish Journal Park Academic. All rights reserved.

1. Introduction

Large-scale loss of life and property may occur due to the structural damage after the earthquakes (Harirchian et al., 2020; İnel et al., 2008; Tabrizikahou et al., 2021). The characteristics of the building stock in any region are one of the important factors that will directly affect the losses that may occur (Kaplan et al., 2010; Işık, 2016; Bilgin et al., 2021). In this context, seismic vulnerability assessment is a major concern, especially in regions where earthquakes are common (Harirchian et al., 2021a; Arslan, 2010; Candela et al., 2021). In this context, determining the earthquake safety of buildings before a possible earthquake ensures correct decisions about the existing building stock (Doğan et al., 2021; Sipos and Hadzima-Nyarko, 2017; Yakut, 2004; Bilgin and Uruçi, 2018). However, the increase in the existing building stock with urbanization and increasing population makes it difficult to determine the earthquake safety of buildings in terms of time, qualified personnel and economy (Işık ve Tozlu, 2015; Kapetana and Drsitos, 2007; Ademoviç et al., 2020). At this point, it is not possible to determine the earthquake safety in

detail for the entire existing building stock (Işık et al., 2018; Özmen and İnel, 2017). Thus, buildings with risk priority can be determined by using faster and more practical evaluation methods on the building stock (Sucuoğlu et al. 2007; Kassem et al., 2021; Işık et al., 2020). These methods are generally called rapid visual screening methods (RVS). By using these methods, the number of buildings to be subjected to detailed earthquake safety analysis is greatly reduced (Harirchian and Lahmer, 2019; Biçen et al., 2020; Büyüksaraç et al., 2021; Ayhan et al., 2021). In order to overcome the destructive effects of earthquakes on the structural parameters of the building and human losses, different countries are developing various approaches and methodologies related to these methods (Harirchian et al., 2021b). These methods are one of the important measures to be taken in the pre-disaster structural sense of modern disaster management (Işık et al., 2020a). These studies on the building stock before the earthquake are also important in terms of spatial planning and urban transformation.

Officially in Turkey, these methods were first put on a legal basis with the regulation published by the Ministry of

* Corresponding author. Tel.: +0 434 222 0030; fax: +0 434 222 9145
E-mail address: eisik@beu.edu.tr

ORCID: 0000-0001-8057-065X (E.İşık), 0000-0001-7499-3891 (A.E. Ulu), 0000-0002-5477-1033 (M.C. Aydın)

Environment and Urbanization in 2013 titled as “The Principles of Determining Risky Buildings” (PDRB, 2013). With this regulation, the evaluation and prioritization of risky structures are expressed in detail. The application of the first stage evaluation method for reinforced-concrete and masonry buildings is detailed under the title of methods that can be used to determine the regional earthquake risk distribution of buildings in this regulation. However, due to the significant changes in Turkey Earthquake Hazard Maps and Turkish Building Regulations in 2018, the change in the first stage evaluation method in the regulation has also become mandatory and it has been updated and started to be used in 2019 (TBEC-2018; PDRB, 2019; <https://tdth.afad.gov.tr/>, 2020).

Within the scope of this study, information is given about the changes in the first stage evaluation method, which is included in both regulations and recommended for reinforced-concrete structures. In this study, the results obtained for an existing reinforced-concrete building selected as a sample were also compared. Considering the geographical location of the selected building as an example, earthquake parameters were determined with the help of the updated Turkey Earthquake Maps Interactive web application. In addition, the necessary data for this application aid rapid evaluation method were obtained.

2. First Stage Evaluation (2013)

The parameters considered in this method, which can be used for existing reinforced concrete buildings with 1-7 floors, are given below:

- Type of structural system
- Number of storey
- Current status and apparent quality
- Soft storey/weak storey
- Vertical irregularity
- Heavy overhangs
- Irregularity/torsion effect in plan
- Short column effect
- Adjacent/pounding effect
- Hill/slope effect
- Earthquake hazard and local soil class

Two different structural system types are expressed as reinforced-concrete frame (RCF) and reinforced concrete frame + shear wall (RCFW). The number of stories on the foundation is taken into account as the number of storey. In gradual structures, the part with the highest number of stories is taken into account. The importance given to the quality of materials and workmanship and the maintenance of the building is determined by the current condition and apparent quality and is classified as good, medium and bad. In addition to the differences in stiffness and strength between stories, the variation of stories height within the building is taken into

account in the soft story/weak story parameter. The parameter taken into account in order to reflect the effect of the frame and changing story areas that do not continue vertically is the vertical irregularity. Differences in storey areas are indicated as heavy overhangs. Irregularities that will cause torsion in the zoning plan are taken into account in the plan irregularity/torsion effect parameter. In this method, the presence of short columns in the building examined, the fact that the building was built with a pronounced hill-slope effect, and the relationship of the building with the neighboring structures are also taken into account in this method. Earthquake hazard and class are directly taken from the Regulation on Buildings to be Constructed in Seismic Zones (TSDC-2007; PDRB, 2013). The structural system type is taken into account as a positive basis point. No additional score is given for buildings with RCF system, but a positive base score (Op) is given for buildings with other structural system (RCFW). Structural system and baseline scores are shown in Table 1.

Table 1. Base and structural system scores

Total number of floors	Base score				Structural system score (YSP)	
	Danger zone				Structural system	
	I	II	III	IV	RCF	RCFW
1 and 2	90	120	160	195	0	100
3	80	100	140	170	0	85
4	70	90	130	160	0	75
5	60	80	110	135	0	65
6 and 7	50	65	90	110	0	55

While determining the danger zone for the examined building, the local soil classes and seismic zone recommended in the previous earthquake code (TSDC-2007) are taken into account, and the selection is made according to Table 2.

Table 2. Earthquake zones determined according to TSDC-2007

Danger zone	Seismic zone according to TSDC-2007	Soil class according to TSDC-2007
I	1	Z3/Z4
	1	Z1/Z2
II	2	Z3/Z4
	2	Z1/Z2
III	3	Z3/Z4
	3	Z1/Z2
IV	4	All soil types

For all negative parameters, except the apparent quality, determinations will be made as "yes" or "no". Negative parameter values (O_i) corresponding to these determinations will be taken as 1 and 0 for "yes" and "no" states, respectively. If the apparent quality rating is "good", the negativity parameter value (O_i) will be taken as 0, if it is "moderate" 1, if

it is "poor", 2 will be taken. The negative coefficients corresponding to each parameter are shown in Table 3

Table 3. Negative parameter values (O_i)

Negativity parameter	Case 1		Case 2	
	Parameter detection	Parameter value	Parameter detection	Parameter value
Soft storey	None	0	Available	1
Heavy overhangs	None	0	Available	1
Apparent quality	Good	0	Moderate (bad)	1 (2)
Short column	None	0	Available	1
Hill/slope effect	None	0	Available	1
Irregularity in plan	None	0	Available	1

The suggested point values for each parameter are shown in Table 4, and the selection is made according to the number of floors.

Table 4: Negativity parameter score (OP_i) table

Total number of floors	Negativity Parameter Scores (OP)										
	Soft storey	Apparent quality	Heavy overhangs	Storey level/ Building status				Vertical irregularity	Irregularity/torsion effect in plan	Short Column	Hill/slope effect
				Same		Different					
				Middle	Corner	Corner	Middle				
1,2	-10	-10	-10	0	-10	-5	-15	-5	-5	-5	-3
3	-20	-10	-20	0	-10	-5	-15	-10	-10	-5	-3
4	-30	-15	-30	0	-10	-5	-15	-15	-10	-5	-3
5	-30	-25	-30	0	-10	-5	-15	-15	-10	-5	-3
6,7	-30	-30	-30	0	-10	-5	-15	-15	-10	-5	-3

Building performance score (PP) is calculated according to Equation 2.1 after the total negativity score is determined by multiplying the negativity parameter values given in Table 3 with the negativity parameter points given in Table 4.

$$PP = TP + \sum_{i=1}^n O_i * OP_i + YSP \quad (2.1)$$

Here, TP is the base score; YSP indicates the structural system score.

3. First Stage Evaluation (2019)

Along with the Turkish Building Earthquake Regulation (TBEC-2018) and the Turkey Earthquake Hazard Map, which were updated in 2018 and entered into force in 2019, many parameters in the previous regulation remained the same in the method specified under the simple methods that can be used to determine the regional earthquake risk distribution of buildings. One of the important changes in the current earthquake code has been the use of site-specific design

spectra. The values obtained on a regional basis in the previous regulation have been converted to site-specific with the current regulation. At the same time, another change occurred in local soil classes. Local soil classes, which were expressed with soil group and soil classes in the previous regulation, were combined and specified as only local soil class. These changes have also found their way into simplified methods. These changes have changed the designation of danger zones. The factors taken into account to determine the danger zone of the building to be examined according to the current regulation are shown in Table 5.

In the method, the DD-2 earthquake ground motion level, which has a 50% probability of exceeding in 50 years, will be used as the ground motion level, and the short period design spectral acceleration coefficient (SDS) will be taken from the current Turkey Earthquake Hazard Map. The earthquake hazard zone will be determined by using the relationship between the SDS value and the local soil class.

Negative parameter values are the same as in the previous regulation and the values given in Table 3 are used. Likewise, there is no change in the negativity parameter score table, and the values in Table 4 will be used. The building performance

score calculation will be made according to Equation 2.1, there is no change here either.

Table 5. Seismic danger zone (PDRB,2019)

Danger zone	S_{Ds}	Soil class
I	$S_{Ds} \geq 1.00$	ZC/ZD/ZE
II	$S_{Ds} \geq 1.00$	ZA/ZB
	$1.00 \geq S_{Ds} \geq 0.75$	ZC/ZD/ZE
III	$1.00 \geq S_{Ds} \geq 0.75$	ZA/ZB
	$0.75 \geq S_{Ds} \geq 0.50$	ZC/ZD/ZE
IV	$0.75 \geq S_{Ds} \geq 0.50$	ZA/ZB
	$0.50 \geq S_{Ds}$	All soil types

After the earthquake danger zone is obtained, the determination of the base score for the building to be examined is made according to Table 6.

Table 6. Base and structural score table (PDRB, 2019)

Total number of floors	Base score (TP)				Structural system score (YSP)	
	Danger zone				Structural system	
	I	II	III	IV	RCF	RCFW
1 and 2	90	120	160	195	0	100
3	80	100	140	170	0	85
4	70	90	130	160	0	75
5	60	80	110	135	0	65
6 and 7	50	65	90	110	0	55

Information is also given about the parameters taken into account when determining the risk priority of any RC building. Having RC shear walls in the structural system increases the earthquake resistance of the building. Therefore, an additional structural system score is added in RCFWs. The types of structural system types considered in RC structures are shown in Figure 1. If the presence of RC shear walls cannot be determined, it would be appropriate to consider them as RCF.

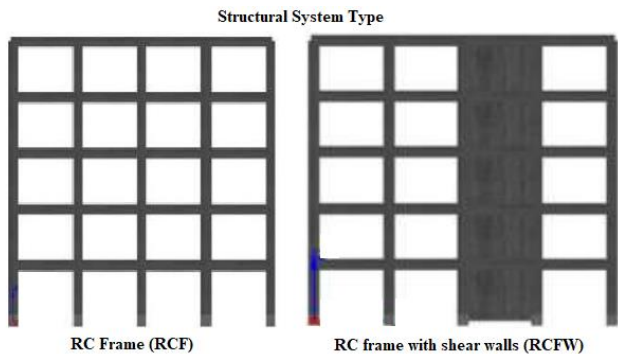


Figure 1. Structural system types

The number of stories is one of the factors affecting the earthquake behavior of the structures. The number of free stories (n_{sk}) will be determined by considering Figure 2.

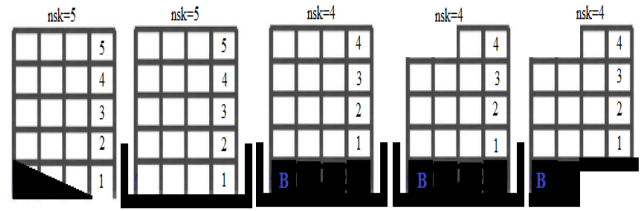


Figure 2. Determining the number of stories

The discontinuities in the vertical structural elements negatively affect the seismic behavior of the structure and are taken into account in this method. Some cases of vertical irregularity are shown in Figure 3.

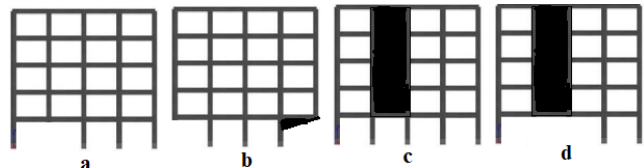


Figure 3. Some vertical irregularity, a) Non-continuing column in vertical, b) column at the console end, c) discontinuity on the shear wall, d) discontinuity on the shear wall

The difference between the storey area sitting on the ground and the storey area above the ground will be determined with overhang parameter. The example for overhang is shown Figure 4.

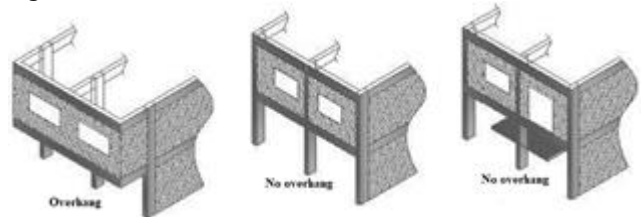


Figure 4. Sample for overhangs (available/none/none)

The other parameter is short column and only externally observed short columns are taken into account in the evaluation. The sample for short column is shown in Figure 5.

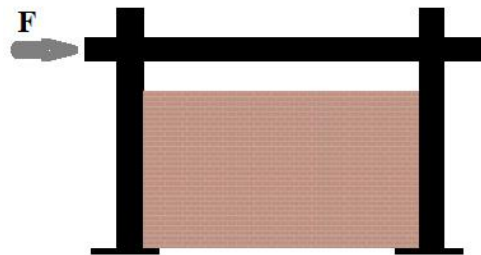


Figure 5. Short column sample

One of the parameters that negatively affect the earthquake behaviour is the irregularities in the plan of the building. Some regular and irregular samples were shown in Figure 6.

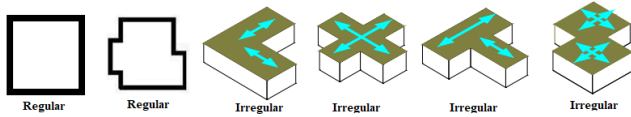


Figure 6. Samples for regular and irregular buildings plan

Another parameter is the state of the building with neighbouring buildings. This situation is shown in Figure 6.

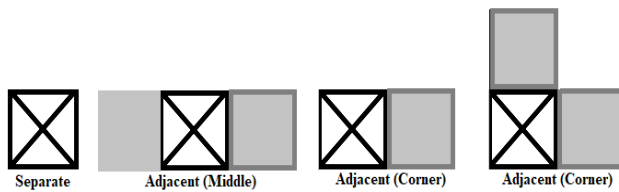


Figure 7. Samples for adjacent/pounding effect

In cases where there is a pounding effect, attention is paid to the floor levels in neighbouring buildings. The sample for this situation is shown in Figure 8.

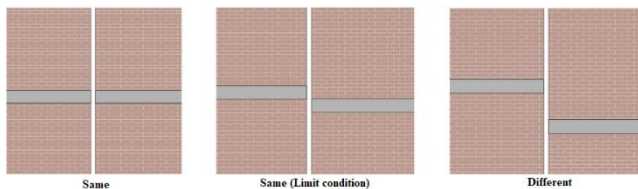


Figure 8. Floor level status in adjacent buildings

4. Determination of Structural System Score for Example RC Building

The selected sample RC building is evaluated as an existing structure. Although it does not contain any structural irregularities, it is assumed that the building has 5 stories and consists of a RCF. In order to be able to prioritize risk, ten different provinces located in the same earthquake zone were taken into account in the previous earthquake zone map. Within the scope of this study, random geographical locations from Amasya, Balıkesir, Burdur, Bilecik, Aydın, Hakkari, Hatay, Kastamonu, Kırşehir and Muğla provincial centers were taken into account. All of these provincial centers are located in the 1st degree earthquake zone in the previous earthquake zone map. It is assumed that the RC building, which is considered as an example, is located in these locations.

In the simplified method in 2013, the local soil class was accepted as Z3. Since all the provinces subject to the study are located in the same earthquake zone, the same danger zone was obtained and this region became the I. danger zone. Since the selected RC structure consists of only frames, no structural

system points are added. Since the structure examined does not contain any negativity, the total negativity score was taken as zero. The provincial values of the building performance scores obtained by using the values prescribed in the previous regulation are shown in Table 7.

Table 7. Building performance scores for 2013

Province	Danger zone	Base score	Structural system score (YSP)	Negativity Score Total	Building Performance Score
Aydın	I	60	0	0	60
Hatay	I	60	0	0	60
Amasya	I	60	0	0	60
Burdur	I	60	0	0	60
Balıkesir	I	60	0	0	60
Muğla	I	60	0	0	60
Hakkâri	I	60	0	0	60
Kastamonu	I	60	0	0	60
Bilecik	I	60	0	0	60
Kırşehir	I	60	0	0	60

In order to use the simplified method proposed for the determination of regional risk in 2019, design spectral acceleration coefficients are needed. These values were obtained by using Turkey Earthquake Hazard Maps Interactive Web Earthquake Application. ZC was chosen as the local soil class in order to make comparisons. Since there is no regional calculation with the new hazard map, spectral acceleration coefficients were obtained separately for each province. The peak ground acceleration (PGA) and design spectral acceleration coefficients obtained for the geographical locations in the provinces considered in the study, which have a 10% probability of being exceeded in 50 years (recurrence period 475 years), are shown in Table 8.

Table 8. Earthquake parameter values for selected locations

Province	PGA (g)	S _{DS}
Aydın	0.592	1.742
Hatay	0.453	1.289
Amasya	0.447	1.279
Burdur	0.409	1.156
Balıkesir	0.372	1.057
Muğla	0.370	1.036
Hakkari	0.319	0.904
Kastamonu	0.289	0.839
Bilecik	0.237	0.718
Kırşehir	0.088	0.261

In order to make comparisons with the previous simplified method, the same RC building was evaluated as the existing building. This building has the same structural features and only the location of the building has changed. As in the previous regulation, no structural system score has been added since the selected RC structure consists only of frames (RCF). Since the structure examined does not contain any negativity, the total

negativity score was taken as zero. The provincial values of the building performance scores obtained by using the values predicted for RC buildings in the simplified method in the current regulation are shown in Table 9.

Table 9. Building performance scores for 2019

Province	Danger zone	Base score	Structural system score (YSP)	Negativity Score Total	Building Performance Score
Aydın	I	60	0	0	60
Hatay	I	60	0	0	60
Amasya	I	60	0	0	60
Burdur	I	60	0	0	60
Balıkesir	I	60	0	0	60
Muğla	I	60	0	0	60
Hakkâri	II	80	0	0	80
Kastamonu	II	80	0	0	80
Bilecik	III	110	0	0	110
Kırşehir	IV	135	0	0	135

5. Results and Conclusions

With the increase in population and increasing urbanization due to this increase, our building stock is increasing day by day. Whether the increased building stock is built in accordance with earthquake resistant building design principles and whether it receives engineering services will directly affect the losses in a possible earthquake. One of the processes in the pre-disaster preparation phase of modern disaster management is to decide whether the earthquake performance of the building stock in the region to be affected by the earthquake is sufficient. In the light of this information to be obtained, it is necessary to determine the buildings with insufficient earthquake performance and to decide on demolition and reinforcement when necessary. The large number of building stocks does not make such detailed structural analyzes possible. These methods specified simplified methods in order to minimize the amount of building stock to be examined. For the first time in Turkey, risk prioritization among buildings was legally stated under PDRB-2013. Finally, mandatory changes were inevitable in the proposed simplified methods along with the earthquake regulation and earthquake hazard maps updated in 2018. This study examined the differences of the simplified methods in the last two regulations for reinforced concrete structures. While examining, ten different provinces located in the same earthquake zone were selected in the previous earthquake zone map. The 2013 regulation was based on a methodology on a regional basis, just like the earthquake zone map and earthquake regulation used at that time. As the provinces selected within the scope of this study are located in the same earthquake zone, the same building performance score was obtained for all provinces. Therefore, it was not possible to determine any risk priority among these provinces.

Obtaining site-specific earthquake parameters from a regional basis is one of the important changes and gains in both

earthquake hazard maps and seismic design code. The results obtained in this study are a clear indication of this. The design spectral acceleration coefficients and peak ground acceleration values obtained for the provinces with the current map have been obtained differently for all provinces considered in the study. However, the same values were used for these provinces in the previous map and regulation. With the increase of PGA value, spectral acceleration values also increased. It has been determined that the risk of structures in accommodation units where PGA and SDS are large is greater. With the increase in the SDS value, the building performance score was evaluated as riskier by taking lower values. The danger zone and building performance scores obtained for randomly selected geographical locations in Aydın, Hatay, Amasya, Burdur, Balıkesir and Muğla provinces have the same values as the previous regulation. However, different earthquake hazard zone and building performance scores were obtained for Hakkari, Kastamonu, Bilecik and Kırşehir. While there was only one danger zone in the previous regulation, four different danger zones have been obtained in the new regulation. The lowest risk priority was obtained for the province of Kırşehir, which has the lowest SDS value. By using other earthquake parameters obtained with the help of site-specific methodology in the current regulation, risk priority can be decided among buildings with the same building performance score. The current simplified method has been made more practical than the previous one. The visuals on how to obtain the negativity parameters used in the method through the structure prevent users from making incomplete or wrong.

References

- Ademović, N., Šipoš, T.K., and Hadzima-Nyarko, M., 2020. Rapid assessment of earthquake risk for Bosnia and Herzegovina. *Bulletin of Earthquake Engineering*, 18(5), 1835-1863.
- Arslan, M.H., 2010. An evaluation of effective design parameters on earthquake performance of RC buildings using neural networks. *Engineering Structures*, 32(7), 1888-1898.
- Ayhan, E., Aktaş, G., and Karaşin, A., 2021. Siirt ilindeki bazı binaların riskli bina tespit yönetmeliğine göre değerlendirilmesi. *Dicle Üniversitesi Mühendislik Fakültesi Mühendislik Dergisi* 12(1), 89-98.
- Bicen, V.S., Isık, E., Arkan, E., and Ulu, A.E., 2020. A study on determination of regional earthquake risk distribution of masonry structures. *J Arch, Eng, Fine Arts*, 2(2), 74-86.
- Bilgin, H., Shkodrani, N., Hysenlliu, M., Ozmen, H. B., Isık, E., and Harirchian, E., 2021. Damage and performance evaluation of masonry buildings constructed in 1970s during the 2019 Albania earthquakes. *Engineering Failure Analysis*, 105824.
- Bilgin, H., & Uruçi, R. 2018. Effects of structural irregularities on low and mid-rise RC building response. *Challenge Journal of Structural Mechanics*, 4(2), 33-44.

- Buyuksarac, A., Isik, E., and Harirchian, E., 2021. A case study for determination of seismic risk priorities in Van (Eastern Turkey). *Earthquakes and Structures*, 20(4), 445-455.
- Candela, T., Rosset, P., and Chouinard, L., 2021. A Quantitative Approach to Assess Seismic Vulnerability of Touristic Accommodations: Case Study in Montreal, Canada. *GeoHazards*, 2(2), 137-152.
- DEMP, 2020. "Interactive earthquake map web page for the 08.06.2020 available at <https://tdth.afad.gov.tr/>"
- Doğan, T.P., Kızılkula, T., Mohammadi, M., Erkan, İ.H., Kabaş, H.T., and Arslan, M.H., 2021. A comparative study on the rapid seismic evaluation methods of reinforced concrete buildings. *International Journal of Disaster Risk Reduction*, 56, 102143.
- Harirchian, E., Lahmer, T., Buddhiraju, S., Mohammad, K., and Mosavi, A., 2020. Earthquake safety assessment of buildings through rapid visual screening. *Buildings*, 10(3), 51.
- Harirchian, E., and Lahmer, T., 2020. Improved rapid visual earthquake hazard safety evaluation of existing buildings using a type-2 fuzzy logic model. *Applied Sciences*, 10(7), 2375.
- Harirchian, E., Hosseini, S. E. A., Jadhav, K., Kumari, V., Rasulzade, S., Işık, E., and Lahmer, T., 2021a. A review on application of soft computing techniques for the rapid visual safety evaluation and damage classification of existing buildings. *Journal of Building Engineering*, 102536.
- Harirchian, E., Kumari, V., Jadhav, K., Rasulzade, S., Lahmer, T., and Raj Das, R., 2021b. A Synthesized Study Based on Machine Learning Approaches for Rapid Classifying Earthquake Damage Grades to RC Buildings. *Applied Sciences*, 11(16), 7540.
- Inel, M., Ozmen, H. B., and Bilgin, H., 2008. Re-evaluation of building damage during recent earthquakes in Turkey. *Engineering Structures*, 30(2), 412-427.
- Isik, E., 2016. Consistency of the rapid assessment method for reinforced concrete buildings. *Earthquakes and Structures*, 11(5), 873-885.
- Işık, E., and Tozlu, Z., 2015. Farklı Değişkenler Kullanılarak Yapı Performans Puanının Hesaplanması. *Bitlis Eren Üniversitesi Fen Bilimleri Enstitüsü Dergisi*, 4(2), 161-172.
- Işık, M. F., Işık, E., and Bülbül, M. A., 2018. Application of iOS/Android based assessment and monitoring system for building inventory under seismic impact. 70 (12), 1043-1056
- Işık, E., Karaşin, İ. B., Demirci, A., and Büyüksarac, A., 2020a. Seismic risk priorities of site and mid-rise RC buildings in Turkey. *CHALLENGE*, 6(4), 191-203.
- Işık E., Kaya, B. and Karaşin İ.B., 2020. The effect of different negative parameters on the performance of steel structures. *Bitlis Eren University Journal of Science and Technology*, 10(2), 73-83.
- Kapetana, P., and Dritsos, S., 2007. Seismic assessment of buildings by rapid visual screening procedures. *Earthquake Resistant Engineering Structures VI*, 93, 409.
- Kaplan, H., Bilgin, H., Yilmaz, S., Binici, H., and Öztas, A., 2010. Structural damages of L'Aquila (Italy) earthquake. *Natural Hazards and Earth System Sciences*, 10(3), 499-507.
- Kassem, M.M., Beddu, S., Ooi, J. H., Tan, C.G., Mohamad El-Maissi, A., and Mohamed Nazri, F., 2021. Assessment of Seismic Building Vulnerability Using Rapid Visual Screening Method through Web-Based Application for Malaysia. *Buildings*, 11(10), 485.
- Ozmen, H. B., and Inel, M., 2017. Effect of rapid screening parameters on seismic performance of RC buildings. *Structural engineering and mechanics*, 62(4), 391-399.
- PDRB, 2019. *The Principles of Determining Risky Buildings*, Turkey Ministry of Environment and Urbanization Ankara, Turkey.
- PDRB, 2013. *The Principles of Determining Risky Buildings*, Turkey Ministry of Environment and Urbanization Ankara, Turkey.
- Šipoš, T.K. and Hadzima-Nyarko, M., 2017. Rapid seismic risk assessment. *International Journal of Disaster Risk Reduction*, 24, 348-360.
- Sucuoğlu, H., Yazgan, U., and Yakut, A., 2007. A screening procedure for seismic risk assessment in urban building stocks. *Earthquake Spectra*, 23(2), 441-458.
- Tabrizikahou, A., Hadzima-Nyarko, M., Kuczma, M., and Lozančić, S., 2021. Application of shape memory alloys in retrofitting of masonry and heritage structures based on their vulnerability revealed in the Bam 2003 earthquake. *Materials*, 14(16), 4480.
- TBEC-2018, 2018. *Turkish Building Earthquake Code*, T.C. Resmi Gazete; 30364 Ankara Turkey.
- TSDC-2007, 2007. *Turkish Seismic Design Code*
- Yakut, A., 2004. Preliminary seismic performance assessment procedure for existing RC buildings. *Engineering Structures*, 26(10), 1447-1461.